Dissertation

submitted to the
Combined Faculty of Natural Sciences and Mathematics
of Heidelberg University, Germany
for the degree of
Doctor of Natural Sciences

Put forward by
Annie Meneses González
born in Havana, Cuba
Oral examination: 25 July, 2023

TCAD Simulations and Characterization of High-Voltage Monolithic Active Pixel Sensors

Referees:
Prof. Dr. André Schöning
Prof. Dr. Peter Fischer

To my incredible mother,
whose unwavering love, support, and encouragement
have been my guiding light through this academic journey.
This achievement is as much yours as it is mine!

Zusammenfassung

Hochspannungsgetriebene monolithisch aktive Pixelsensoren (HV-MAPS) haben sich als vielversprechende Technologie für Silizium-Spurdetektoren in der Teilchenphysik erwiesen. Mu3e hat sich für HV-MAPS als Pixeltechnologie entschieden und Implementationen in anderen Detektoranwendungen werden untersucht. Aufgrund der einzigartigen Struktur und elektrischen Feldverteilung sind besondere Herausforderungen an das Design gestellt

In Rahmen dieser Arbeit wird der erste umfassende Vergleich von TCAD- Simulationen (Technology Computer-Aided Design) und experimentellen Messungen von HV-MAPS vorgestellt. Die Ergebnisse zeigen, dass die Simulationen wichtige experimentelle Parameter wie die Durchbruchsspannung korrekt beschreiben und den Detektionseffizienzverlust an der Pixelecken und übergängen erklärt.

Die TCAD-Simulationen bieten Einblicke in das Verhalten der Ladungssammlungsdiode der Prototypen MuPix8, ALTASPix und MuPix10 und erleichtern die Optimierung des Designs. In diesen Studien wurden vor allem die Verarmungszone, die Durchbruchspannung und die Verteilung des elektrischen Feldes untersucht. Darüber hinaus ermöglicht die Charakterisierung von MuPix10 anhand von Teststrahlergebnissen die Untersuchung der In-Pixel-Clustergröße und -Effizienz für verschiedene Einfallswinkel der Teilchen.

Darüber hinaus werden die Auswirkungen von Diffusion und Drift auf den Effizienz und die Clustergröße bei verschiedenen Spannungskonfigurationen, sowie Sensordicken und resistivitäten, undetersucht. Die Ergebnisse dieser Untersuchung tragen zu einem besseren Verständnis von HV-MAPS und ihrem Potenzial für die Entwicklung effizienterer und zuverlässigerer Silizium-Spurdetektoren für Teilchenphysikexperimente bei.

Abstract

High-Voltage Monolithic Active Pixel Sensors (HV-MAPS) have emerged as a promising technology for silicon tracking detectors in particle physics. HV-MAPS, selected as the foundational technology for the Mu3e Pixel Tracker and under investigation for potential implementation in future detector applications, presents unique design challenges due to its intricate structure and complex electric field distribution.

This thesis presents the first comprehensive comparison of Technology Computer-Aided Design (TCAD) simulations and experimental measurements in HV-MAPS. The results show that the simulations correctly describe key experimental parameters like breakdown voltage and explain the loss of hit detection efficiency at the edges and corners of the pixels.

The TCAD simulations provide insights into the behavior of the charge collection diode of MuPix8, ALTASPix, and MuPix10 prototypes, facilitating design optimizations. These studies primarily investigated the depletion zone, breakdown voltage, and electric field distribution. Additionally, the characterization of MuPix10, using testbeam results, allows for the investigation of the efficiency and cluster size for different angles of incidence of the beam.

Furthermore, this research examines the impact of diffusion and drift on efficiency and cluster size for different voltage, resistivity, and thickness configurations. The findings of this investigation contribute to an enhanced understanding of HV-MAPS and their potential for developing more efficient and reliable silicon tracking detectors in particle physics experiments.

Contents

Chapter 1

Introduction

In the late 1970s, following the discovery of the J/ψ[1] [1] meson, semiconductor sensors became common as tracking devices in particle physics. The quest to observe decays of charmed particles with picosecond lifetimes pushed experimental techniques to their limits, requiring spatial resolutions below 100 µm [2] for direct observation. However, many existing detector technologies like gaseous detectors and bubble chambers [3] struggled to study high statistics events effectively, leading to the realization that semiconductor detectors could provide a viable solution [4]. The attractive features of semiconductor detectors were similar to those cited today: linearity, good energy resolution, small energy loss, compactness, and fast response. In these applications, silicon is preferred because of its electrical properties and abundance. Additionally, its processing is well-developed thanks to the progress in the electronics industry, leading to low production costs and large availability.

Particle physics has long relied on silicon tracking detectors to precisely measure particle trajectories. In this context, High-Voltage Monolithic Active Pixel Sensors (HV-MAPS) have emerged as a promising technology offering good efficiency, position, and time resolution while keeping the material budget minimal. Many HV-MAPS prototypes have been developed to address the challenges imposed by present and foreseen tracking detectors.

In recent years, Technology Computer-Aided Design (TCAD) [5] simulations have emerged as a powerful tool to study the behavior of semiconductor devices. TCAD simulations can help to optimize the design of HV-MAPS, predict their performance under different operating conditions, and facilitate the interpretation of experimental results. The content presented in this thesis focuses on the optimization and

[1] Simultaneously dubbed ψ (at Stanford Linear Accelerator Center) and J (at Brookhaven).

characterization of HV-MAPS using TCAD simulations and testbeam experimental measurements.

This research encompasses a detailed investigation into the charge collection efficiency and charge sharing of MuPix10, an HV-MAPS specifically developed for the Mu3e experiment. The bias voltage, detector thickness, and resistivity configurations are analyzed. Additionally, the thesis examines the behavior of detector efficiency as a function of the incident particle angle.

Thesis Outline

Chapter 2 provides an overview of silicon tracking detectors and their importance in particle physics experiments. Chapter 3 describes the design and operation of HV-MAPS and the challenges associated with their optimization and characterization. Chapter 4 introduces the TCAD simulation tool and models used in this work. Chapter 5 presents the TCAD simulations of HV-MAPS, including optimizing their design and predicting their performance under different conditions. Chapter 6 describes the testbeam campaigns carried out to characterize HV-MAPS performance. This chapter discusses the experimental setup, the data acquisition system, and the analysis techniques used to extract the relevant parameters from the measurements. Finally, Chapter 7 presents the reconstruction and analysis of the MuPix10 testbeam measurements. This chapter also includes TCAD simulation results to interpret the experimental results.

Contributions from the author

Since MuPix7, the author has actively engaged in TCAD simulations of HV-MAPS, providing insights regarding the in-pixel structure, charge collection process, and leakage current. Collaborating with colleagues from the ASIC and Detector Laboratory at the Karlsruhe Institute of Technology and the HV-MAPS and Mu3e groups at Heidelberg University, the author has been responsible for the HV-MAPS TCAD simulations.

This responsibility encompasses various tasks, such as generating simulation models, executing simulations, and extracting relevant data for subsequent analysis. The author's investigations have focused on the electric field strength in the inter-pixel region, the impact of metal layer spacing on the high electric field, and the influence of electric field distribution on the charge collection process. These results have contributed to optimizing MuPix and ATLASPix sensors and offered insights into their behavior.

Furthermore, the author actively participated in collaborative testbeam campaigns alongside members of the HV-MAPS and Mu3e collaborations from Heidelberg University. Specifically, the author assumed responsibility for all testbeam measurements involving the MuPix10 sensor in the ALPIDE telescope. Moreover, the author analyzed all testbeam data presented in this work. For the in-pixel analysis presented in Chapter 7, the author made modifications to the Corryvreckan software, which facilitated the analysis of data collected during the aforementioned test beam campaigns.

Part I.

Introduction

Chapter 2

Silicon Tracking Detectors

2.1. Silicon Wafers: Preparation and Properties

2.1.1. Properties of Silicon

Silicon (Si) is the second most abundant element on earth and is the preferred semiconductor material because it is the most intensively studied semiconductor. Additionally, it can be operated at room temperature to obtain a good resolution, is cheaply available in large quantities, and its processing is well-developed thanks to the progress in the electronics industry. Table 1 lists some basic parameters of Si.

Table 1.: Basic Parameters of silicon. [6]

Atomic number	14	
Crystal structure	Diamond	
Lattice constant	0.5431	nm
Density	2.329	gcm^{-3} at 298 K
Atoms	$4.96x10^{22}$	cm^{-3}
Dielectric constant	12	relative to vacuum
Melting point	1687	K
Thermal conductivity	149	$Wm^{-1}K^{-1}$
Band gap	1.12	eV at 298 K
Intrinsic carrier density	$9.65x10^{9}$	cm^{-3} at 298 K
Intrinsic resistivity	$2.3x10^{5}$	Ωcm at 298 K
Electron mobility	1350	$cm^2V^{-1}s{-}1$ at 298 K
Hole mobility	480	$cm^2V^{-1}s{-}1$ at 298 K
Energy per electron-hole pair	3.62	eV at 298 K

2.1.2. Intrinsic and Extrinsic Semiconductors

The periodic lattice of Si and any other crystalline material establishes allowed energy bands for electrons that exist within that solid. The energy of any electron must be confined to one of these energy bands, which may be separated by gaps or ranges of forbidden energies (no allowable electronic states for them to occupy). The lower band called *valence band*, corresponds to outer-shell electrons bonded to specific crystal lattice sites. In the case of Si, they are part of the covalent bonding. The next higher-lying band is called *conduction band* and represents free electrons migrating through the crystal. Electrons in this band contribute to the material's electrical conductivity (σ). These two bands are separated by the *bandgap*. At low temperatures and in the absence of impurities ("**intrinsic silicon**"), the valence band is full, and the conduction band is empty. Under these circumstances and without ionizing radiation, it would theoretically not show any electrical conductivity.

At higher temperatures, some thermal energy is shared by the electrons in the crystal, and it is possible for valence electrons to gain sufficient thermal energy to be elevated across the bandgap into the conduction band. This excitation process creates an electron in the conduction band, leaving a vacancy (hole) in the valence band. The equal concentration of electrons n in the conduction band and holes p in the valence band is known as intrinsic concentration (n_i).

$$n_i = n = p \tag{1}$$

The probability that an electron-hole pair is thermally generated is given by:

$$p(T) = CT^{\frac{3}{2}} e^{-\frac{E_g}{2kT}} \tag{2}$$

Where T is the absolute temperature, E_g is the bandgap energy, k is the Boltzmann constant, and C is the proportionality constant characteristic of the material. As reflected in the exponential term, the probability of thermal excitation critically depends on the bandgap energy ratio to the absolute temperature.

A simplified representation of the energy bands is shown in Figure 1. In metals, electrons can easily move through the material because they need to achieve only small incremental energy to the conduction band; therefore, they are always characterized by very high electrical conductivity. In semiconductors or insulators, the electrons must first cross the bandgap to reach the conduction band, and the conductivity is, therefore, many orders of magnitude lower.

(a) Metal **(b) Semiconductor** **(c) Insulator**

Figure 1.: Energy band structure.

Figure 2 shows the range of electrical conductivities (and the corresponding resistivities $\rho = 1/\sigma$) of some materials in each of the three classes.

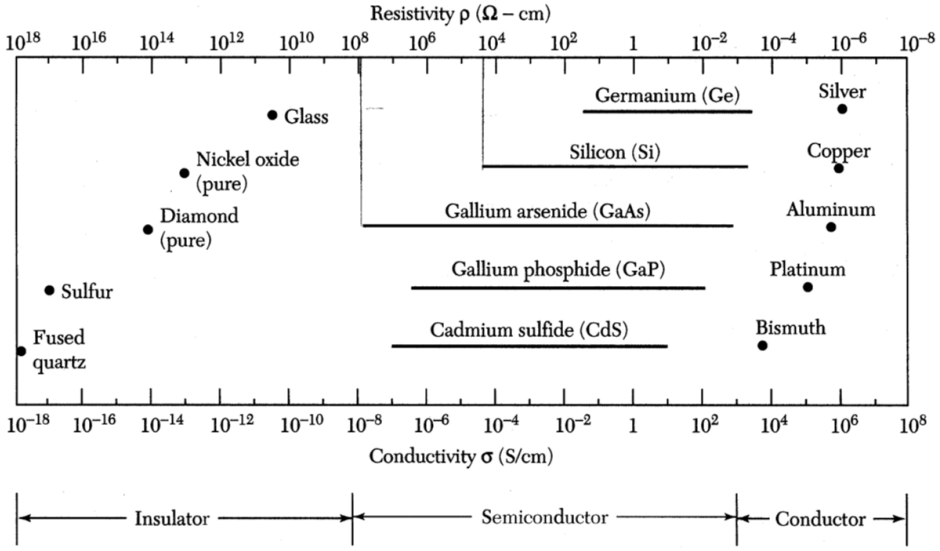

Figure 2.: Range of conductivities for insulators, semiconductors, and conductors. [7]

Intrinsic semiconductors are rarely used in semiconductor devices since obtaining sufficient purity in the material is extremely difficult. In most cases, the properties of the material are altered by adding small fractions of specific impurities during crystal growth or later in selected regions of the crystal ("**extrinsic silicon**"). Depending on the added material, one obtains *n-type* silicon by adding type V materials (e.g.,

phosphorus, donor impurity) with an excess of electrons in the conduction band or *p-type* by adding type III materials (e.g., boron, acceptor impurity) with additional holes in the valence band.

n-type silicon

Figure 3a shows a two-dimensional schematic bond representation of a Si crystal with one Si atom replaced by an arsenic atom with five valence electrons. Four electrons are used to form covalent bonds with neighboring atoms. The fifth electron has a relatively small binding energy to its host atom and can be ionized to become a conduction electron at a moderate temperature (electrons are the majority of charge carriers). The crystal as a whole remains uncharged since the charge of the free electron is compensated by the excess charge of the arsenic nucleus bound in the crystal lattice.

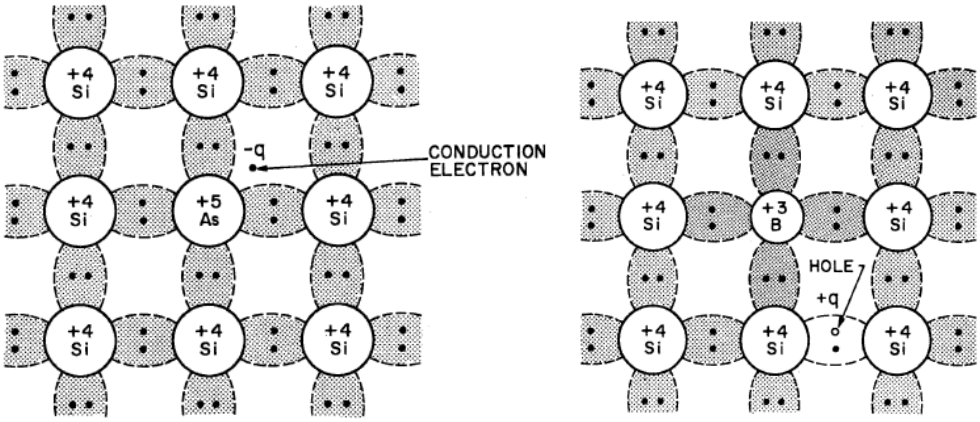

(a) n-type Si with donor (arsenic) **(b) p-type Si with acceptor (boron)**

Figure 3.: Schematic bond representation. [8]

p-type silicon

If a Si atom is replaced by an atom with only three valence electrons, as in Figure 3b, one electron is missing in the covalent bonds, and a hole is thus created. This hole may be filled by an electron from a neighboring atom, equivalent to the hole's movement. The hole is free for conduction (holes are the majority of charge carriers).

2.1.3. Dopants and Impurities

The result of the growth process of Si is a high-purity material containing small amounts of foreign dissolved atoms. Typically, most of the contamination of the

Si lattice takes place during device fabrication. However, unintentional doping[1] during the growth process has several sources, but their concentration is kept at an acceptably low level.

- Metals and carbon impurities may originate from the starting material and are generally harmful, with rare exceptions [9, 10].
  - The exact effect of the metal impurities depends on the metal and its concentration (e.g., iron can decrease the recombination lifetime [11]).
- Oxygen coming from the Czochralski (CZ)[2] crystal growth [12] has a dual role.
  - Oxygen originating from the silica crucible in interstitials (atoms dissolved in the lattice in empty spaces) gives the wafers mechanical strength against thermal, gravitational, or mechanical stress during heat treatments, decreasing the risk of slip dislocation formation and wafer warping [13].
  - Too high oxygen concentration ($>$ 9x10^{17} atoms/cm^3) can be harmful if it induces too strong precipitation of oxygen [14] and formation of defects [15].

Today most of the used Si is intentionally doped, up to a few tens of ohm centimeters, with elements from groups III and V of the periodic table of elements. The most commonly used elements are boron, antimony, arsenic, and phosphorus.

- These typical dopants are substitutional (they replace Si atoms in the lattice structure) and at very high doping levels (above 10^{18} atoms/cm^3) a small fraction of the atoms are inactive and in interstitial places.
- The three most popular donors: phosphorus, antimony, and arsenic, are not replaceable by each other because they have different limits for the lowest resistivity achievable.
- Boron and phosphorus are typical in lightly doped crystals, while all four elements are used in the highly doped cases.

2.1.4. Resistivity

The crystals' resistivity, ρ, is controlled by adding precise amounts of the specified acceptor or donor impurities. The resistivity can be expressed in terms of the carrier concentrations p (n) and mobility μ_p (μ_n) as [7]:

[1] Mechanism that alters conductivity behavior through additional states in the forbidden region.
[2] CZ is the workhorse that produces the vast majority of single-crystal silicon used today (»90%).

$$\rho = (q\mu_p p)^{-1} \qquad \text{for p-type silicon} \tag{3.1}$$

$$\rho = (q\mu_n n)^{-1} \qquad \text{for n-type silicon} \tag{3.2}$$

Where q = 1.602x10^{-19} C is the elementary charge, μ the mobility, and n,p the electrons and holes carrier concentration. The mobility values, mainly at high concentrations above 10^{16} cm^{-3}, are dependent on the dopant densities and therefore are not constants.

Figure 4 shows the correlation between the resistivity and dopant concentration by using parameterized functions, which can be found in SEMI MF723 [16], together with the references to the experimental data on which the fit is based.

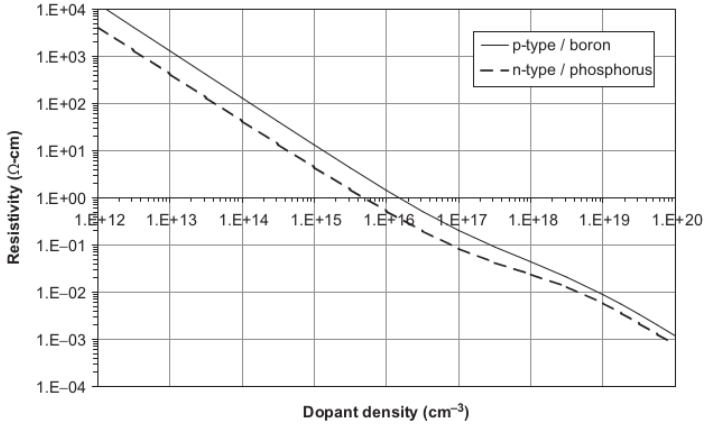

Figure 4.: Resistivity versus dopant density at 23°C. [6]

Carrier Concentration

In extrinsic semiconductors with shallow donors, there is usually enough thermal energy (E_D) to ionize all donor impurities at room temperature and thus provide the same number of electrons in the conduction band as donors. This condition is called complete ionization. Figure 5 shows some of the measured ionization energies in eV for various impurities in Si.

Under complete ionization, the electron density can be written as:

$$n = N_D \tag{4}$$

Where N_D is the donor concentration. Similarly, for semiconductors with shallow acceptors, if there is complete ionization, the concentration of holes is:

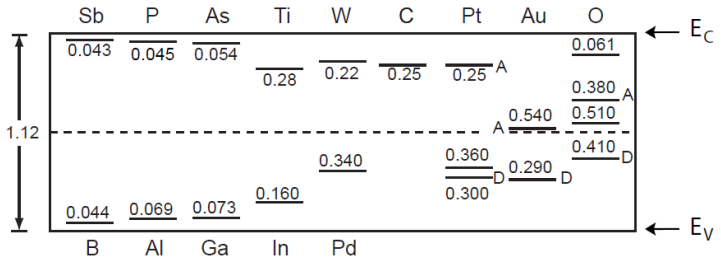

Figure 5.: Measured ionization energies (in eV) for various impurities in Si. [17]

$$p = N_A \tag{5}$$

Where N_A is the acceptor concentration. Using Equations 48 in Appenix A, we can express the electron and hole densities in terms of n_i and the intrinsic Fermi level (E_i).

$$n = n_i e^{(E_F - Ei)/kT} \tag{6.1}$$
$$p = n_i e^{(E_i - E_F)/kT} \tag{6.2}$$

A mathematical description of the electron and hole densities in intrinsic semiconductors can be found in Appendix A. Identically to that for the intrinsic case, the product of n and p equals n_i^2 (*mass action law*).

The Fermi level (E_F) for n-type (p-type) semiconductors, in terms of the effective density of states in the conduction band N_C (valence band N_V) and the donors N_D (acceptors N_A) concentration, can be obtained by substituting Equation. 4 (5) in Equation 48.1 (48.2) from Appendix A as:

$$E_C - E_F = kTln(N_C/N_D) \tag{7.1}$$
$$E_F - E_V = kTln(N_V/N_A) \tag{7.2}$$

We can see from Equation 7.1 that the higher the donor concentration, the smaller the energy difference (E_C-E_F); that is, the Fermi level will move closer to the bottom of the conduction band. Similarly, from Equation 7.2, the Fermi level will move closer to the top of the valence band for higher acceptor concentrations.

Generation and Recombination Process

When the electron and hole concentration product deviates from the thermal equilibrium ($np = n_i^2$), a recombination and generation process (also known as the Shockley-Read-Hall process [18]) restores the system to equilibrium. When $np < n_i^2$, thermal generation happens, whereas if $np > n_i^2$, recombination occurs.

In Si, the dominant recombination-generation process is an indirect transition[3], which occurs through the intermediate states in the band gap (due to impurities in the Si lattice). Four intermediate-state assisted processes, shown in a schematic representation in Figure 6, can be distinguished:

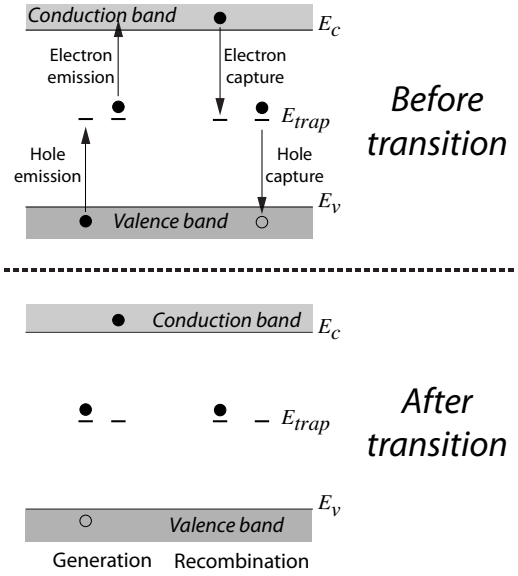

Figure 6.: Generation and recombination processes through indirect transitions. Indirect transitions occur via intermediate band gap states acting as generation-recombination or trapping centers. Adapted from [19]

1. Hole emission: This process involves the capture of a valence-band electron by the intermediate state. As this electron leaves behind a hole, it can be seen as if the gap state emits a hole.

2. Electron emission: The transition of a captured electron to the conduction band.

[3]Direct recombination process is very unlikely because the electrons at the bottom of the conduction band have a nonzero momentum with respect to the holes at the top of the valence band. Direct recombination that conserves energy and momentum is impossible without a simultaneous lattice interaction. [18]

3. Electron capture: The process in which a gap state catches an electron from the conduction band.

4. Hole capture: The transition of a captured electron from a trap to the valence band can be seen as if the intermediate state captures a hole.

Emission processes 1 and 2 combine to generate electron-hole pairs, whereas capture mechanisms 3 and 4 contribute to electron-hole recombination. The net recombination rate is given by [7]:

$$U = \nu_{th}\sigma_o N_t \frac{np - n_i^2}{n + p + 2n_i \cosh(\frac{E_t - E_f}{kT})} \tag{8}$$

Where ν_{th} is the thermal velocity of the carriers, N_t is the concentration of the recombination center in the semiconductor, σ_o is the electron and hole capture cross-section, E_t is the trap activation energy, and E_f the Fermi-Level. Equation 8 shows that net recombination decreases if the cosh term becomes larger by E_t moving away from the middle of the bandgap E_f.

In addition, a sequence of transitions 2 and 3 or 1 and 4 can occur. In either case, a carrier is captured and subsequently emitted to the band where it came from, and neither generation nor recombination occurs. This process is known as trapping and is predominantly mediated by shallow states. Due to their position close to the band edges, the capture probability of shallow states is high. Nonetheless, their emission probability is equally high, which means charge carriers only occupy these states for a relatively short time (of the order of ns). Deep states, however, have a considerably lower capture and emission probability. Consequently, these states can trap carriers for a relatively long time ($0.1 - 1$ µs).

2.1.5. Wafer Cutting, Shaping and Finishing

Si crystals (or ingots) grown with either Czochralski or float zone (FZ)[4] [20, 21] techniques are typically up to 2 m long. Crystals don't have a uniform resistivity distribution, with the seed end having higher resistivity and the tail end having low resistivity. This distribution depends on the dopant used and crystal growth process parameters. For example, with phosphorus doping, the resistivity ratio between the neck and tail parts can exceed 4:1 [6]. These, combined with practical

[4] FZ is only used if very high-resistivity silicon (>5-10 kΩcm) or silicon without dissolved oxygen is needed.

manufacturability aspects, dictate that the crystal needs to be cut in suitable lengths for further processing.

The first step is to cut away the head part (shoulder) and tail part of the ingot (**cropping**), leaving the cylindrical part for further processing. A grown ingot is not perfectly round, as there is diameter fluctuation along the length of the ingot. Cylindrical **grinding** [22] with diamond tools shapes the ingot round. The finished piece of the ingot is then ready for cutting into wafers.

Wafers have, after cutting, a large average wafer-to-wafer thickness variation and a large total thickness variation (TTV) within the wafer. TTV in as-cut wafers may exceed 5 µm, and the average thickness variation from wafer to wafer can be over 20 µm. Traditionally, dimensional variations are reduced with dual-side **lapping** [23]. After the total removal of 50-100 µm wafer, TTV is well below 1 µm, and the average thickness range within a production lot is a few micrometers. Lapping can be replaced or supplemented with single side **grinding** [24]. This technique has been advanced in recent years and gives very good flatness and thickness control. Under suitable illumination, ground wafers show shallow grinding marks visible to the unaided eye. However, these marks can be removed in double-sided **polishing** [25]. This technology makes it possible to make wafers with a few micrometer thickness spread and low TTV well below 1 µm.

Nevertheless, lapping and grinding can leave residual mechanical damage[5] on the wafer surface [19]. Mechanical damage reduces the crystalline integrity at the sensor's surfaces, causing dangling bonds, which give rise to intermediate states in the forbidden gap. These states increase the conductivity of those regions, promoting the current flow, and hence can cause undesirably high leakage currents and early breakdown of the device [26]. This damage can be removed, and the wafer cleaned from leftover impurities in a **chemical etching** step [27].

2.2. Sensor Manufacturing Steps

Oxidation

The first step in most sensor production processes is protecting the wafer surface with a silicon dioxide layer (SiO_2). The success of SiO_2 in device fabrication stems from its chemical stability and thoroughly known properties. SiO_2 serves many different functions for the fabrication and final device structures.

[5] Damage can manifest as micro-cracks propagating into the crystal and chip-outs.

- From the fabrication point of view, the essential tasks are diffusion and ion implantation masking.

- As to the device functions, it serves as capacitor dielectrics, isolations dielectrics for the multilevel metallization systems, and final passivation layers.

SiO_2 in device fabrication is produced in several different ways as indicated in [28], and the choice of the method is a compromise between cost and performance.

Doping

The practical use of impurity doping has been mainly to change the electrical properties of semiconductors. *Diffusion* and *ion implementation* are the two key methods of impurity doping [7].

Until the early 1970s, all impurity doping was done mainly by diffusion (Figure 7a) at elevated temperatures. In this method, the dopant atoms are placed on or near the surface of the wafer by passing a gas mixture that contains the desired dopant through it. The doping concentration decreases monotonically from the surface, and the profile of the doping distribution is determined mainly by the temperature and diffusion time.

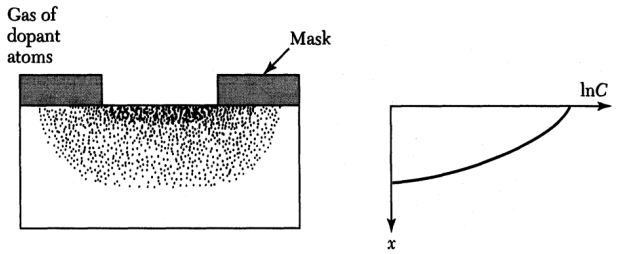

(a) Diffusion

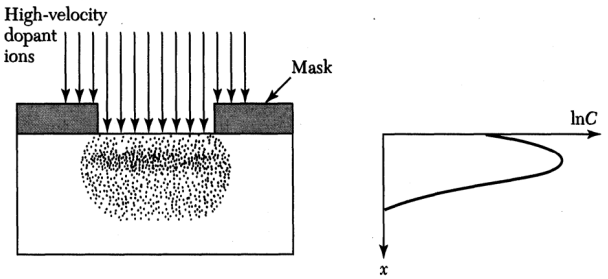

(b) Ion-implementation

Figure 7.: Comparison of techniques for the selective introduction of dopants into the semiconductor substrate. [7]

Since the early 1970s, many doping operations have used ion implementation (Figure 7b). In this process, the ion atoms with energies between 1 keV and 1 MeV are implanted into the semiconductor by means of an ion beam, resulting in ion distributions with average depths ranging from 10 nm to 10 μm . The doping concentration has a peak distribution inside the semiconductor, and the profile of the dopant distribution is determined mainly by the ion mass and the implanted-ion energy. The main advantages of ion implantation are its more precise control and scalability of impurity dopings and its lower processing temperature than the diffusion process.

Diffusion and ion implementation are used for device fabrication because these processes generally complement each other. For example, diffusion is used for deep junctions, whereas ion implementation is used for shallow junctions.

Diffusion

Figure 8 shows the contours of constant doping concentration for a constant-surface-concentration diffusion situation. We see from this curve that the lateral penetration is about 80% of the penetration in the vertical direction for concentrations three or more orders of magnitude below the surface concentration. Similar results are obtained for a constant-total-dopant diffusion condition, where the ratio of lateral to vertical penetration is about 75%.

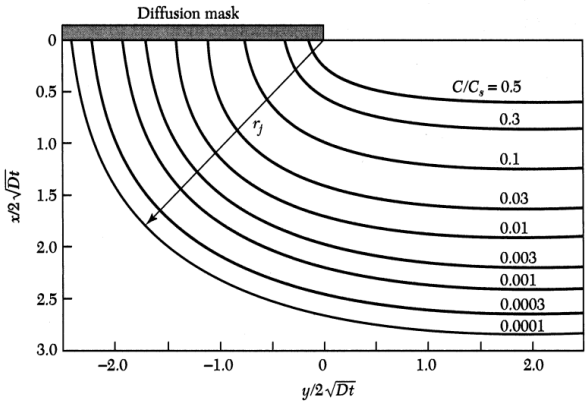

Figure 8.: Diffusion at the edge of an oxide window. r_j is the radius of curvature and C_S the surface concentration. [7]

Because of the lateral-diffusion effect, the junction consists of a central plane (or flat) region with approximately cylindrical edges with a radius of curvature r_j, as shown in Figure 8. Since the electric-field intensities are higher for cylindrical

and spherical junction regions, the breakdown voltages (See section 2.3.2) of such regions can be lower than that of a plane junction having the same background doping.

Implantation

The total distance an ion travels in coming to rest is called *range* R and is illustrated in Figure 9. The projection of this distance along the axis of incidence is called the *projection range* R_p. Because the number of collisions per unit distance and the energy lost per collision are random variables, there will be a spatial distribution of ions having the same mass and the same initial energy. The statistical fluctuations in the projected range are called the *projected straggle* σ_p. There are also statistical fluctuations along an axis perpendicular to the axis of incidence, called the *lateral straggle* $\sigma_\perp$.

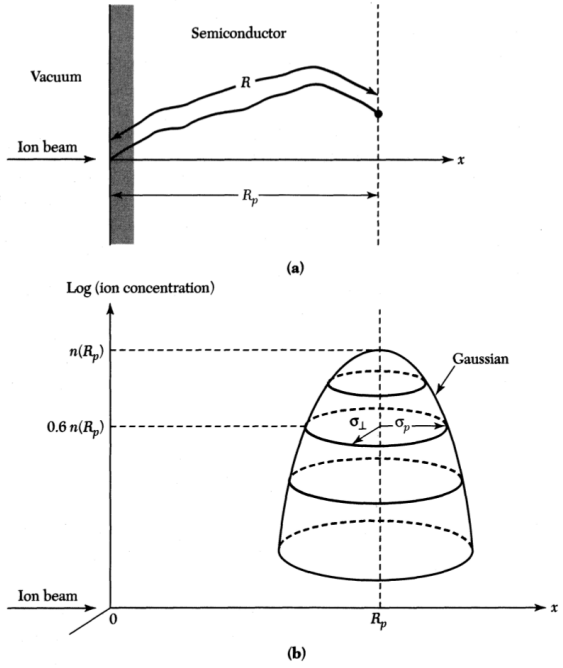

Figure 9.: (a) Schematic of the ion range R and projected range R_p. (b) Two-dimensional distribution of the implanted ion. [7]

Figure 9 shows the ion distribution. Along the axis of incidence (x), the implanted impurity profile can be approximated by a Gaussian distribution function:

$$n(x) = \frac{S}{\sqrt{2\pi}\sigma_p} e^{-\frac{(x-R_p)^2}{2\sigma_p^2}} \tag{9}$$

Where S is the ion dose per unit area. The maximum concentration is at the projected range R_p, and is reduced by 40% from its peak value at (x - R_p) = $\pm\sigma_p$.

Along the axis perpendicular to the axis of incidence, the distribution is also a Gaussian function of the form $\exp(\frac{-y^2}{2\sigma_\perp^2})$. Because of this distribution, there will be some lateral implantation, however, is considerably smaller than that from the thermal diffusion process.

Metallization

Making electrical contact with doped regions requires metallization. The Fermi level of the contact must be compatible with the semiconductor to ensure a non-rectifying ("ohmic") contact [6] [29]. This is often a problem with large bandgap semiconductors.

Metal films such as aluminum (Al) and its alloys are used extensively in Si detectors and IC to form low-resistance interconnections and ohmic contacts. Because Al and its alloys have low resistivities, 2.7 Ωcm for Al and up to 3.5 Ωcm for its alloys, these metals satisfy the low-resistance requirements. Al also adheres well to SiO_2.

2.3. Working Principle of a Silicon Tracking Detectors

Electron-hole (e-h) pairs are created when a particle hits the detector ($\sim 10^4$). In undepleted silicon detectors with a high number of free charge carriers ($\sim 10^9$), the created e-h pairs would quickly recombine, generating only a small signal in the electrodes. Additionally, the free-charge carriers would have a larger contribution to the signal, complicating the process of separating the signal from the noise. Meanwhile, in depleted semiconductor detectors, reversely biased, a large depletion zone is created that reduces the flow of the free charge carriers through the junction, and the electric field will drift the e-h pairs created for the particle to the electrodes producing a large current signal.

2.3.1. The pn-junction

When bringing p- and n-type semiconductors in contact, a so-called pn-junction is formed. PN-junctions are essential in semiconductor detectors and are also used extensively in rectification, switching, and other operations in electronic circuits.

[6] The Ohmic contact is a low resistance junction that provides current conduction from metal to semiconductor and vice versa. Theoretically speaking, the current should increase/decrease linearly with the applied voltage. With an immediate response for any small voltage.

Space charge

In Figure 10, a p- and n-type semiconductor are joined together, leading to carrier diffusion J(diffusion) due to the carrier concentration gradients at the junction. Holes from the p-side diffuse (J_p(diffusion)) into the n-side (letting acceptor atoms near the junction negatively charged), and electrons from the n-side diffuse (J_n(diffusion)) into the p-side (letting donors atoms near the junction positively charged). A negative space charge is formed near the p-side and a positive space charge near the n-side. This leads to a zone free of charge carriers called the **depletion zone**.

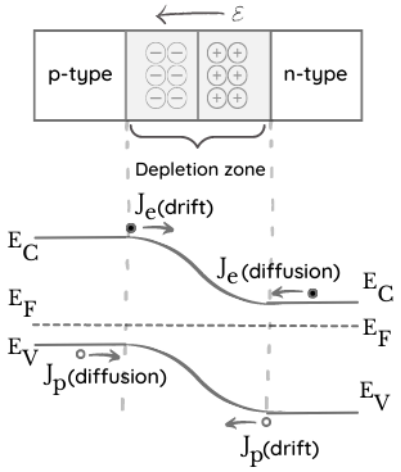

Figure 10.: Depletion region representation and energy band diagram for a pn-junction at thermal equilibrium.

The space charge region creates an electric field ($\mathcal{E}$) directed from the positive space charge toward the negative space charge. The electric field creates a drift current J(drift) from the positive space charge to the negative space charge for the holes (J_p(drift)) and in the opposite direction for the electrons (J_e(drift)). The created electrostatic potential causes the energy levels to bend across the boundary, whereas at thermal equilibrium[7], the Fermi level remains constant, as shown in Figure 10.

Electric Field

The electric field created for the space charge region is represented in Figure 11 and is given by the one-dimensional Maxwell equation for the electric field as:

[7]Steady-state condition at a given temperature without any external excitations.

$$\frac{d\mathcal{E}}{dx} = \frac{\varrho}{\varepsilon} = \frac{q(N_D + p) + (-q)(N_A + n)}{\varepsilon} = \frac{q}{\varepsilon}(N_D - N_A + p - n) \tag{10}$$

Where ϱ is the charge density, and ε is the permittivity of the medium. The electric field cancels outside the depletion region since the charge neutrality is maintained in regions away from the junction (ϱ=0). Within the depletion zone, the mobile carrier density is zero (n=p=0) and $N_D \gg N_A$ for the n-type and $N_A \gg N_D$ for the p=type, the electric field resulting in:

$$\mathcal{E}(x) = -\frac{q}{\varepsilon}N_A(x + x_p) \qquad -x_p \leq x < 0 \tag{11.1}$$

$$\mathcal{E}(x) = \frac{q}{\varepsilon}N_D(x - x_n) \qquad 0 < x \leq x_n \tag{11.2}$$

The maximum electric field is at x = 0 and can be expressed as:

$$\mathcal{E}_{max} = -\frac{q}{\varepsilon}N_A x_p = -\frac{q}{\varepsilon}N_D x_n \tag{12}$$

Electrostatic Potential

The electrostatic potential (ψ), given by Poisson's equation:

$$\frac{d^2\psi}{dx^2} = -\frac{d\mathcal{E}}{dx} = -\frac{\varrho}{\varepsilon} \tag{13}$$

result in

$$\psi(x) = -\frac{q}{2\varepsilon}(N_D - N_A + p - n)(x \pm x_{p/n})^2 + \psi_{p/n} \tag{14}$$

Due to the charge neutrality away from the junction (ϱ=0), equation 14 outside the depletion junction result in:

$$\psi(x) = \psi_{p/n} = -\frac{1}{q}(E_i - E_F))|_{-x_p > x > x_n} \tag{15}$$

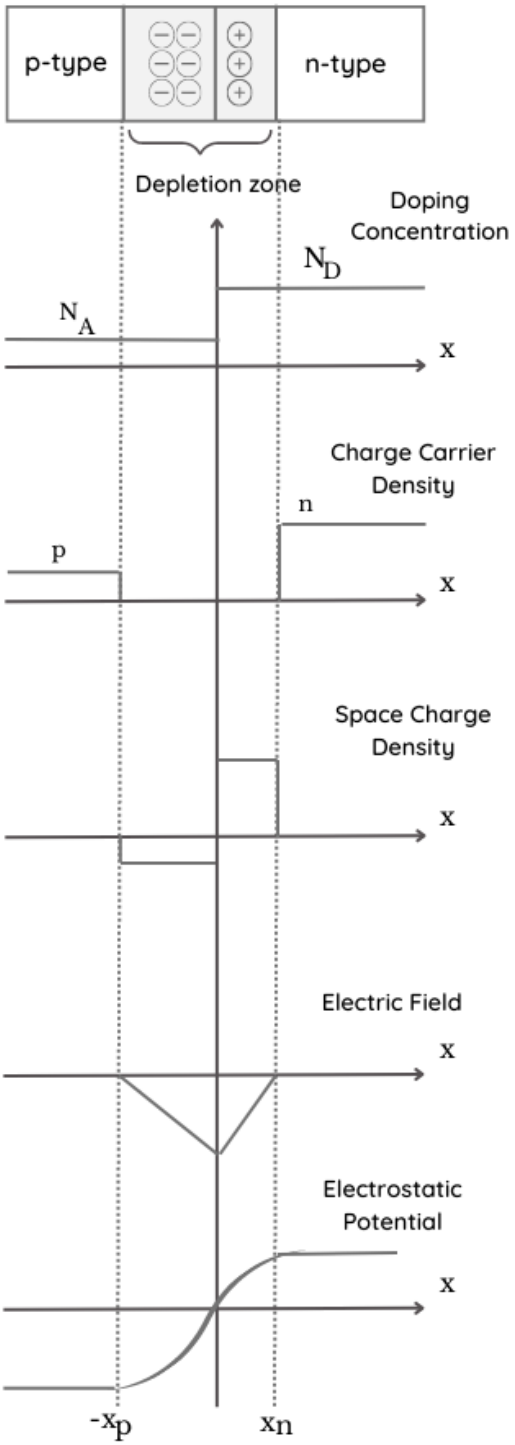

Figure 11.: Doping concentration, charge carrier concentration, space charge density, electric field, electrostatic potential for a pn-junction.

The potential is quadratic over the depletion zone and constant outside, as shown in Figure 11. For the neutral regions, the electrostatic potential with respect to the constant Fermi level (E_F), designated as $\psi_{p/n}$, can be obtained by setting N_D=n=0 and N_A=p=0 in equation 6 as:

$$\psi_n = \frac{kT}{q} ln(\frac{N_A}{n_i})|_{x<-x_p} \tag{16.1}$$

$$\psi_p = -\frac{kT}{q} ln(\frac{N_D}{n_i})|_{x>x_n} \tag{16.2}$$

Built-in Potential

The total electrostatic potential difference between the p-side and the n-side neutral regions (voltage drop over the depletion zone) at thermal equilibrium is called the *built-in potential* V_{bi}:

$$V_{bi} = \psi_n - \psi_p = \frac{kT}{q} ln(\frac{N_D N_A}{n_i^2}) \overset{\text{Si}}{\approx} 0.4 - 0.8\,V \tag{17}$$

Depending on x_p and x_n the voltage V_{bi} can be written using equations 11 as:

$$\begin{aligned} V_{bi} &= -\int_{-x_p}^{x_n} \mathcal{E}(x)dx = -\int_{-x_p}^{0} \mathcal{E}(x)dx - \int_{0}^{x_n} \mathcal{E}(x)dx \\ &= \frac{qN_A x_p^2}{2\varepsilon} + \frac{qN_D x_n^2}{2\varepsilon} \end{aligned} \tag{18}$$

Using equation 12, equation 18 turn into

$$V_{bi} = -\frac{1}{2}\mathcal{E}_{max}(|x_p| + |x_n|) \tag{19}$$

Depletion layer width

The depletion layer width ($W=|x_p|+|x_n|$) can be expressed in function of the built-in potential using the charge neutrality outside of the depletion region ($-N_A x_p = N_D x_n$) and equations 19 and 12 as:

$$W = \sqrt{\frac{2\varepsilon}{q}(\frac{N_D + N_A}{N_A N_D})V_{bi}} \tag{20}$$

2.3.2. The pn-junctions under external voltage

The width of the depletion zone changes under the application of an external voltage (V_{ext}), depending on the polarity and the size of the voltage, as shown in Figure 12.

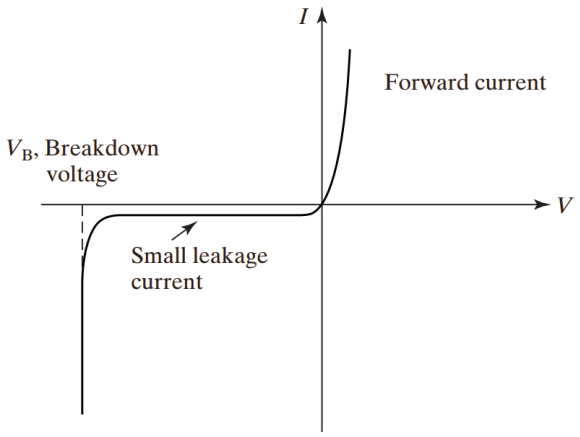

Figure 12.: Current-voltage characteristics of an ideal silicon pn-junction.

Forward Bias

When a positive voltage is applied to the p-side of the junction relative to the n-side ("forward bias"), the current through the junction increases rapidly as the voltage increases, as shown in Figure 12. The current starts to flow when the external voltage exceeds the built-in potential. The diffusion current is enhanced since the external voltage moves away the majority charge carriers through the junction (more electrons diffuse from the n-type material to the p-type material and more holes from the p-side to the n-side). Before crossing the depletion region, some of the charge carriers find the ions in the space of charge, recombine, and the atoms become neutral, thinning the depletion zone. Thus the space charge region decreases as well as the electrostatic potential difference between the n-side and p-side ($V=V_{bi}-V_{ext}$) as shown in Figure 13a.

Reverse Bias

However, when the external voltage is applied so that the p-side voltage is negative

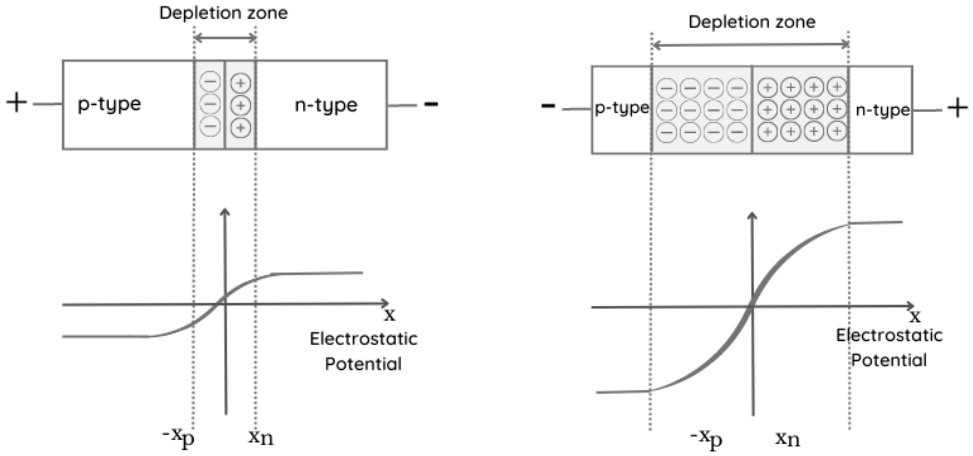

(a) Forward Bias **(b) Reverse Bias**

Figure 13.: Illustration of the changing width of the depletion region and the potential difference across the pn-junction for different polarities of the applied external voltage.

relative to the n-side ("reverse bias"), practically no current flows initially, as shown in Figure 12. In this case, the minority charge carriers are injected into each side of the junction, attracting the majority charge carrier, which leaves behind an ionized atom. Thus the space charge region increase as well as the electrostatic potential difference between the p-side and n-side ($V=V_{bi}+V_{ext}$) as shown in Figure 13b.

These positive ions at the n-side of the pn-junction oppose the flow of free holes from p-type material, and negatively charged in the p-side oppose the flow of free electrons from the n-side. Only the minority charge carriers attracted towards the opposite space of charge contribute to the electric current. Since the electric current carried by the minority charge carriers is so small, it is considered negligible in theory. As the external voltage increases, the current remains very small until a critical voltage is reached, where the current suddenly increases. This point is known as the *breakdown voltage*. The critical *breakdown voltage* can vary from just a few volts to thousands of volts depending on the doping concentration and other device parameters.

The current shows an exponential dependence on the externally applied voltage and can be calculated using the Shockley equation [30]:

$$I = I_S(e^{\frac{qV}{kT}} - 1) \tag{21}$$

Where the current created after the breakdown voltage is not included and I_S the reverse saturation current [17].

$$I_S \approx qA(\frac{D_n n_i^2}{L_n N_A} + \frac{D_p n_i^2}{L_p N_D}) \tag{22}$$

A represents the cross-sectional area, $D_{n/p}$ the diffusion constants, and $L_{n/p}$ the carrier diffusion lengths.

Leakage current

In no-ideal diodes, the current created for the diffusion of minority charge carriers is not the only source of leakage current (I_S) in reverse bias. Volume and surface contributions originate from different sources. The most important cause of volume contribution originated from the thermal generation of e-h pairs in the depletion zone (I_V^{gen}), and its size is determined by the presence of impurities that can act as generation/recombination centers. The generated charges inside the depletion zone can be moved for the high electric fields toward the electrode before recombining.

$$I_V^{gen} = qAW\frac{n_i}{\tau_g} \tag{23}$$

Where τ_g represents the charge carrier generation lifetime[8]. Because n_i has a temperature dependence ($n_i \propto T^{\frac{3}{2}} e^{\frac{-E_G}{2kT}}$) I_V^{gen} and I_S also depend on the temperature. At low temperatures, the generation current dominates, and the leakage current varies as $I_V^{gen} \sim \sqrt{V_{ext}}$. As the temperature increases, the generation current demonstrates a saturation tendency; at this point, the diffusion current becomes dominant. The generation current is also saturated when full depletion is reached. [7].

Surface contribution to the leakage current originates from damage on the detector surface during the fabrication process or the handling of the detector. It can be distinguished from volume current due to the linear proportionality with the voltage, a difference of the quadratic dependence of volume contribution.

Junction breakdown

The junction will conduct very large currents when a critical breakdown point is reached. Even though this current isn't necessarily destructive, excessive created heating can destroy the circuits, so the maximum current need to be limited.

The tunneling effect [7] is one of the mechanisms that can cause these large currents.

[8]Time constant needed for the generated charge carriers to return to the equilibrium state.

In this process, electrons can move from the valence band to the conduction band, even if their energy is much lower than the barrier height. In the case of silicon, breakdown voltages of less than $\sim 4E_g/q$ are attributed to the tunneling effect.

For pn-junctions with breakdown voltages higher than $\sim 6E_g/q$, the large currents result from the avalanche multiplication mechanism [7]. In this process, thermally generated electrons in the depletion zone gain enough kinetic energy from high electric fields that in a collision with atoms from the crystal, can break the lattice bounds and crate a secondary electron-hole pair that will continue the process of creating more electron-hole pairs. For this case, the breakdown is defined as the voltage where the multiplication factor[9] approaches infinity and is defined as:

$$\int_0^W \alpha dx = 1 \tag{24}$$

Where α denotes the avalanche ionization rate. Breakdown voltages between $4E_g/q$ and $6E_g/q$ are the result of currents created by both mechanisms.

Junction capacitance

Capacitance is the property that describes how much electric charge can be stored in an object for a given applied voltage (dQ/dV). Due to the charge stored inside the depletion zone, pn-junctions work as a parallel-plate capacitor. Typically, the capacitance of a pixel detector can range from a few femtofarads (10^{-15} F) to several tens of femtofarads. High capacitance can lead to higher detector noise, low signal-to-noise ratio, and a shift in the detector's frequency response, so minimizing the capacitance is often a design goal for pixel detectors.

The capacitance of a pixel detector depends on several factors, such as the detector's size, the detector substrate's thickness and material, and the type of readout circuitry used. In general, the capacitance of a pixel detector can be modeled as the sum of the junction capacitance (C_j), the inter-pixel capacitance (C_i), the p-well capacitance (C_p), other small contributions, and the capacitance of the readout electronics (determined by the circuitry design and can be minimized by using low-capacitance transistors and minimizing the length of the interconnects).

The junction capacitance is directly proportional to the area (A) and inversely proportional to the thickness (d), where d=W:

[9] Ratio between the current gained through the junction due to the avalanche multiplication and the initial current.

$$C_j = \frac{\varepsilon A}{d}[F] \tag{25}$$

or

$$\frac{1}{C_j^2} = \frac{2}{\varepsilon q A^2}\left(\frac{N_A + N_D}{N_D N_A}\right)(V_{bi} + V_{ext}) \tag{26}$$

From equation 26, we can see that a plot of $\frac{1}{C_j^2}$ versus V_{ext} produces a straight line, where the slope depends on the acceptor and donor concentration, and the intercept at 0 gives the built-in potential.

Full depletion voltage

Since C_j depends on the depletion volume, measuring C_j allows determining the full depletion voltage (voltage necessary to deplete the entry sensor volume). Given that the depletion zone can't grow larger than the thickness of the detector when the full depletion is reached, $\frac{1}{C_j^2}$ will stay at a constant value, as shown in Figure 14.

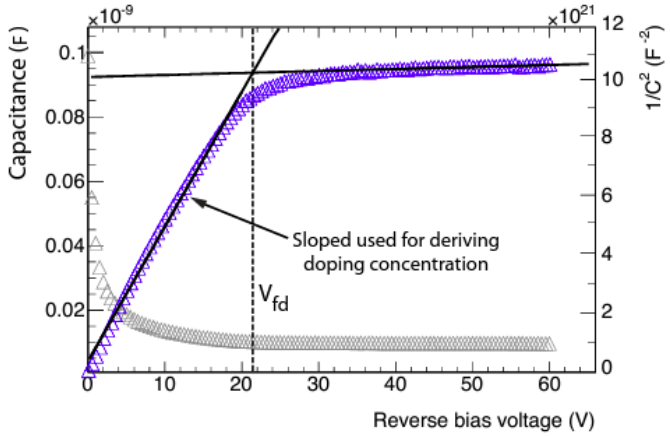

Figure 14.: Determination of the full depletion voltage from a measurement of the diode capacitance as a function of the applied voltage. $\frac{1}{C_j^2}$ is represented by the blue triangles. [19]

2.3.3. Metal-Semiconductor Interface

The metal-semiconductor interface is the point at which a metal and a semiconductor material meet and create a boundary between them. This interface is a crucial component in the functioning of Si sensors and is designed to connect the sensor to

external circuitry. A metal-semiconductor interface is typically created by depositing a metal layer, such as aluminum, on the surface of a Si substrate (as discussed in section 2.2). The charge transfer between metal and semiconductor exists in a very narrow region in the metal and in the semiconductor side is proportional to $\sqrt{V}$. The maximum electric field at the interface decreases linearly with distance.

Si semiconductor detectors can be designed with either Schottky or ohmic contacts, depending on the specific application requirements. The main difference between these two contact types is how they control current flow across the metal-semiconductor interface. Schottky contact exhibits rectifying behavior, characterized by a potential interface barrier that prevents current flow in one direction. In contrast, an ohmic contact allows current flow in both directions. The metal layer forms a low-resistance contact with the semiconductor material, with no potential barrier at the interface.

The electrical contacts made to the Si detector must be ohmic to make accurate measurements. This is important because it allows for accurate and precise measurements of the electrical signals produced by the detector. A non-ohmic contact would have a nonlinear current-voltage relationship, introducing measurement errors and inaccuracies. This is because the current flowing through the contact would not be directly proportional to the voltage applied across it, making it difficult to accurately determine the signal produced by the detector.

2.3.4. Oxide-Semiconductor Interface

Passivation refers to the process of protecting the surface of a semiconductor material from external contaminants and other factors that could degrade its performance. During the manufacturing process, the surface of the semiconductor material can become damaged or contaminated due to exposure to air or other environmental factors. This can create defects or impurities in the material, affecting its electrical properties. To prevent this, a thin layer of insulating material, typically silicon dioxide (section 2.2), is deposited on top of the semiconductor material. This layer acts as a protective barrier, shielding the surface of the semiconductor from external contaminants and preventing impurities from diffusing into the material.

The interface between semiconductors and insulators is a critical feature of many electronic devices. Even if no free carriers are on the oxide side, charged ions and holes trapped near the interface pull the free electrons of the semiconductor toward the insulator creating an electron accumulation layer at the oxide-semiconductor boundary. The presence of charges at the interface can create an electric field that affects the behavior of detectors.

2.4. Interaction of Particles with Matter

It is only through interaction with matter that particles can be sensed. Particles can interact with matter through several mechanisms and depend on the particle's properties and the matter it interacts with.

Charged particles can interact with matter through Coulomb interactions, ionization, and excitation. Coulomb interactions occur when charged particles interact with the electric fields of the atomic nuclei and electrons, resulting in deflection from their original path. Ionization occurs when charged particles transfer enough energy to an atom or molecule to remove one or more electrons, creating ions. Excitation occurs when charged particles transfer energy to an atom or molecule, resulting in the excitation of electrons to higher energy states.

The average energy loss per path of the particle is described by the Bether-Bloch formula [31, 32]:

$$-\left\langle \frac{dE}{dx} \right\rangle = Kz^2 \frac{Z}{A} \frac{1}{\beta^2} \left[\frac{1}{2} \ln \frac{2m_e c^2 \beta^2 \gamma^2 T_{max}}{I^2} - \beta^2 - \frac{\delta(\beta\gamma)}{2} \right]$$

With:

$K = 4\pi r_e^2 m_e c^2 N_A \approx 0.307$ MeVcm^2/mol, with m_e and r_e being the rest mass and the classical radius of the electron

z, $\beta = v/c$ are the charge number and relative velocity of the projectile particle

Z, A are the atomic number and atomic mass number of the material

I is the mean excitation energy of the material

T_{max} is the maximum kinetic energy transfer to a free electron in a single collision

$\delta(\beta\gamma)$ is the density correction

For the case of electrons and positrons, this formula must be modified to account for the small mass and the indistinguishability of incident and scattering electrons.

The stopping power ($\frac{dE}{\rho dx}$) determines the range of a particle in matter or the energy loss after penetration. Figure 15 shows the mean energy loss of pions in silicon as a function of $\beta\gamma$. Between β approximated 3-4, there is a minimum. Particles in this kinematic range are called Minimum Ionizing Particle (MIP).

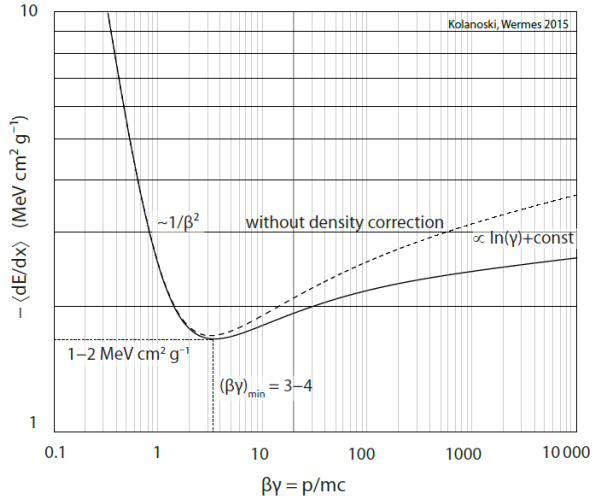

Figure 15.: Density weighted mean energy loss of charged pions in silicon as a function of $\beta\gamma = p/mc$ [17].

Delta electrons, also called delta-rays (δ-rays), are also created in the path of particles through matter. These are created in a central collision of an incident particle with a shell electron. They are characterized by kinetic energy sufficiently large to cause secondary ionization and contribute to the tail of the energy loss spectrum (as shown in Figure 16). They can traverse a significant distance within the detector material and thus lead to outliers in the measured energy spectrum and the spatial position measurement of the incident particle.

The energy loss process has a statistical fluctuation. The energy loss ΔE along a distance Δx comprises many small contributions corresponding to individual ionization or excitation processes. This leads to an asymmetric distribution with a Gaussian part corresponding to the small energy losses and a tail for large energy losses. From this distribution, we can distinguish the most probable value (mpv) of the energy loss, that is, the maximum of the distribution and the average value ($\frac{dE}{dx}$) situated to the right of the mpv by an amount depending of the asymmetry of the distribution.

Radiative losses cannot be neglected for light-charged particles such as electrons and positrons. At low velocities, energy loss mainly results from inelastic collisions with the shell electrons, leading to excitation and ionization similar to heavily charged particles. For relativistic velocities, the mean energy loss is almost exclusively given by bremsstrahlung, which occurs when a charged particle is accelerated in the electric field of the nucleus and is the emission of individual photons accounting for the total

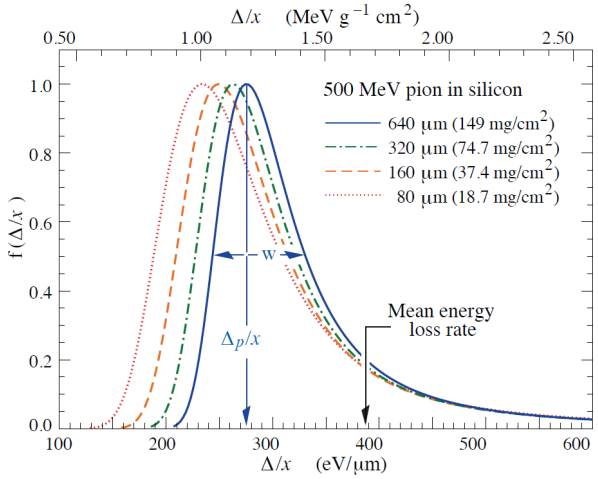

Figure 16.: Energy loss rate of a MIP in silicon for different thicknesses given by the Landau distribution. The mean value, described by the Bethe-Bloch formula, is independent of material thickness, while the most probable value changes scales with it [33].

momentum change of the electron. This leads to an exponential decrease in the particle energy, according to

$$\left(\frac{dE}{dx}\right)_{\textbf{ion.}} = -\frac{E}{X_0} \tag{28}$$

Where X_0 is a characteristic property of the absorber material, defined as the average length over which a high-energy electron loses 1/e of its energy due to bremsstrahlung.

2.5. Transport of Charge Carriers and Signal Formation

The previous section showed how free charge carriers are created when charged particles pass through matter. After the creation of the free electrons and holes, the transport process starts. The transport process includes drift, diffusion, recombination and generation. Some of these mechanisms are shown in Figure 17 and presented in this section.

2.5.1. Drift

The thermal motion of the free charge carriers is characterized by a succession of random scattering from collisions with lattice atoms and impurities. The average

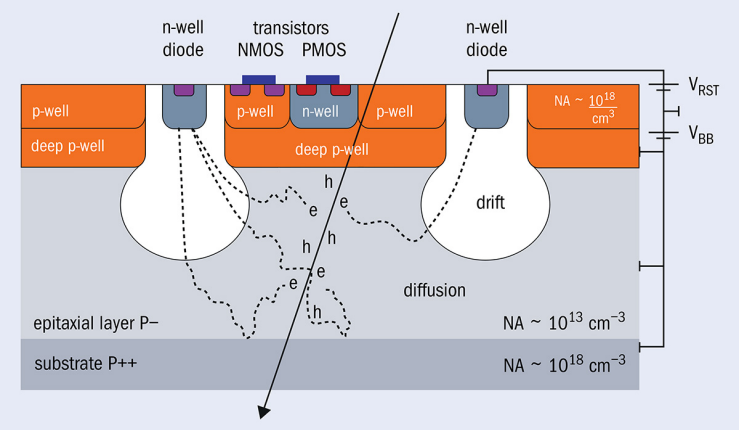

Figure 17.: A schematic cross-section of the ALPIDE chip.

distance between collisions is called the mean free path (ι), and the average time mean free time (τ_c). When an electric field is applied to a semiconductor sample, the free charge carriers will be accelerated. This additional component to the velocity is called drift velocity and is defined as:

$$\upsilon_D = \frac{q\tau_c}{m_{\text{eff}}}\mathcal{E} = \pm\mu_{n,p}\mathcal{E} \tag{29}$$

Where q is the unit charge and m_{eff} is the effective mass. In silicon, τ_c is in the picosecond range and depends strongly on temperature and impurity concentration as $(\frac{T^{3/2}}{N})$ [17]. The parameter $\mu = \frac{q\tau_c}{m_{\text{eff}}}$ is known as mobility. The mobility of electrons and holes differs due to their effective mass. In silicon, at room temperature, the electron mobility is about three times larger than the hole mobility [17].

In equation 29 τ_c was assumed to be independent of the electric field. This assumption can be used as long as the drift velocity is small compared with the thermal velocity ($\approx 10^7$ in Si at room temperature). As the drift velocity approaches the thermal velocity, the field dependency moves from the linear dependence, as shown in Figure 18 approaching a saturation velocity. This effect is related to the inelastic interaction of the free carriers with optical phonons at sufficiently large electric fields.

2.5.2. Diffusion

Another important current component can occur if there is a special carrier concentration variation. The free carriers tend to move from the region of high to the region of small concentration. This current component is called diffusion current, which

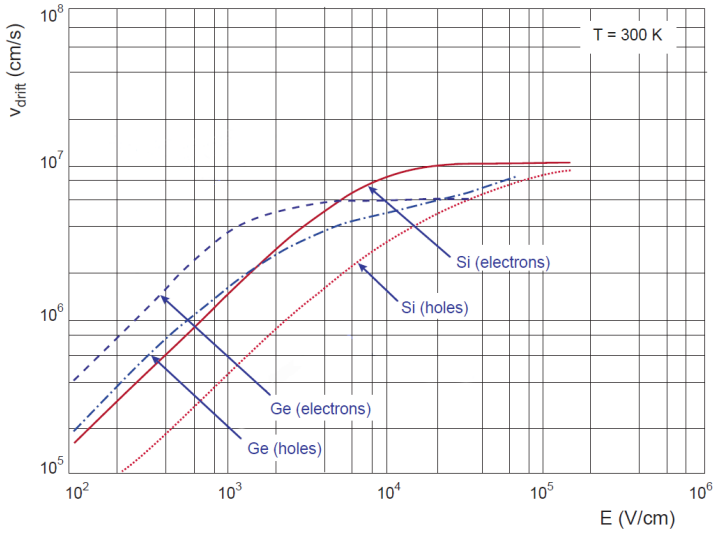

Figure 18.: Electron and hole drift velocity in silicon as a function of the applied electric field at room temperature (adapted from [17]).

according to Fick's First law, takes the form:

$$J_{n,p} = \pm q D_{n,p} \frac{n,p}{dx} \tag{30}$$

D_n is called diffusion coefficient or diffusivity and is equal to:

$$D_{n,p} = (\frac{kT}{q})\mu_{n,p} \tag{31}$$

2.5.3. Charge Induction

By separating the ionization charges in an electrical field, electrical signals can be produced on external electrodes, which can be further electronically processed. The moving charge induces an accumulation of charges on the electrode surfaces; therefore, it is not important for the signal formation that the charge actually arrives at the electrode.

The calculation of the induced charge is based on the Shockley-Ramo Theorem [34, 35]. The theorem states that the induced current i_s and the accumulated charge Q on the electrode are:

$$i_s = q\upsilon\mathcal{E}_w \quad \text{and} \quad Q = -q\Delta\phi_w \tag{32}$$

Where υ is the velocity of the charge. $\mathcal{E}_w$ and ϕ_w are the weighting field and weighting potential, the electric field and potential that would exist at q's instantaneous position x under the following circumstances: the selected electrode at unit potential, all other electrodes at zero potential and all charges removed.

The induced charge on the electrode is independent of the trajectory of the carrier towards the electrode and only depends on the beginning and end positions. It should be emphasized that the weighting field depends only on the geometrical electrode configuration and, thus, differs from the electric field. The weighting potential is dimensionless, and the weighting field has the dimension 1/length. The detector signal is the integral over time of the induced current within the integration time of the amplifier.

In pixels sensors, charges traveling close to the readout electrode will induce a higher signal for a given displacement Δx than carriers traveling the same Δx but further from the readout electrode. Consequently, the carriers drifting toward the sensing electrode contribute more to the detector signal. The entire signal is not measured if the integration time is shorter than the total drift time or if carriers get recombined or trapped.

Chapter 3

HV-MAPS for Particle Physics Experiments

3.1. Pixel detector technologies

Pixel detectors are advanced sensing devices that have become essential tools for particle physics, astronomy, and medical imaging applications. These detectors offer high granularity and are designed to detect and measure the properties of individual particles with high spatial resolution and efficiency. A Schematic drawing of a one-pixel cell is sketched in Figure 19.

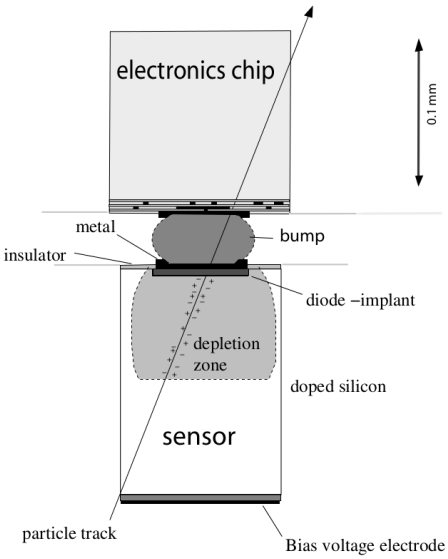

Figure 19.: Schematic drawing of a one-pixel cell of a hybrid pixel sensor. [28]

Structured electrodes allow for space-point determination of the particle traversal. As discussed in Chapter 2, when a particle crosses a semiconductor detector, it loses energy through many collisions with the electrons and nucleus of the semiconductor. These collisions potentially generate free electron-hole pairs. The free charges move via drift in the electric field created inside the depletion zone toward the electrodes, inducing a signal that is processed by custom-design circuits. During the drift, the charges do not exactly follow the electric field lines but also diffuse due to the random thermal motion in the crystal lattice. The spread of the arrival position of the charge due to this effect can be described as a Gaussian distribution with standard deviation [36]:

$$\sigma = \sqrt{2Dt} \tag{33}$$

Where D (See subsection 2.5.2) is the diffusion constant, and t is the carriers' transit time. This results in a spread of a few micrometers at the collecting electrode. If only digital information is available ($1 = hit$, $0 = no\,hit$), the electrode pitch determines the resolution. The average quadratic deviation (the variance) from the true entrance point for perpendicular particle incidence and single hit response is [17]:

$$\begin{aligned} \sigma_x^2 &= \frac{1}{p}\int_{-p/2}^{p/2} x^2 x = \frac{p^2}{12} \\ \sigma_x &= \frac{p}{\sqrt{12}} \end{aligned} \tag{34}$$

A so-called cluster is formed if the signal charge is shared by two (or more) pixels. The occurrence of clusters improves the resolution for particles passing through the region between two pixels [1]. For the events triggering two pixels, one expects a resolution of $s/\sqrt{12}$ [17], where s is the area between two n-well. For the events triggering only one pixel, $(p-s)/\sqrt{12}$. For analog readout, if two or more pixels fire, the signal can be used to precisely determine the entrance point by weighted averaging of pixel signals. However, the resolution is still limited to $(p-s)/\sqrt{12}$ in the region where only one-pixel fires. For this reason, one tries to expand the region of charge sharing in the inter-pixel region as far as possible by tilting the detector.

Some of the pixel detector technologies developed over the last years are explored in this chapter, especially High Voltage Monolithic Active Pixel Sensors (HV-MAPS).

[1] Refer to as inter-pixel region/area during the following discussions.

3.1.1. Hybrid Pixel Detectors

Hybrid pixel detectors [37] consists of a silicon pixel detector and custom-designed readout electronics, which are fabricated separately and then bonded together to form a hybrid structure (as shown in Figure 20). The pixel detector serves as the sensing element, detecting particles and converting them into electrical signals. The readout electronics then amplify and digitize the signals, allowing for the reconstruction of particle tracks with high resolution and accuracy.

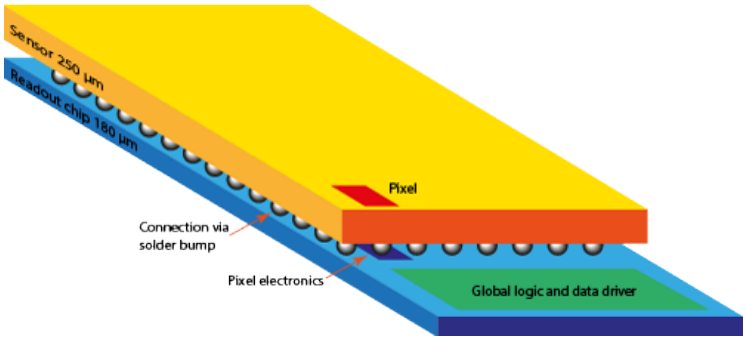

Figure 20.: Schematic of a hybrid pixel sensor. Pixel sensor (yellow) connected to the readout chip (blue) via solder bump.

One of the key advantages of hybrid detectors is their high granularity and fast readout speeds, which enable them to accurately detect and track particles even in high-rate environments. Hybrid detectors also offer excellent energy resolution and timing performance, making them ideal for various high-energy physics experiments, such as the Large Hadron Collider (LHC).

The disadvantages of the hybrid technique become evident when one addresses the requirements of particle detectors at future high-energy accelerators, particularly the demands on high resolution in high-multiplicity environments while maintaining low material budget and high speeds. The technological limitations are mostly related to the bump technology and the power density associated with the constraint that the electronics circuitry for amplification and logic is confined to the same area as the detecting electrode.

3.1.2. Monolithic Active Pixel Detectors

More recently, the development of monolithic pixel sensors has revolutionized the field of particle detection. Monolithic pixel detectors [17] integrate the sensing volume and the readout electronic in a single piece of semiconductor material. The

detector and readout electronics are fabricated in a single process step, simplifying the manufacturing and resulting in a compact device.

Compared to hybrid detectors, monolithic detectors offer several advantages. First, they have a smaller form factor and are easier to integrate into complex detector systems. Second, they have a lower material budget, which is important for applications where minimizing multiple scattering is critical. Finally, monolithic detectors have lower power consumption and produce less heat, which can benefit applications with limited power and cooling.

Monolithic active pixel sensors (MAPS) are advanced monolithic pixel detectors featuring integrated amplifiers within each pixel cell. Figure 21 illustrates an example of the MAPS concept.

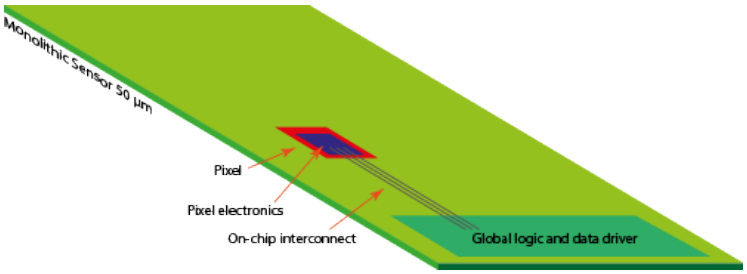

Figure 21.: Schematic of a MAPS. The readout electronic is integrated into each pixel cell. Pixels are connected to the periphery through a signal line.

MAPS are fabricated using standard Complementary Metal–Oxide–Semiconductor (CMOS)[2] technology, allowing for the integration of readout electronics directly onto the pixel array. This eliminates the need for complex and expensive hybridization processes, making MAPS more cost-effective and scalable than traditional pixel detectors. One downside of the MAPS is that they might not be suitable for high-rate applications since this technology's charge collection is mainly via diffusion.

3.2. High Voltage-Monolithic Active Pixel Sensors

High voltage monolithic active pixel sensors (HV-MAPS) [38] are a type of MAPS that operates at high bias voltages. The high bias voltage used in HV-MAPS creates larger depletions and stronger electric fields than traditional MAPS detectors, allowing a more efficient collection of the charge generated by the ionizing radiation. The high electric field results in fast charge collection via drift. The fast charge collection

[2]CMOS is a type of metal–oxide–semiconductor field-effect transistor fabrication process that uses complementary and symmetrical pairs of p-type and n-type MOSFETs for logic functions.

reduces the trapping probability of the free charge carriers (crucial mainly after long exposure to radiation), providing the sensors with intrinsic radiation hardness [39]. A schematic of an HV-MAPS is shown in Figure 22.

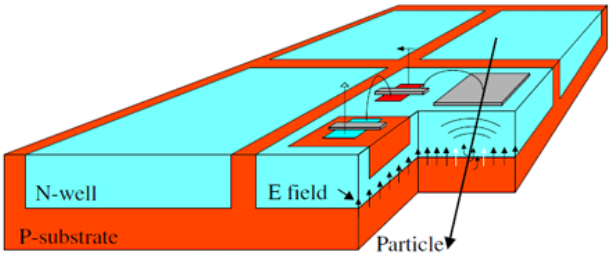

Figure 22.: Schematic drawing of a four-pixel sub-matrix of an HV-MAPS. Each pixel consists of a pn-junction with integrated electronics. Large depletion zones are created due to the high voltage operation. [38]

A deep n-well is implemented in a p-substrate to form the sensor diode (see Figure 23). The n-well works as a collection electrode, houses the in-pixel electronic and shields it from high electric fields.

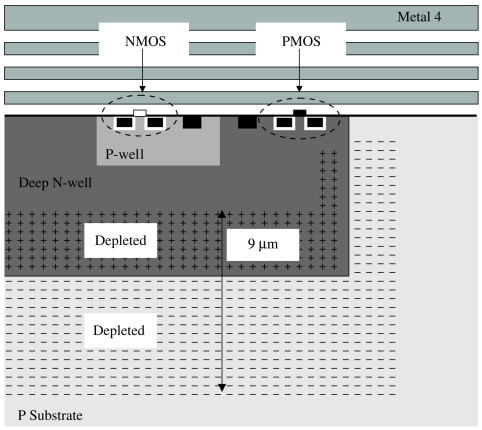

Figure 23.: HV-MAPS floating logic housed by the n-well. [38]

HV-MAPS are currently under research and development (R%D) to be implemented in particle physics experiments, where their high sensitivity and fast response make them well-suited for detecting charged particles and measuring their energy and position. However, HV-MAPS also have some limitations, including the high operating voltage that can lead to increased power consumption and heat generation [40]. They also require careful design to minimize the effects of crosstalk (see

subsection 5.3.1) between adjacent pixels, which can degrade the spatial resolution [3] and decrease the noise rate due to the large fill factors [4].

The signal-to-noise ratio (S/N) is defined from the collected charge (Q_{in}) and the detector capacitance (C_{det}) [28] as:

$$S/N \propto \frac{Q_{in}}{C_{det}} \tag{35}$$

and from equation 25, we see that $C_{det} \propto$ A. small collection electrodes decrease the noise and increase the S/N ratio. Furthermore, a high capacitance can also affect the time resolution [5]. An amplifier with a short rising time and a fast discriminator is desirable to improve the time resolution. The capacitance of the detector affects the amplifier's rising time because the charge collected in each pixel must be transferred to the amplifier through a readout circuit. The larger the capacitance, the longer the time it takes for the charge to be transferred to the amplifier, increasing the amplifier's rising time. The relationship between the capacitance and the amplifier's rising time can be expressed mathematically using the time constant (t_r):

$$t_r \propto \frac{C_{det}}{C_{FB}} \tag{36}$$

Where C_{FB} represents the amplifier feedback capacitance [41].

3.2.1. HV-MAPS Applications and Challenges

HV-MAPS are becoming increasingly important for particle physics experiments and are under study for implementation in several particle physics applications. This chapter discusses some of the applications and challenges of HV-MAPS.

Mu3e

Mu3e [42] is a particle physics experiment aimed at studying the charge lepton flavor violating decay $\mu^+ \rightarrow e^+e^-e^+$ if its branching fraction is larger than 10^{-16}, or otherwise to exclude a branching fraction of $> 10^{-16}$ at the 90% confidence level. To achieve these goals, more than 10^{17} muons must be stopped in a target, and any background mimicking the signal process must be suppressed to below the 10^{-16}

[3] Position resolution refers to the detector's capability to accurately determine the position of particle interactions within its sensitive volume.

[4] Large fill factor detectors refer to sensor designs that maximize the active area available for charge collection.

[5] Time resolution refers to the ability to accurately distinguish and resolve events that occur close together in time.

level. A schematic view of the experiment cut along the beam axis in phase I [6] is shown in Figure 24, where a muon beam is stopped by a hollow Mylar double cone target. The target is surrounded by four radial layers of HV-MAPS, which form the pixel tracker and measure the vertex position and bending radius of the electrons due to the 1 T magnet. The tracker is complemented by two timing detectors.

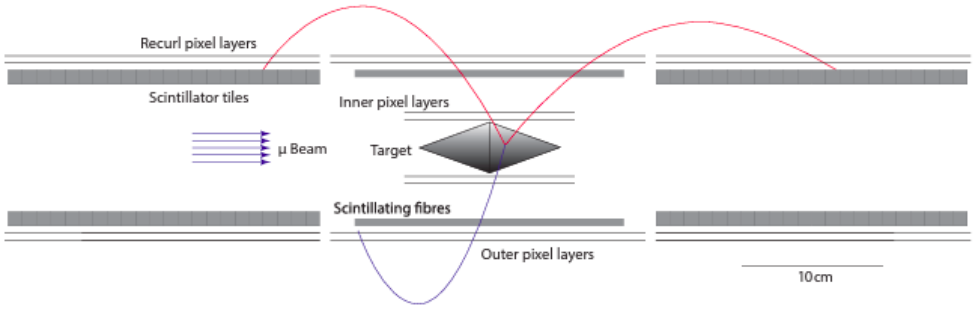

Figure 24.: Schematic view of the experiment cut along the beam axis in the phase I configuration. [42]. The muon target, tracking, and timing detectors are illustrated.

The energies of the decay particles range from the electron mass up to half the muon mass, which is about 53 MeV. At the energies of interest, multiple Coulomb scattering in detector material is the dominating factor affecting the momentum resolution. For this reason, the chosen pixel tracker must be designed with a thickness of 0.1% of the radiation length per layer. HV-MAPS is the only pixel sensor technology that provides high rate capability while allowing to thin of the sensor down to 50 µm.

One challenge associated with this application is minimizing crosstalk between adjacent pixels, which can degrade the spatial resolution. The sensors use specialized guard rings around each pixel to address this challenge and minimize the induced charge in neighbor pixels. In addition, to achieve the aimed Mu3e Phase II sensitivity, the pixel tracker must deal with a stopping rate of 10^9Hz muons decay per second. To further reduce combinatorial background without adding material, HV-MAPS must reach a time resolution of $\mathcal{O}(1\,\text{ns})$ [42].

LHCb

In the coming years, the Large Hadron Collider (LHC) at CERN [44] is being upgraded to work at higher luminosities, leading to the High-Luminosity LHC (HL-LHC) [45].

[6] The detector will be built in 2 phases. Phase I aims for a sensitivity of 10^{-15}. Phase II will use a new high-intensity beam under study at PSI [43], resulting in the aimed final sensitivity.

The LHC experiments will also be upgraded to handle the increased luminosity and data rate. LHCb PL(Large Hadron Collider beauty) [46] is one of the LHC experiments that seek to undertake new measurements with unprecedented precision in its search for new physics in CP-violating phenomena and rare decays in flavor physics.

Among the tracking systems, the Scintillating Fibre(SciFi) Tracker [47] simulation studies at increased luminosities result in an occupancy increase of up to 20% per fibre per event in the innermost region, a ghost rate of 90% and an efficiency of between 50% and 60% which are unacceptable for the performance of the tracker [48]. One of the proposed updates is the installation of the Mighty Tracker [49], a new hybrid tracking system shown in Figure 25. It consists of scintillating fibers in the outer regions and silicon sensors in the inner regions (MightyPix), where the hit density is the highest. Figure 26 shows the studies for the SciFi at increased luminosities for the present tracker and the proposed Mighty Tracker.

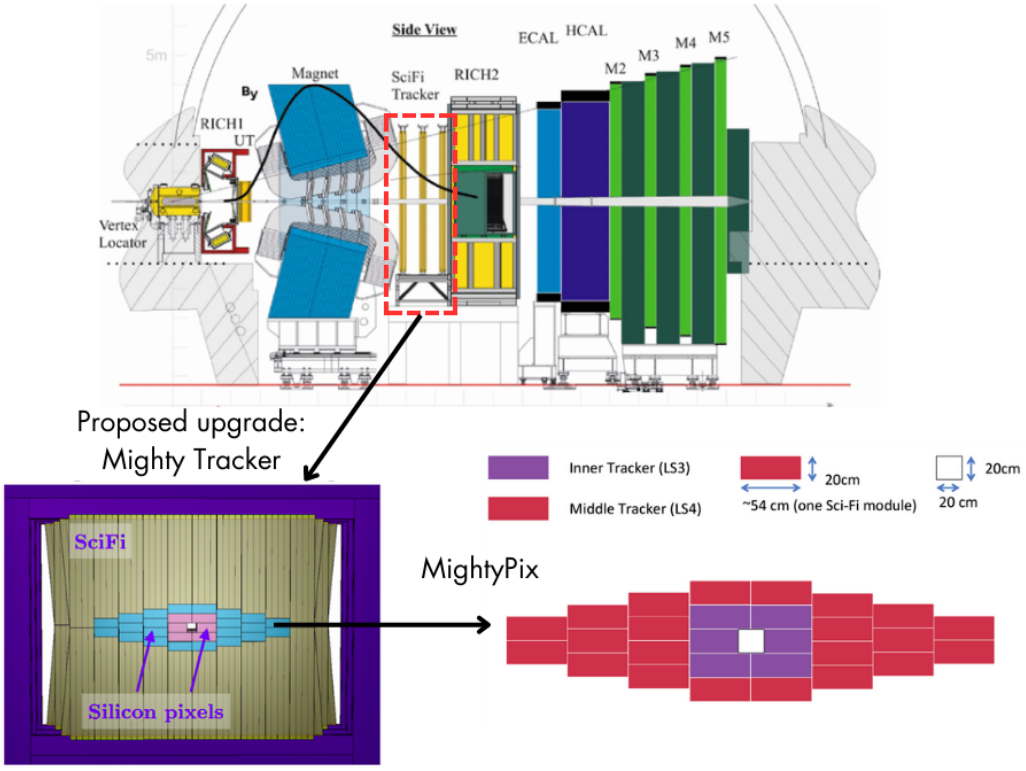

Figure 25.: Cross section of the LHCb detector. The SciFi tracker is highlighted in red. The proposed Mighty Tracker consists of scintillating fibers in the outer regions and Si sensors in the inner and medium regions.

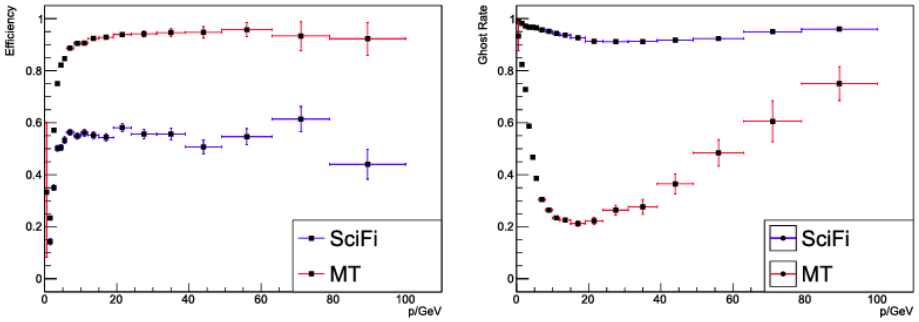

Figure 26.: Simulated reconstruction efficiency (left) and ghost rate (right) as a function of momentum for a $1.5 \times 10^{34}\text{cm}^{-2}\text{s}^{-1}$ luminosity. SciFi (blue) denotes the geometry of the present scintillating fibre tracker, while MT(red) represents the geometry of the Mighty Tracker. [49]

The challenge associated with this application is the need to operate the detector in a high-radiation environment, which leads to radiation damage and increased noise. To overcome this challenge, the proposed baseline technology for the silicon sensors is High-Voltage CMOS detectors (HV-MAPS), which meet the requirements for radiation hardness [39] (radiation tolerance of $6\text{x}10^{14}$ $\text{n}_{eq}\text{cm}^{-2}$) and granularity [7]. Another challenge of the LHCb Mighty Tracker is the required value for the time resolution of ∼3 ns for a relatively large pixel size of 100 x 300 μm^2.

Panda

PANDA (AntiProton Annihilation at Darmstadt) experiment [50] is a particle physics experiment that aims to study various topics around the weak and strong forces, exotic states of matter, and the structure of hadrons. PANDA will be one of the key detectors at the Facility for Antiproton and Ion Research (FAIR) [51] currently under construction in the area of the GSI Helmholtzzentrum für Schwerionenforschung in Darmstadt, Germany. The central part of FAIR is a synchrotron complex providing intense pulsed ion beams.

Antiprotons produced by a primary proton beam will be filled into the High Energy Storage Ring (HESR) [52]. In the HESR, the antiprotons are accelerated or decelerated in a momentum range of 1.5 GeV/c to 15 GeV/c [53]. The antiproton beam hits a fixed proton target inside the PANDA detector and undergoes annihilation and scattering processes. A versatile detector, able to provide precise trajectory

[7] It refers to the size or dimensions of individual detector cells, within the sensor array. A sensor with high granularity has smaller sensing elements, allowing it to capture fine details or variations in the measured quantity.

reconstruction, energy and momentum measurements, and very efficient identification of charged particles, will be built to gather all the necessary information from the collisions.

A variety of items of the PANDA physics program require a luminosity measurement [54]. To determine the time-dependent luminosity, the elastically scattered antiproton tracks must be measured precisely regarding the scattering angle [53]. Therefore, a tracking detector was developed, which allows the reconstruction of the antiproton tracks with high precision. The luminosity detector requires sensors with good spatial resolution, good energy resolution [8], and high rate capability. In addition, the sensors need to have a low material budget to minimize multiple scattering and should be able to operate under vacuum conditions with low power consumption. These requirements led to choosing HV-MAPS as the preferred detector technology.

PANDA experiment sets high demands on the track reconstruction resolution and energy resolution for good particle identification at very high reaction rates of up to 20 MHz. One of the challenges associated with this application is that most of the HV-MAPS prototypes were designed to deliver a fast response rather than a good energy resolution. New engineering runs incorporate designs with two comparators, one fast for good time resolution and one slow for good energy resolution, making it possible to employ HV-MAPS for luminosity measurement of the PANDAS experiment.

TelePix

At the DESY II Test Beam facility [55], users can study the response of novel detectors to particles with an electron beam. MAPS-based telescopes (MIMOSA-26 sensors [56]) are provided in each beam area. MAPS provides good position resolution, but as most of the charge is collected via diffusion, they do not offer the best time resolution. In the case of the MIMOSA detector, the rolling shutter architecture further limits the time resolution to $\sim$230 µs. Since the demand for better timing is becoming more relevant, DESY foresees several upgrades of the telescopes. TelePix [57] is an upgrade project to provide track time stamping with a precision greater than five ns. Small-scale prototypes have been characterized, showing efficiencies above 99% over a threshold range of more than 100 mV and time resolutions of 3.16 ns at low noise rates [57].

One of the challenges for this application is the pixel size. The current TelePix pro-

[8] Energy resolution refers to the ability of the detector to accurately differentiate and measure the energies of incident particles, providing a quantifiable measure of the detector's ability to distinguish between different energy levels.

totype uses a pixel size of 25x165 µm^2. Smaller pixel sizes would further improve the time resolution due to the direct proportionality with the pixel area, but the sensor scaling presents diverse difficulties. Reducing the pixel size increases the total number of pixels within the sensor and, thus, the number of connection lines to the digital part sitting in the periphery. The increased number of lines and the subsequently reduced distance between them result in increased crosstalk and fake hits. Additionally, the area of the pixel needed for the in-pixel electronic will be limited. As for the device functionality, high electric fields are likely to occur in the inter-pixel region, increasing the capacitance due to a reduced maximum operating voltage and depletion depth.

In conclusion, HV-MAPS offers many unique advantages for particle physics experiments, including high sensitivity, fast response times, and radiation hardness. However, several challenges must be addressed for specific applications requiring further research and development (R&D) to improve their performance. The latter constitutes the main motivation of this thesis.

3.2.2. HV-MAPS Prototypes

Starting in 2007, when the HV-MAPS concept was published, the R&D for implementing this sensor for the Mu3e pixel tracker started. Several prototypes denoted MuPix sensors have been created for phase I of the Mu3e experiment, from the small-scale MuPix1 prototype to today's MuPix11. On the road, other sensors based on a similar concept but with different specifications have been studied, like the ATLASPix [39], TelePix [57], and the MightyPix [49]. Additionally, other general characteristics of the HV-MAPS sensors as pixel size, amplifiers, and comparators, are under study as part of two engineering runs.

As part of an R&D cycle, sensors must be designed, manufactured, commissioned, characterized (in the laboratory and under an accelerator beam), evaluated, and optimized. This thesis presents the results of the optimization and characterization of three HV-MAPS prototypes. Results from the MuPix10 characterization under an accelerator beam are presented in Chapter 7. Accordingly, the MuPix10 sensor is introduced in detail in this chapter. The findings using TCAD simulation in the ATLASPix, MuPix8, and MuPix10 structures are shown in Chapter 5. These prototypes have a different readout scheme and pixel design than the MuPix10. Therefore, the unique characteristics of these sensors are also presented in this chapter. The testebam characterization of the MuPix8 and ATLASPix sensors is not a subject of this thesis and can be found in [58] and [59], respectively.

MuPix10

MuPix10 is produced in a 7 aluminum metal layer process with a minimum gate length of 180 nm provided by TSI [60] semiconductors. Unlike previous prototypes designed to solve the technology challenges of the HV-MAPS, the MuPix10 design goal is to provide a full-scale chip that fulfills all the requirements for the Mu3e pixel tracker.

The chip layout from Figure 27 shows the active pixel matrix and the periphery, which occupies a total area of 20.66 x 23.14 mm^2. The sensors have been produced on wafers with different substrate resistivities and thicknesses. The pixel matrix (256 x 250 pixels each with an 80 x 80 μm^2 pitch) is subdivided into submatrixes, and each readout by an individual data link. The periphery makes up 13% of the total chip surface, of which 2.2% correspond to the bond layout. The periphery also houses the digital-to-analog converters (DAC) and the clocked circuitry to digitize and read out the pixel hits. The sensor architecture is sketched in Figure 28.

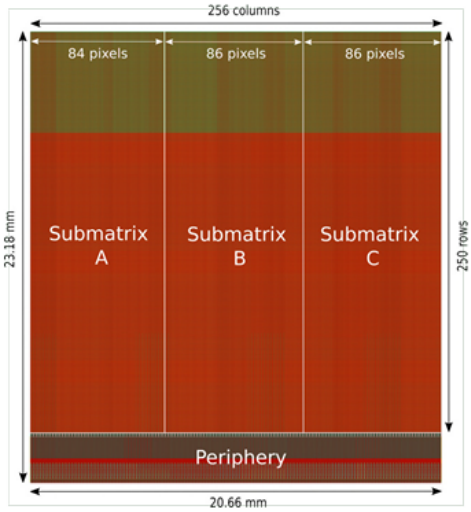

Figure 27.: MuPix10 chip layout highlighting the pixel matrix and the periphery. Each submatrix is readout by an individual data link.

The active pixel comprises the sensor diode (n-well and the p-doped substrate). The n-well houses the charge-sensitive amplifier (CSA) and a source follower (SF). The SF drives the analog signal to the readout cell in the periphery. The analog pulse arriving at the readout cell is AC coupled to a system of two comparators with individual thresholds.

The comparators can be used individually or can share tasks. The common threshold for each comparator is set globally. Individual 3-bit digital-to-analog

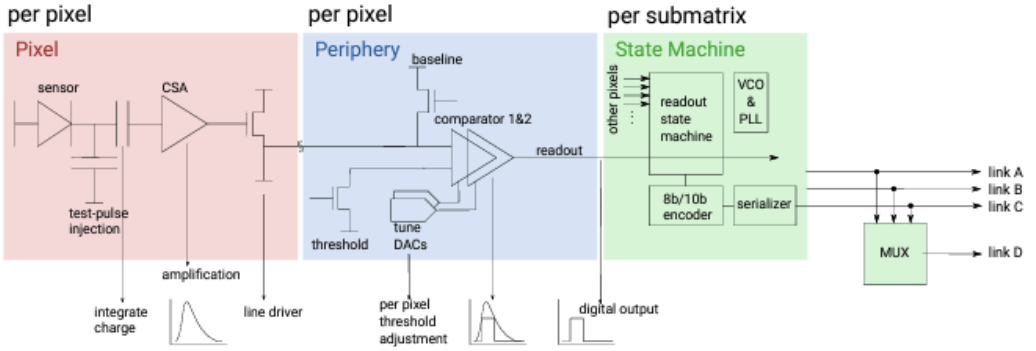

Figure 28.: Schematic drawing of the signal chain of the MuPix10 sensor, including the in-pixel electronics and the digital periphery.

converters (DAC) allow for fine-tuning each pixel threshold. This feature can ensure a uniform signal response or noise suppression over the pixel matrix [61]. A fourth enable bit can be used to mask out noisy pixels. Additionally, the comparator flags the hits and measures the time-of-arrival (ToA) when the signal of the rising edge crosses the threshold (see Figure 29). The measured timestamp is 11 bits wide with an 8 ns binning.

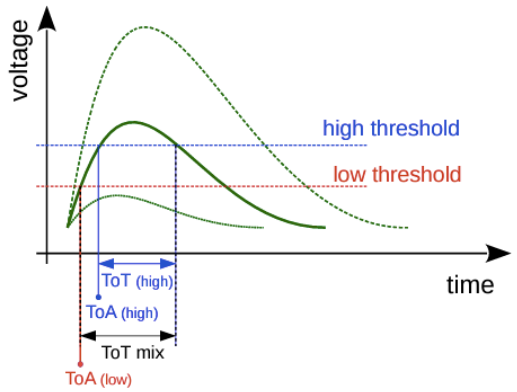

Figure 29.: Two-comparator threshold methods as implemented in MuPix10. In the mixed mode, the ToA is determined by the low threshold and time-of-fall by the high threshold.

When the pulse drops below the threshold, a second 5-bit timestamp (TS2) is stored typically with 128 ns binning to cover a pulse duration range of 4 μs. The subtraction of the timestamps allows calculating the time-over-threshold (ToT), which is a 5 bits measure of the deposited energy.

In Figure 29, it is visible that the stored ToA depends on the pulse height, and long pulses result in lower ToA. This effect is referred to as timewalk. The impact of timewalk can be reduced by lowering the threshold or measuring the ToT and correcting this effect in the offline analysis. Lowering the threshold can lead to an increase in noise-induced hits. To address this, the second comparator was implemented, allowing samples of the ToA on a lower threshold with little timewalk, while the other comparator, on a higher threshold (well above the noise), generates the hit flag. It is possible to use only one comparator or a mixed mode where the ToA is defined by the lower threshold and the time-of-fall by the higher threshold.

The sampling of the second timestamp is affected if the hit is read out before TS2 is sampled (Figure 30a). The scheme pictured in Figure 30b is implemented for a correct ToT measurement and subsequently enables the possibility of timewalk corrections. When the comparator sets the hit flag, a delay period starts. If the delay is correctly chosen, TS2 will be properly sampled even for hits with large ToT. As the delay is the same for all pixels, the time ordering of the readout hits remains unchanged.

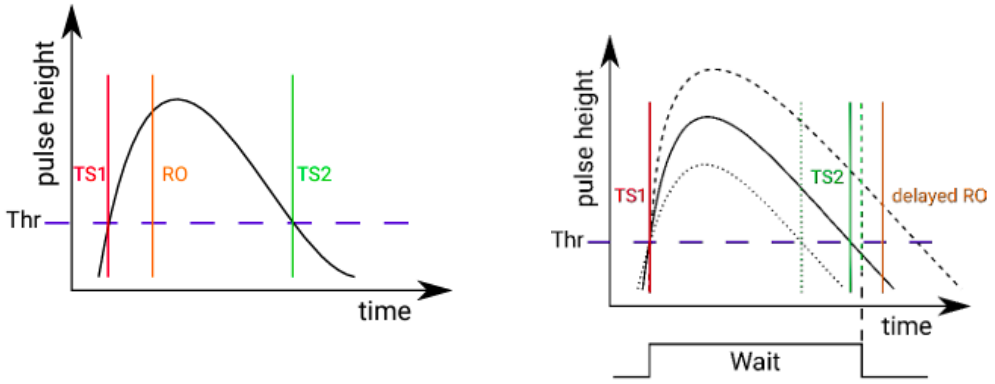

(a) Timestamp sampling without delay.

(b) Sampling with delay after hit flagging.

Figure 30.: Readout time (RO) and timestamp sampling for different pulse lengths using a constant delay. [41]

The registered hits are read out in a column-drain fashion. The data is serialized by the on-chip state machine [41] and sent out via 1.25 Gbit/s links. To test single chips, the sensors are mounted onto a specifically designed Printed Circuit Board (PCB), which was developed to supply all necessary voltages, currents, clocks, and other signals and are configured and read out via the DAQ system presented in [62]. The MuPix10 chip can be connected to the PCB via an edge connector and a daughter PCB called “insert” on which the chip is glued and bonded, as depicted in Figure 31.

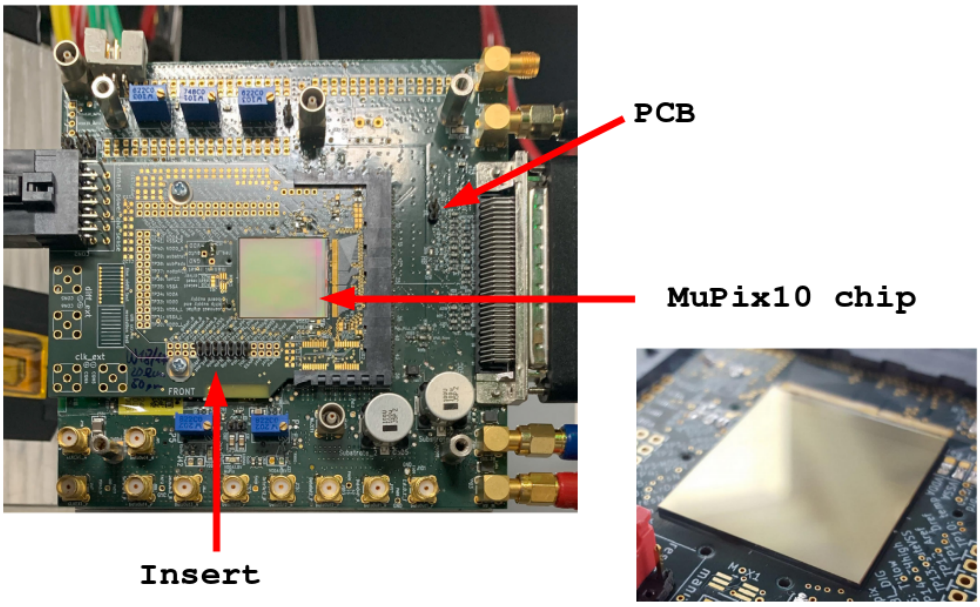

Figure 31.: MuPix10 chip mounted on the insert and PCB.

MuPix8

The MuPix8 [58] sensor, which preceded the MuPix10, was the first large-scale sensor developed for the Mu3e experiment (sensor size of 10.7x19.5 mm^2). Unlike MuPix10, MuPix8 was produced in the AH18 process by ams AG [63]. The primary objective of the MuPix8 prototype was to investigate various aspects such as sensor size, power network, and potential cross-talk issues associated with the long analog readout lines. The sensor and in-pixel layout are shown in Figure 32. Table 2 compares the design parameters of MuPix8 and MuPix10. The most notable change is the chip size.

Table 2.: MuPix8 and MuPix10 sensor specifications.

	MuPi8	MuPix10
Pixel size [µm^2]	81x80	80x80
Sensor size [mm^2]	10.7x19.5	20.66x23.18
Active area [mm^2]	10.3x16.0	20.48x20.00
Sensor thickness [µm]	53, 100	50, 60, 70, 80, 100
Substrate resistivity[9] [Ω cm]	≈20, 80, 200	≈20, 200

[9]The given resistivities are only approximate and are specified in the ranges 10–20 Ω cm (20), 50–100 Ω cm (80) and 200–400 Ω cm (200).

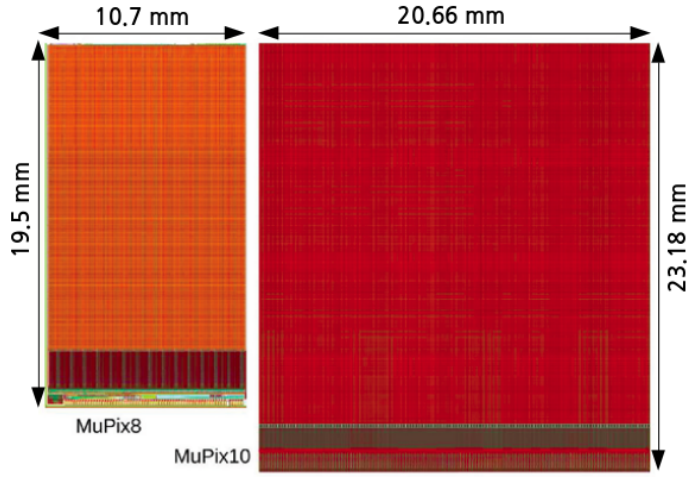

Figure 32.: Sensor size comparison of MuPix8 and MuPix10 prototypes. The main area is the active pixel matrix, and the stripe at the bottom is the periphery.

ATLASPix

In addition to the Mu3e experiment, HV-MAPS technology has been extensively studied for its potential implementation in other experiments. An example of such an application is the ATLASPix, which was proposed and designed as an option for the outer layer of the Inner Tracker Pixel detector of the ATLAS (an acronym for A Toroidal LHC ApparatuS) tracking system upgrade [64]. The architecture of the ATLASPix sensors differs from that of the MuPix sensors as it incorporates an in-pixel comparator, as depicted in Figure 33. The digital nature of the pixel pulse transmission offers advantages over the analog approach used in the MuPix sensors since the adjustability of the normalized pulse height enables complete crosstalk suppression without compromising efficiency.

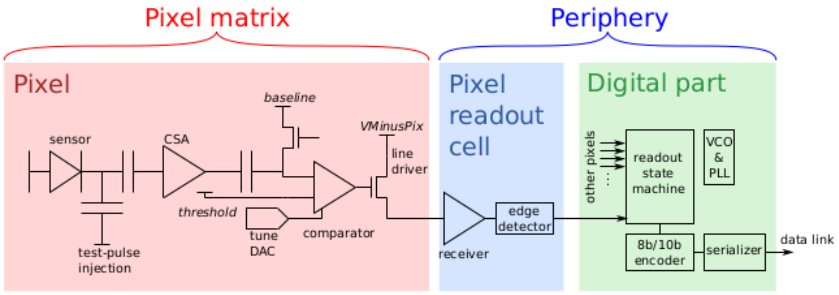

Figure 33.: ATLASPix signal chain schematic, including the in-pixel electronics and the digital periphery.

Several ATLASPix prototypes have been designed in AMS/TSI 180 nm process to meet the ATLAS Inner Tracker detector requirements. The first-generation ATLASPix1 [10] [59] (pixel size: 130 × 40 µm^2) has proven high radiation tolerance and detection efficiency in testbeam studies [39]. ATLASPix2 [65] (pixel size: 110 × 45 µm^2) chronologically introduced the sorting of hits. ATLASPix3 [66] (pixel size: 150 × 50 µm^2) is the first full reticle size, with a pixel size of 2x2 cm^2. It adopts some of the design blocks from its predecessors while ensuring compatibility with RD53A readout and configuration protocol [67].

Furthermore, ATLASPix_IsoSimple [39], one of the ATLASPix1 prototypes, introduces a deep p-well, as sketched in Figure 34b. The deep p-well facilitates the complete decoupling of the PMOS (p-type metal-oxide-semiconductor) transistors from the n-well, thereby enabling the integration of digital CMOS electronics within the active detection area without a possible parasitic coupling into the signal collection electrode. The utilization of CMOS electronics within the pixel allows for implementing of complex in-pixel electronics, offering the possibility of relocating circuits from the periphery into the pixel itself. This approach reduces the size of the periphery and the non-active detection surface area.

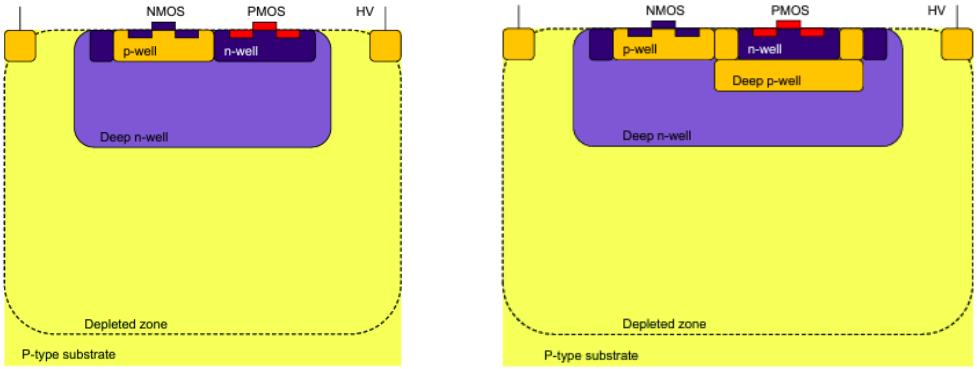

(a) Shallow p-well: ATLASPix_Simple. [59] **(b)** Deep p-well: ATLASPix_IsoSimple. [39]

Figure 34.: Cross-section of floating logic for ATLASPix prototypes. [68]

[10] Note that for the ATLASPix1 chip, three different prototypes were included in the same reticle (ATLASPIx_Simple, ATLASPIx_IsoSimple and ATLASPIx_M2). Each with a different pixel size and active area. Additionally, differences in the on-chip electronic are implemented. Due to a different signal line routing, the pixel size for ATLASPIx_M2 is reduced to 60 × 50 µm^2

Part II.

TCAD Simulation of HV-MAPS

Chapter 4

TCAD Simulation Tools

In recent years, the field of detector development has undergone significant advancements, driven by the increasing demand for high-performance detectors in a wide range of applications, such as medical imaging, radiation detection, and high-energy physics experiments. The performance of these detectors is crucial for many applications, and optimizing their performance requires a deep understanding of their physical operation.

TCAD, which stands for Technology Computer-Aided Design, uses numerical modeling techniques to develop and optimize semiconductor technology processes and devices. Some of the first TCAD tools were developed in the 1980s at Stanford University [69]. TCAD tools numerically solve the five classical semiconductor device equations (Poisson's electrostatic potential, electron and hole continuity, and electron and hole drift-diffusion current equation). These tools typically operate at the device level using fundamental physical models and usually only incorporate basic external circuit elements. In contrast, "mixed-mode" simulators incorporate more comprehensive models for external circuit elements. These advanced tools integrate TCAD (Technology Computer-Aided Design) with SPICE [70] (Simulation Program with Integrated Circuit Emphasis) models, enabling a more holistic simulation approach.

TCAD simulations can be used to study the transport of charge carriers within a detector. Another advantage of TCAD simulations is the possibility to explore and understand a wide range of design options quickly and efficiently. Instead of building and testing multiple prototypes, it is possible to simulate different detector designs and evaluate their performance under varying operating conditions.

TCAD simulations can also be used to study the effects of radiation damage on

semiconductor detectors. Radiation damage degrades the performance of detectors over time, leading to reduced efficiency and increased noise. By simulating the effects of radiation on detector materials, it is possible to develop more robust detectors that can withstand high levels of radiation exposure.

4.1. TCAD tools

A modern TCAD software package includes several simulation tools like the process simulator, the device simulator, the Graphical User Interface (GUI), and visualizations tools. This thesis uses 2D and 3D device simulation software developed by Synopsys [5]. Relevant device physics, such as doping concentration effects and electric field-dependent mobilities, are incorporated into the program.

4.1.1. Sentaurus Structure Editor

In Sentaurus Structure Editor (SDE) [71], 2D and 3D structures using geometric models can be generated or edited using the GUI or batch mode (scripts based on Scheme [72] scripting language). In addition, doping profiles (constant, analytic, or external) and contacts are defined. Figure 35 shows an example of a 2D and 3D pixel geometry generated with SDE. Additionally, it generates the necessary input files for the meshing and device simulation.

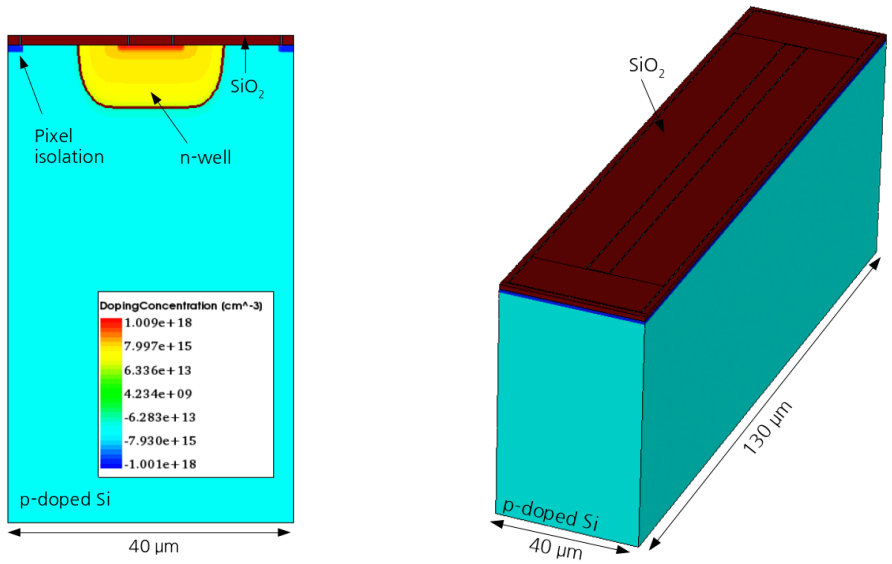

(a) 2D. **(b)** 3D.

Figure 35.: 20 Ω cm ATLASPix pixel-geometry reconstruction using SDE.

4.1.2. Mesh Generator

TCAD simulates the electrical parameters using the finite element method (FEM) [73]. The FEM is widely used to solve differential equations for complex device geometries numerically. It accomplishes this by discretizing the continuum description of semiconductor device equations into a simulation model composed of a finite number of points. This transformation allows the problem to be represented as a linear system of equations, which can be efficiently solved using linear algebra methods. By applying FEM, complex device behaviors can be accurately analyzed and understood through the systematic approximation of their mathematical representations. The global solution is then obtained by combining the solutions for the many elements.

To obtain the solutions in an arbitrary geometry, we must subdivide the surface or volume into rectangular, triangular, prismatic, or pyramidal sub-elements small enough that the solution is locally polynomial in this domain and can be approximated by a polynomial. The sum of all sub-elements covering the simulation geometry is called the mesh. One of the key components of the Synopsis TCAD is the Sentaurus Mesh Generator (SNMESH) [74], a powerful tool that enables the generation of high-quality meshes.

A mesh example for a 2D ATLASPix simulation can be seen in Figure 36. To obtain a good approximation of the solution using the FEM, the mesh element's size must be chosen to be sufficiently small. Regions, where the solution is expected to vary rapidly, require a smaller mesh size to ensure that the solution can be represented as a local polynomial function. TCAD software use known quantities in the geometry, such as impurity concentration, to generate the mesh sub-elements covering the domain to simulate.

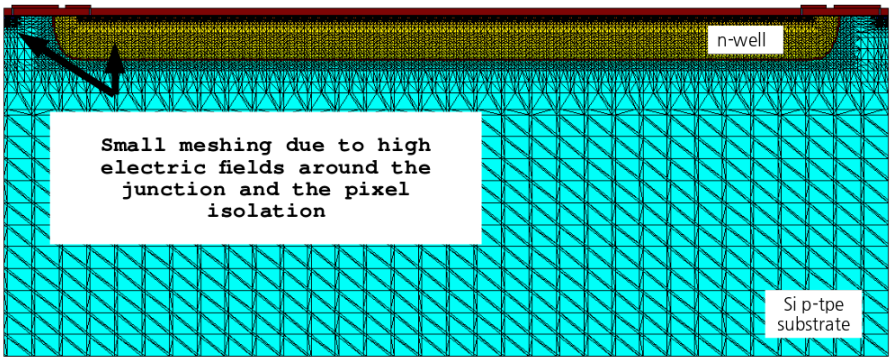

Figure 36.: Meshing example in the ATLASPix pixel-geometry using SNMESH.

SNMESH is a highly versatile tool that can handle a wide range of geometries, including complex 3D structures and layered materials. The mesh generator also offers automatic mesh refinement, which helps ensure the mesh is optimized for accuracy and efficiency. However, no method exists to determine the perfect mesh. A case-by-case study must be performed to ensure the validity of the solution obtained. This is essential for accurate simulations, as small errors in the mesh can lead to significant inaccuracies in the simulation results.

4.1.3. Sentaurus Device Simulators

Sentaurus Device simulation (SDEVICE) [75] simulates electronic devices' electrical and optical behavior. The selection of physical models is a very important step in getting realistic results from the device simulator. Examples of these models include mobility models, carrier transport mechanisms, velocity saturation, carrier generation, and recombination. Some of the models need extra refinements of the grid at critical positions. Appendix B lists the physics section of the SDEVICE input file used for the simulation results presented in this thesis.

Transient simulations

Transient simulations are used to analyze the behavior of a device over time. These simulations are particularly useful for understanding how a device responds to changes in its environment, such as when a particle interacts with the detector and can be used to identify potential design issues or performance limitations.

Figure 37 shows the transient simulation example of the integrated charge collected during 15 ns by a MuPi8-like pixel in a 80 Ω cm substrate resistivity with a 40 µm thickness and a bias voltage of -60 V when a MIP passes through different in-pixel positions. Determining the charge collected at different positions can help predict inefficiencies within the pixel matrix.

Quasi-stationary simulations

With SDEVICE, it is also possible to perform quasi-stationary simulations. These are used to study the steady-state behavior of a device. Quasi-stationary simulations are useful for analyzing the performance of a device over a range of operational conditions and identifying potential design optimizations.

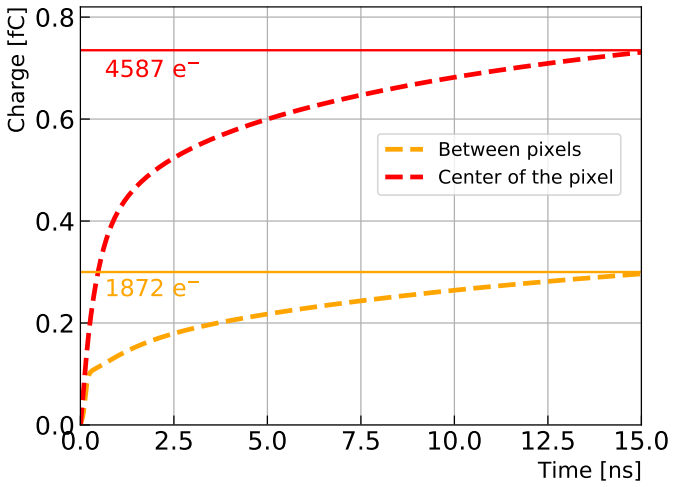

Figure 37.: Transient simulation results of the charge collected during 15 ns by a MuPi8-like pixel in a 80 Ω cm substrate resistivity with a 40 µm thickness and a bias voltage of -60 V when a MIP (with equivalent energy transfer of 112 e-h/µm) passes through different in-pixel positions.

Figure 38 shows an example of the electric field distribution and depletion zone in an HV-MAPS prototype obtained using quasi-stationary simulations. The depletion depth is a distinct characteristic of silicon detectors and is widely studied using TCAD simulations.

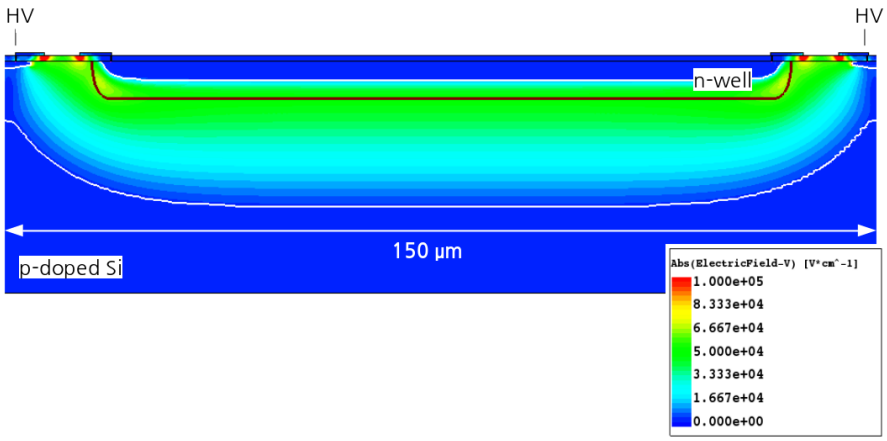

Figure 38.: Quasi-stationary simulations of the Electric Field distribution and depletion zone in an ATLASPix3-like pixel in a 80 Ω cm substrate resistivity with a 40 µm thickness and a bias voltage of -60 V. The white line inside the n-well and the p-doped substrate defines the depletion depth edges.

Additionally, Figure 39 shows the electrostatic potential distribution at the junction between the n-well and the pixel isolation for different mask[1] lengths. The simulation results show that a short distance between the isolation and the n-well (defined by the mask) produces an abrupt change in the electrostatic potential. This sudden change can result in high electric fields that create large leakage currents due to avalanche multiplication, bringing the sensor into the breakdown. These results can be used to optimize the pixel design dimensions.

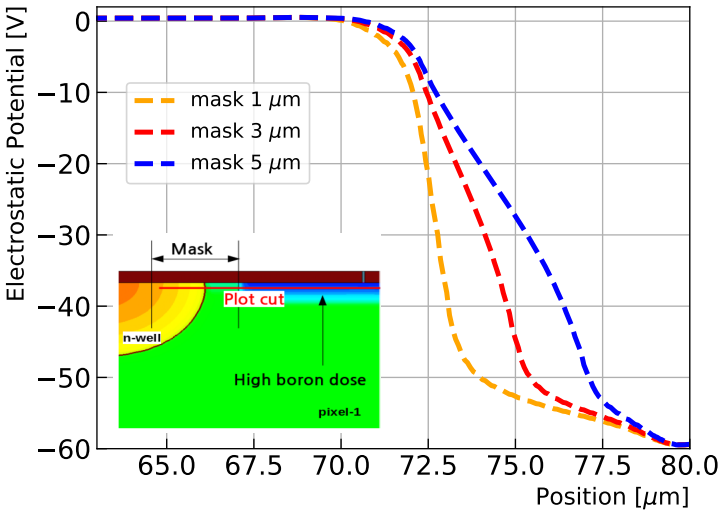

Figure 39.: Quasi-stationary simulations of the electrostatic potential along a parallel line to the sensor surface, from inside the n-well to the edge of the pixel, for different masks in a MuPix8-like pixel structure in a 80 Ω cm substrate resistivity with a 40 µm thickness and a -60 V bias voltage.

Finally, Figure 40 shows the result of a mixed-mode quasi-stationary simulation, used to compute the junction capacitance[2] as a function of the applied voltage for different pixel sizes and substrate resistivity in a generic HV-MAPS with 20 µm thickness. The junction capacitance is essential as it directly impacts the signal-to-noise ratio and overall detector performance.

The results were computed as $1/C_j^2$ since it shows a linear behavior as a function of the voltage up to the full depletion (Equation 26). After full depletion, the $1/C_j^2$ behavior with the voltage is constant since the depletion region cannot extend beyond the thickness of the sensor. The simulation results show that while the 1000 Ω cm

[1] Mask is an area around the n-well which is excluded from a high boron concentration, used for pixel isolation. More details are in Chapter 5

[2] By default, a device simulated in 2D is assumed to have a "thickness" in the third dimension of 1 µm. As a result, the capacitance results are given in C µm^{-1} for 2D, and C for 3D devices.

substrate reaches full depletion at ∼10 V, the 20 Ω cm does not reach full depletion inside the studied voltage range. The curve shows the expected behavior where higher substrate resistivity has lower capacitance due to the larger depletion. Meanwhile, a large pixel size results in a capacitance increase. This result helps estimate the junction capacitance for different layout designs and optimize for possible operating voltages and wafer resistivities.

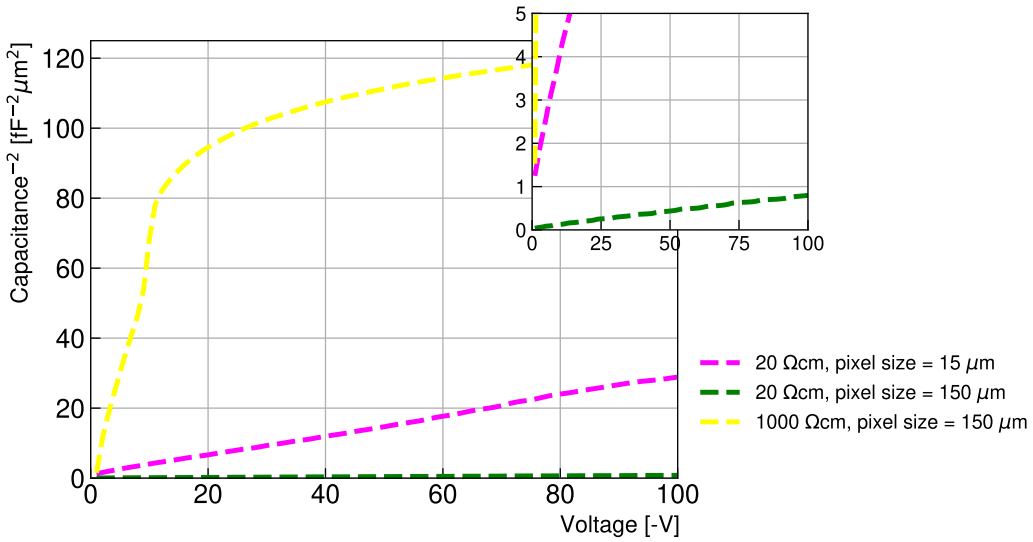

Figure 40.: Junction capacitance as a function of voltage for different pixel sizes and substrate resistivity in a generic HV-MAPS with 20 µm thickness.

Chapter 5

TCAD Simulation of HV-MAPS

HV-MAPS operation is intricately tied to their design, making optimizing the pixel layout critical to achieving the desired performance levels. In this regard, TCAD simulations have emerged as an indispensable tool. TCAD facilitates the exploration of diverse design options, enabling the identification of optimal parameters that maximize the sensor's performance according to specific experimental requirements. Taking advantage of TCAD simulations, it is possible to effectively predict and analyze essential electrical characteristics of the HV-MAPS devices, including the electric field distribution, charge collection efficiency, and noise performance.

This chapter comprehensively analyzes the results obtained from TCAD simulations of HV-MAPS prototypes. The study examines the effects of various design parameters, such as pixel size, doping concentration, thickness, and biasing voltage, on the sensor's overall performance. To ensure the credibility of the findings, a qualitative analysis is performed by comparing selected simulation results with experimental data, thus validating the accuracy and reliability of the proposed TCAD model.

5.1. PN-junction

In Chapter 2, pn-junctions were introduced as the building blocks of silicon detectors. To study the behavior of HV-MAPS using TCAD Simulations, a pn-junction was created as the initial step in the simulation process. It is crucial to note that:

- Boron-doped Si substrate (p-substrate) with a highly doped n-well as the collection electrode was used in the simulations. This configuration was kept through all the simulations and the HV-MAPS prototypes.
- This configuration is more effective for particle detection than using an n-type

substrate because the charge collected for the segmented electrodes are the electrons, which have higher mobility than holes, making them more efficient in the charge collection process.

To simulate a basic pn-junction using SDE (Subsection 4.1.1), the following steps were used:

1. Definition of the physical structure of the pixel, including the dimensions and materials. The dimensions of the pn-junction may vary between different prototypes.

2. Specification of the doping profiles and concentrations.
   - For the p-substrate, a uniform concentration is used, which variate between different prototypes.
   - Since the doping profiles are a company secret, the n-well doping concentration has to be estimated. The n-well doping concentration was reverse-engineered and calculated for an HV-MAPS prototype in a 10 $\Omega\,$cm wafer in [76]. Based on the reported results, a value of 6.5×10^{15} cm^{-3} was set as the n-well phosphorus concentration in this thesis.
   - The n-well profiles were reproduced assuming that they were created using diffusion (see Section 2.2). Diffusion is preferred over ion implantation for deep n-well since diffusion can create a more uniform doping profile with a smoother transition between the doped and undoped regions. This is particularly important since any variations in doping concentration can lead to non-uniformities in the detector response and affect its performance. In addition, diffusion allows for creating much deeper wells than ion implantation.
   - With this assumption, a Gaussian function was used to reproduce the dopant distribution in the n-well. The Gaussian distribution function is suitable for modeling the dopant distribution in an n-well region because it has a maximum at the center of the distribution, which corresponds to the highest dopant concentration, and decreases gradually towards the edges of the region. This accurately models the behavior of the dopants in the n-well region, which gradually decrease towards the edges due to diffusion. In addition, the Gaussian function has well-defined parameters, such as the mean and standard deviation, which can be used to control the shape and size of the distribution.

- As seen in Section 2.2, the doping process also creates lateral diffusion, extending to around 75%–80% of the vertical diffusion depth. The error function was chosen as the suitable function for modeling the lateral dopant distribution in the n-well region because the error function parameter can be used to control the shape and size of the distribution.

Figure 41 shows the simulated doping concentration distribution of a generic HV-MAPS pn-junction in a 20 Ω cm substrate. The n-well is visible and was created following the previously explained steps using a maximum concentration of 6.5×10^{15} cm^{-3}.

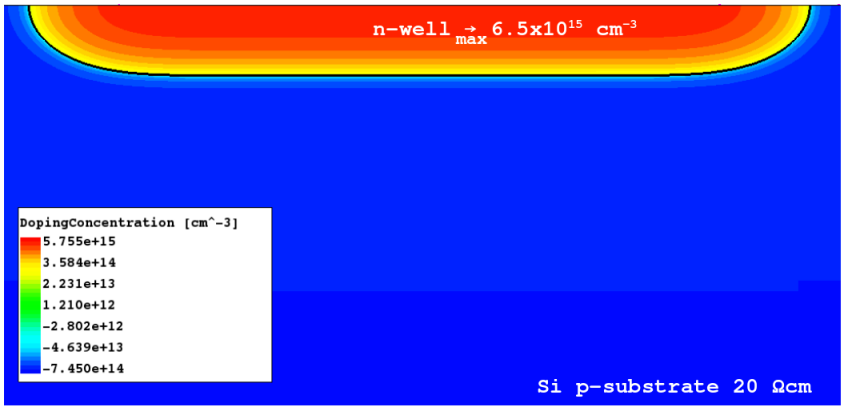

Figure 41.: Generic HV-MAPS pn-junction in a 20 Ω cm substrate. The black line represents the junction line. The n-well is defined as a Gaussian function with a maximum concentration of 6.5×10^{15} cm^{-3}. For lateral diffusion, the error function is used.

5.1.1. Biasing Structure

In Section 2.2, two critical steps in the sensor manufacturing process, oxidation, and metallization, are introduced. Both of these steps are essential in the sensor performance and are accordingly included in the simulations. For oxidation, a layer of SiO_2 is created in the frontside face of all simulated structures. An etching step was also included in the contact areas, where Al metallization was used. The contact points vary depending on the specific prototype being simulated. HV-MAPS utilized a multi-metal layer structure consisting of 6 metal layers for ams and 7 for TSI technology. The metal layers serve not only for readout but also for biasing the sensor. Frontside biasing offers greater design flexibility than backside metallization as it enables the creation of complex, multi-functional devices with different regions

of the device biased independently. This is particularly important in applications where multiple device regions require different biasing for optimal performance. In addition, utilizing the pre-existing multilayers for biasing eliminates the need for creating an additional aluminum layer in the backside, reducing fabrication steps, material, and radiation length.

The simulation structure presented in this thesis includes the contacts and oxide structure, which are illustrated and highlighted in Figure 42 for a generic HV-MAPS.

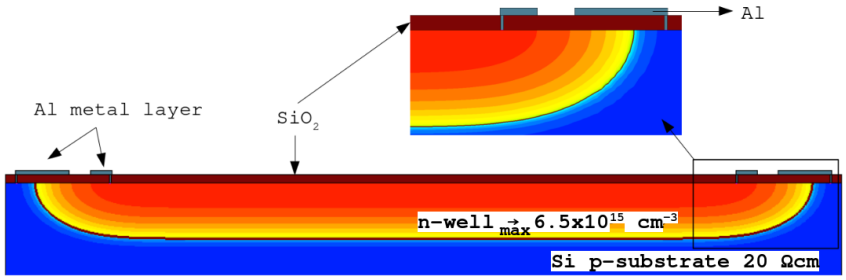

Figure 42.: Generic HV-MAPS pixel layout in a 20 Ω cm substrate with oxidation and metallization structures included using SDE simulation.

After creating the contacts, oxide, and pn-junction, the SDE simulation output was fed into the SDEVICE (see Section 4.1.3) tool to investigate the electrical behavior of various designs. The SDEVICE simulation involves two essential steps: defining the physical models (presented in Appendix B) and biasing the electrodes.

5.2. Depletion zone

The pn-junction is operated under reverse bias, causing the depletion region to widen. The n-well is designed so that the depletion zone matches the pixel's shape, ensuring that the entire sensor active matrix is sensitive to irradiation. As a charged particle passes through, it generates electron-hole pairs, which are separated by the electric field in the depletion region and collected by the electrodes.

The depletion zone is a distinctive characteristic of HV-MAPS sensors, and this section studies its behavior under different operation conditions to ensure a full depletion coverage over the whole sensor active matrix. The depletion zone width is defined as the distance between the edges of the p- and n-regions depleted of free charge carriers. The edges are determined by the concentration of dopants in the semiconductor material and applied voltage.

In a typical pn-junction (abrupt "infinite" [1]), as the one shown in Figure 43, the depletion extends vertically, as shown in Figure 44a. This classic model does not fully describe the real shape of pixel detectors' pn-junction. For a more realistic pn-junction model like the HV-MAPS shown in Figure 41, the depletion extends vertically through the thickness of the detector but also horizontally across the pixel, as shown in Figure 44b.

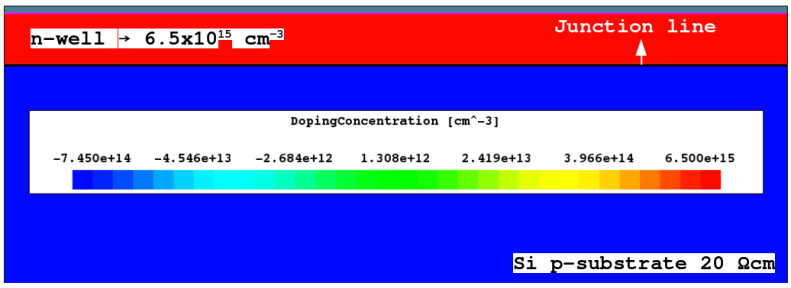

Figure 43.: Doping concentration distribution for an abrupt "infinite" junction. A 20 Ω cm substrate was used.

5.2.1. Voltage dependence

Figure 45a presents the depletion width in the middle of the n-well as a function of the applied voltage for a set of substrate resistivities. The simulation results reveal that the depletion zone width increases as the voltage increases for all substrate resistivities. This is due to the reverse bias effect explained in Section 2.3.2, where the minority charge carriers are injected into each side of the junction, attracting the majority charge carrier, which leaves behind an ionized atom. As the voltage increases, more free charge carriers are attracted, and the depletion zone widens.

5.2.2. Substrate resistivity dependence

The substrate resistivity is an important factor that affects the electrical properties of the pn-junction and the behavior of the depletion region. From Figure 45a, it is clear that the depletion zone increases not only with the increase of the voltage but also with the increase of the resistivity. Figure 45b explores how the depletion zone of HV-MAPS changes in response to the substrate resistivity using TCAD simulation.

[1] Constant doping and n-type and p-type material have the same dimensions.

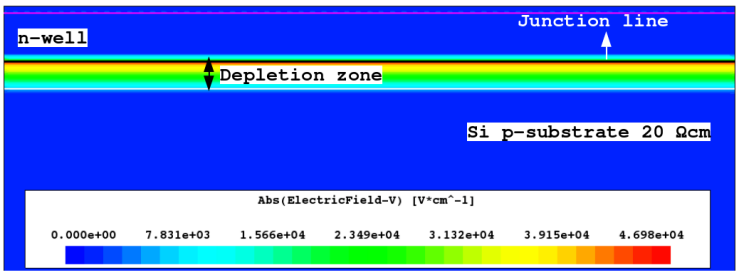

(a) Abrupt "infinite" junction .

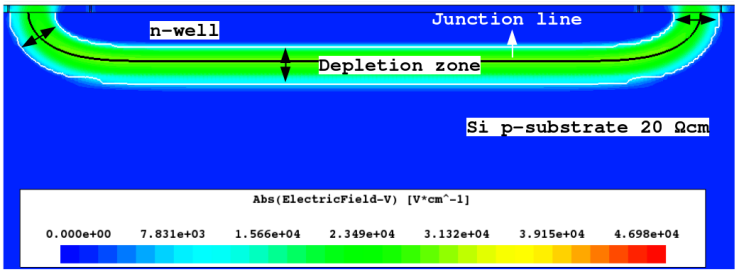

(b) Gaussian gradient junction.

Figure 44.: TCAD SDEVICE electric field distribution in a 20 Ω cm substrate at -20 V. The white lines define the border of the depletion zone.

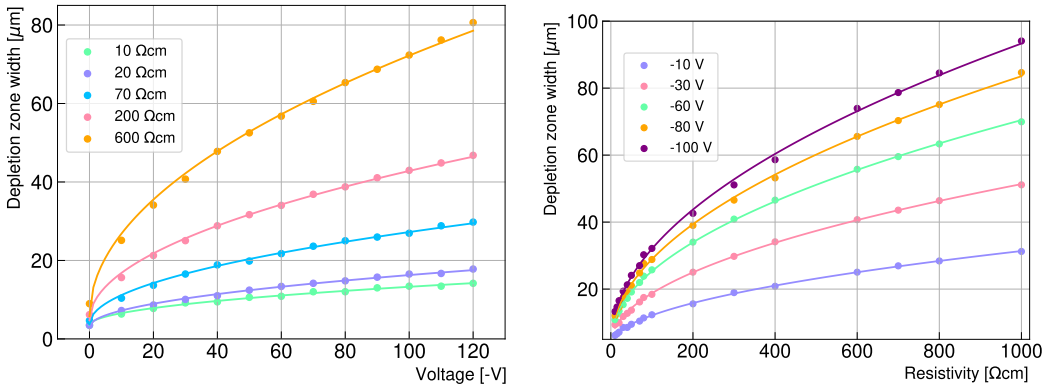

(a) **(b)**

Figure 45.: TCAD simulation vertical depletion width in a generic HV-MAPS as (a) a function of voltage and (b) resistivity.

The depletion zone increases as the substrate resistivity increases [2] because fewer carriers are available to neutralize the charge created by the minority carriers that diffuse across the junction. As a result, the depletion region widens to maintain the

[2]The number of majority-free charge carriers decreases when the doping concentration decreases, inversely proportional to the resistivity

balance between the diffusion and recombination of minority carriers. While the depletion zone increases for high substrate resistivities, the opposite effect occurs over the electric field due to decreased free charge carriers (as seen in equation 11).

Figure 46 shows the electric field distribution and depletion width in the center of the n-well along the sensor thickness for different substrate resistivities in a MuPix8 sensor thinned to 40 µm and a bias voltage of -60 V. A large depletion zone, as is the case for the higher substrate resistivities, can increase the charge collected, but a high electric field, as is the case for the lower substrate resistivities, is ideal for fast-timing applications. Selecting the ideal substrate resistivity is a challenging step in the sensor design. HV-MAPS prototypes have been developed in different substrate resistivities to study its effect on detector performance (Chapter 7).

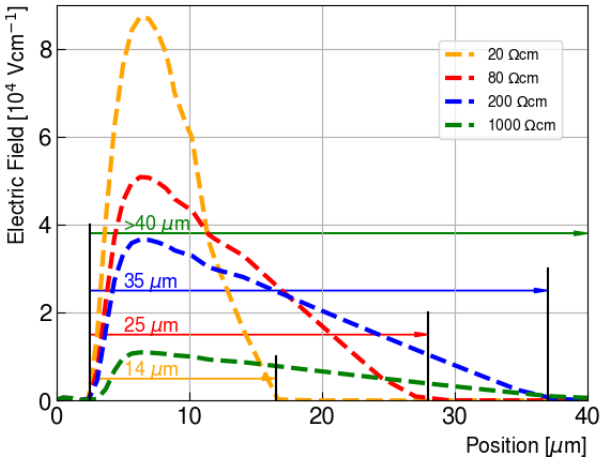

Figure 46.: Electric field and depletion in the center of the n-well along the sensor thickness for different substrate resistivities in a MuPix8 sensor thinned to 40 µm at -60 V.

5.2.3. Biasing

As previously seen, the depletion width depends on the voltage and resistivity. However, the biasing design is another factor that affects the depletion zone. Figure 47 shows the electrostatic potential and depletion zone for different biasing configurations for a generic HV-MAPS with a 200 Ω cm substrate and -40 V external voltage.

Front-side biasing in HV-MAPS is the result of the previously discussed multi-layer structure. For this configuration, the depletion zone (Figure 47a) follows the shape of the n-well and grows as $\sim\sqrt{V}$ until the depletion region reaches the high voltage

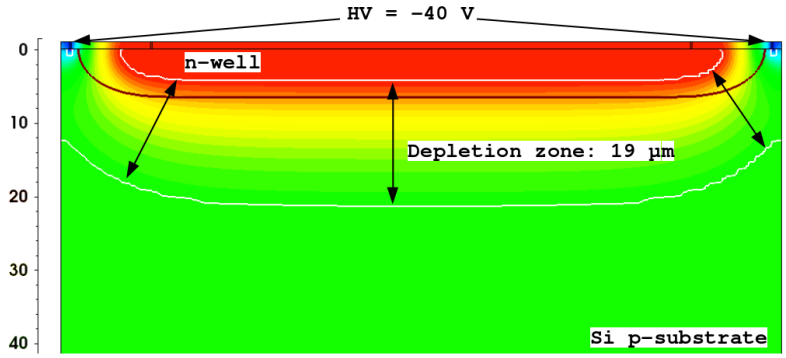

(a) Front-side biasing.

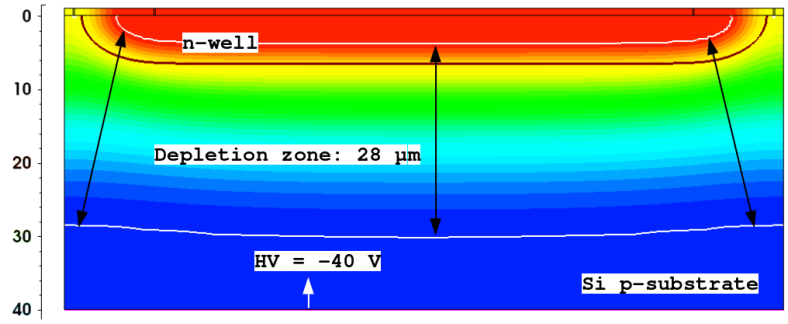

(b) Back-side biasing.

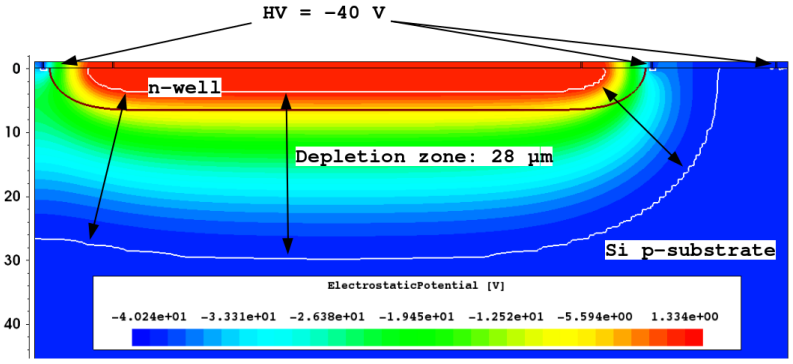

(c) Front-side biasing with extra HV contact outside the pixel matrix.

Figure 47.: Electrostatic potential and depletion zone for different biasing configurations schemes in a generic HV-MAPS with a 200 Ω cm substrate and -40 V external voltage. The color scale from sub-figure (c) describes the electrostatic potential for the three configurations.

contact. From this point, the electric field inside the depletion zone causes a decrease in the electrostatic potential in the substrate, and the width of the depletion zone as a function of the applied voltage is reduced compared with the backside biasing case (Figure 47b). The results show that back-side biasing produces a more homogeneous

depletion zone for a given voltage and resistivity.

A solution to the front-side biasing electrostatic potential reduction in the substrate is to bias the sensor using a high voltage contact outside the pixel matrix, as shown in Figure 47c. This contact keeps the substrate at the desired electrostatic potential, even for large depletions.

It is important to note that even if front-side biasing is used in most of the HV-MAPS prototypes, back-side biasing is possible and was studied in the work presented in [59].

Figure 48 analyzes how the depletion zone of HV-MAPS changes as a function of the substrate resistivity for a bias voltage of -60 V and -120 V, using TCAD simulation data and theoretical results. The plots show five different data sets. The first curve, in pink, is obtained from the theoretical model given by equation 20 (where V_{bi} was substituted by V_{ext} = -60 V and -120V). The second data set, in black, shows the results of a TCAD simulation of an abrupt "infinite" junction.

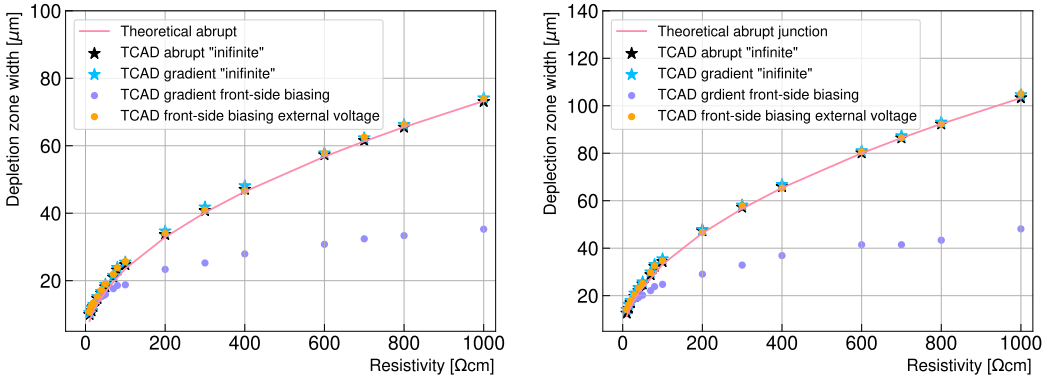

(a) -60 V. **(b)** -120V.

Figure 48.: Depletion zone width as a function of the resistivity for different pn-junction configurations and voltages, using TCAD simulation data and the theoretical results from the abrupt "infinite" junction model.

The third data set (in light blue) represents a gradient "infinite" junction. In the gradient n-well, the doping concentration near the junction is lower than in the case of the abrupt junction (Figure 49). Consequently, fewer carriers are available during diffusion to neutralize the charge created by the carriers that diffuse into the n-side of the junction. As a result, the depletion region extends slightly deeper into the n-well and less into the p-substrate than the abrupt junction, as shown in Figure 50. However, the total depletion width as a function of the resistivity still follows the theoretical results.

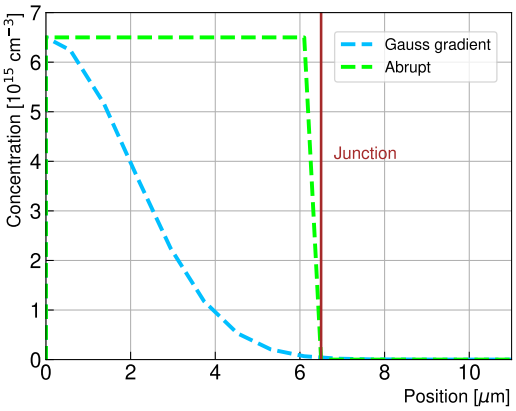

Figure 49.: Donor concentration inside the n-well for an "infinite" Gauss gradient and abrupt junction distribution.

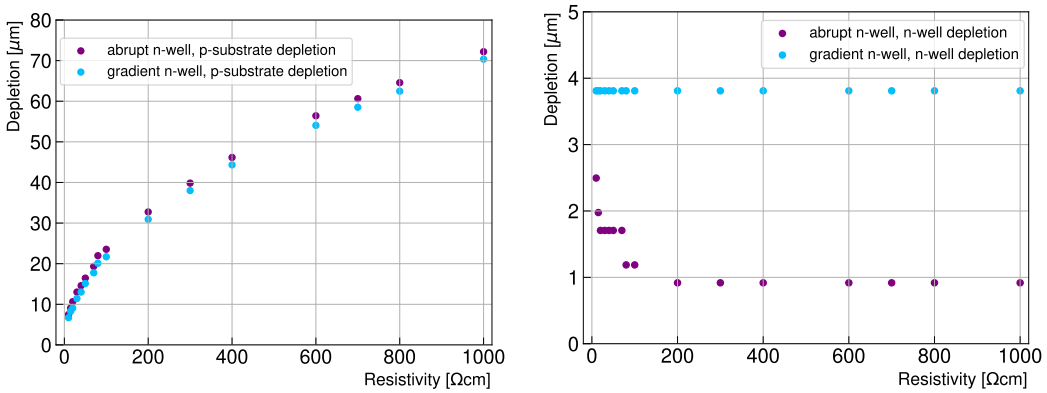

(a) p-substrate depletion width.

(b) n-well depletion width.

Figure 50.: TCAD simulation depletion width in an "infinite" abrupt and gradient pn-junction at -60 V bias voltage. Due to the lower concentration near the n-side of the junction for a Gaussian distribution, lower depletions depths are created inside the p-well (a) and larger inside the n-well (b) compared with the abrupt distribution. Due to the high concentration of dopants in the n-well compared with the p-substrates, the depletion inside the n-well is minimal and stays constant for most of the studied resistivities. For low resistivities (high concentrations of dopants) in an abrupt n-well, the concentration difference between the n-side and p-side of the junction is reduced enough to slightly increase the depletion inside the n-well compared with higher substrate resistivities.

In contrast to the other simulated structures, the depletion width data set of the basic gradient front-side biasing (purple), as the one shown in Figure 47a, does

not follow the theoretical predictions presented in subsection 2.3.1. This is due to the decreased electrostatic potential in the substrate when the depletion region touches the HV electrodes, resulting in a slower increase of the depletion zone. The introduction of the extra contact outside the pixel matrix results in a depletion zone (orange) that follows the theoretical predictions. If the HV contact is correctly placed, the depletion zone follows the expected behavior even for large voltages (Figure 48b). In the following this biasing structure will be used for the simulations to resemble the biasing ring connected around the pixel matrix in the HV-MAPS prototypes.

5.2.4. n-well

The HV-MAPS pn-junction can be described as a flat region with cylindrical-like shape edges. In the flat region, the diffusion process that creates the depletion zone occurs mostly in the vertical direction creating a more homogeneous electric field profile. However, in the edges, due to the cylindrical-like shape, the diffusion occurs in several directions, forming a cylindrical shell. This effect is sketched in Figure 51.

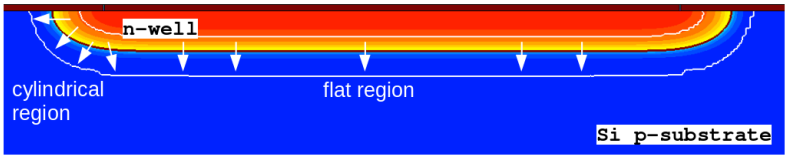

Figure 51.: Depletion zone of HV-MAPS in a 20 Ω cm substrate at -20 V. The n-well can be described as a flat region with cylindrical-like shape edges.

Figure 52 shows the depletion width in the center of the n-well for different n-well sizes in a generic HV-MAPS in a 400 Ω cm substrate at different voltages. The decrease in depletion width for small n-well sizes results from a decrease in the size of the flat region (bottom Figure 53). The full n-well tends to be cylindrical-like, creating diffusion in several directions. The charges near the pixel's center also diffuse to the lateral side of the n-well, decreasing the depletion width in the vertical direction for a given voltage and resistivity, as shown in Figure 53 for a 200 Ω cm substrate at -60 V.

5.2.5. Lateral depletion

The depletion in the horizontal direction (Figure 54) is a key parameter that needs to be considered in the design of HV-MAPS. The depletion zone must be wide enough to ensure that the charge created for an incident particle is collected independent of

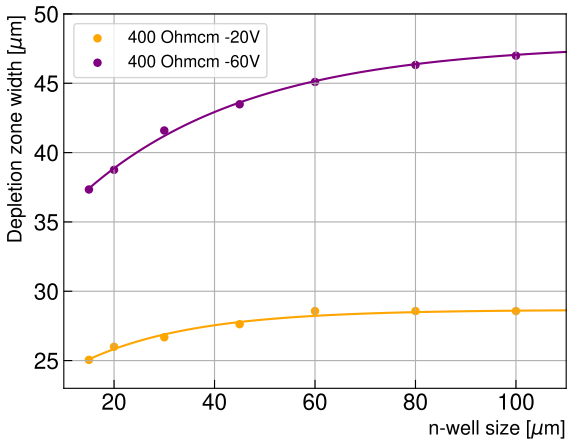

Figure 52.: Depletion zone width as a function of the n-well size in a generic HV-MAPS in 400 Ω cm substrate at different bias voltages with external contact.

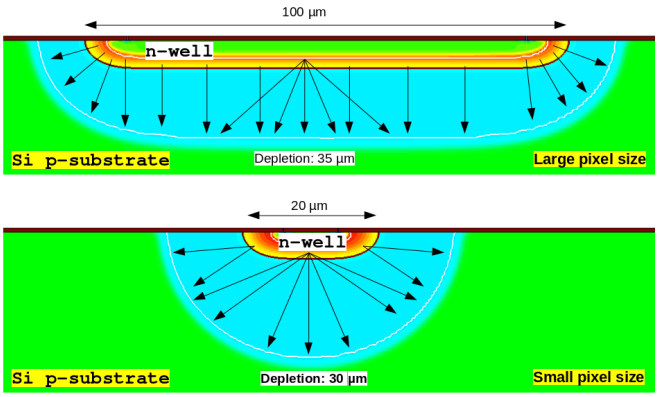

Figure 53.: TCAD simulation of the effect of the n-well size over the depletion width in a 200 Ω cm substrate at -60 V. As the n-well size decreases, the flat region (represented in the upper figure) decreases. As a result, the n-well tends to have a cylindrical-like shape (represented in the bottom figure). The cylindrical-like shape creates diffusion in several directions, resulting in lower depletion zones in the vertical direction.

the in-pixel position. One solution is to increase the n-well area closer to the pixel edge. However, an increase in the n-well area is limited by the fabrication process, the maximum operable pixel capacitance, and spatial resolution.

The width of the lateral depletion depends on the voltage, doping, and thickness of the n-well. The thickness of the n-well and concentration are process parameters, but the working voltages and resistivities can be considered for the pixel design.

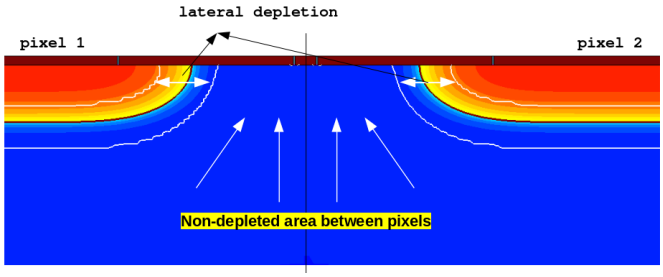

Figure 54.: Lateral depletion of HV-MAPS in a 20 Ω cm substrate at -20V.

Figure 55 presents the lateral depletion near the Si/SiO_2 interface (1 µm) as a function of the substrate resistivity for different voltages. The behavior with resistivity and voltages is similar to that in the vertical direction but with a width reduction up to ∼50 µm in the study range. This reduction in the horizontal direction is due to the cylindrical-like shape growth of the depletion zone in the pixel edge.

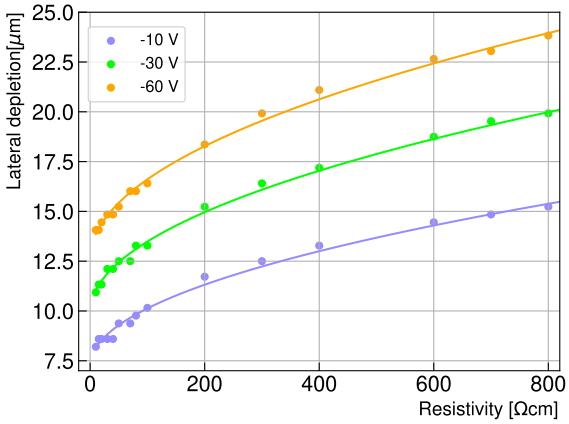

Figure 55.: Lateral depletion of HV-MAPS as a function of the resistivity for different applied voltages in a 62 µm n-well.

For good detection efficiencies, the detector design needs not only to consider the point where the lateral depletion close to the Si/SiO_2 interface reaches the pixel edge but also that deeper in the substrate, the lateral depletion reaches the pixel edge. This way, enough depletion would be created to avoid inefficiencies in the inter-pixel region.

Figure 56 shows two examples of lateral depletion. In Figure 56a, the depletion reaches the pixel edge, but most of the inter-pixel region is still undepleted. A higher operational voltage assures larger depletions in the inter-pixel region, as shown in Figure 56b. Despite the larger depletion due to the shape of the depletion zone, the

vertical depletion in the inter-pixel region is smaller compared with the center of the depletion in the center of the pixel.

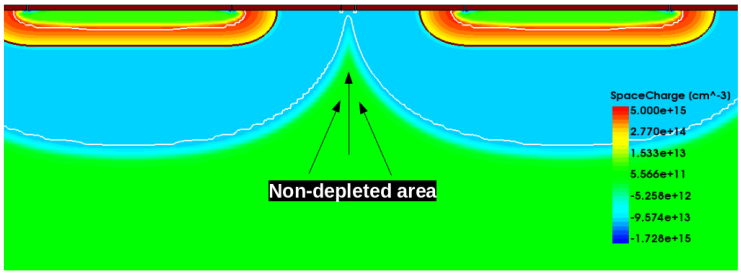

(a) -60 V.

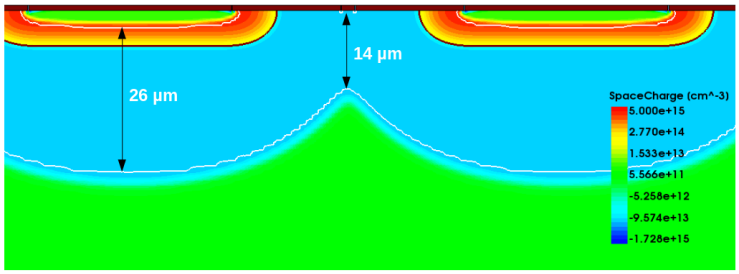

(b) -100 V.

Figure 56.: Lateral depletion simulation in a 80 Ω cm substrate for a 80x80 µm^2 pixel size and 62x62 µm^2 n-well. (a) At -60 V, the depletion reaches the pixel edge, but a large undepleted area is observed in the inter-pixel region. A larger voltage of (b) -100 V assures a good vertical depletion in the inter-pixel region.

5.2.6. 2D Vs 3D Simulations

Given the computational limitations of 3D simulations, most of the results presented in this thesis employ 2D TCAD simulations for device modeling. The use of 2D simulations allows for a faster and more efficient exploration of the device's behavior under various operating conditions.

Previously it was demonstrated that a flat-like shape of the n-well creates larger depletion zones than in the case of a cylindrical-like shape. In a 2D simulation for a large n-well, the bottom of the n-well can be considered to have a flat-like shape, but in a 3D simulation, this will depend on the size of the n-well in the transverse direction.

For large pixel sizes in both directions, the bottom of the n-well can still be considered a flat-like (plate) region (Figure 57a) that creates larger depletion, but if

one or both directions have a small size, then the n-well can be considered to have a cylindrical-like shape (Figure 57b).

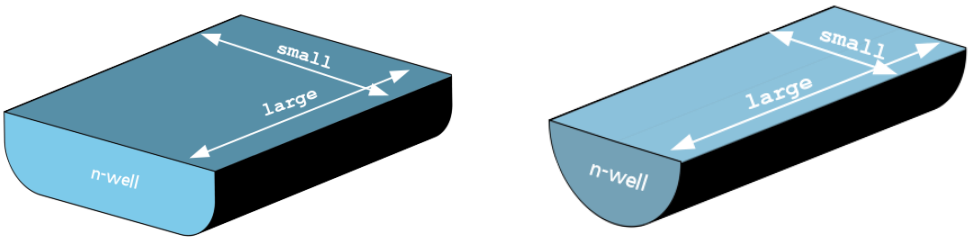

(a) Large size in both directions. **(b)** One small and one large direction.

Figure 57.: 3D sketch of the n-well shape dependence on the transverse size. (a) For large pixel sizes, in both directions, the bottom of the n-well has a flat-like shape. (b) If one direction is small, then the n-well can be considered to have a cylindrical-like shape.

Using TCAD SDEVICE, the depletion of three different n-well structures was simulated in 3D and compared with similar structures in 2D. Figure 58a presents the obtained results. The bars represent the 3D depletion for the three different n-well, while the lines show the depletion for similar structures in 2D. The first two bars, 25x25 and 25x62 µm^2, in Figure 58a show equal depletion, concluding that the depletion depth is dominated by the side of the n-well with the smallest length.

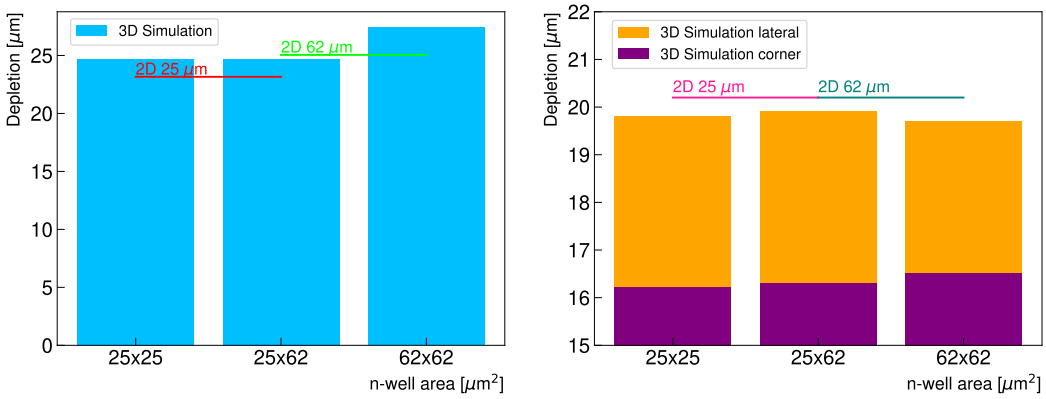

(a) Vertical depletion. **(b)** Lateral depletion.

Figure 58.: Vertical and horizontal (edges and corners) depletion width for different n-well sizes in a 300 Ω cm substrate at -60V. The bars represent the depletion width results obtained using 3D simulation, while the lines represent the results for 2D TCAD simulations.

Compared to the other two, the third n-well size, 62x62 µm^2, shows the previously explained behavior of a slight increase in depletion zone for a large n-well size. Given the computational constraints and just a slight increase (∼2 µm) in depletion, 2D simulations can accurately estimate the depletion zone and be a viable alternative to 3D simulations.

In the lateral depletion, Figure 58b shows that the depletion width is independent of the n-well size and, therefore, well estimated with the 2D simulations (less than 1 µm difference). However, the corners of the n-well have a spherical-like shape, increasing the diffusion directions and resulting in a smaller depletion zone than the lateral depletion obtained with 2D TCAD simulation.

The depletion in the corners has to be carefully considered in the HV-MAPS design since it can cause inefficiencies if the depletion zone doesn't extend to the whole pixel area. Figure 59 shows a sketch of the corner effect. For a pixel size of 80x80 µm^2 and an n-well of 44x44 µm^2 in a 300 Ω cm substrate at -20 V.

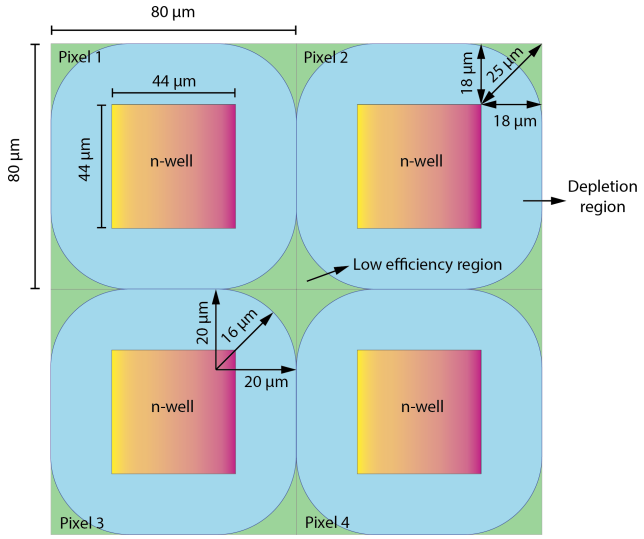

Figure 59.: Sketch of the depletion at the pixel corner for a pixel size 80x80 µm^2 and n-well of 44x44 µm^2 in a 300 Ω cm substrate at -60 V. The blue lines represent the lateral and corner diffusion. The purple area illustrates the undepleted area at the pixel corner.

If only lateral depletion is taken into consideration, due to the smaller depletions in the corner and the larger distance between the n-well and the pixel corner, the depletion does not reach the pixel corner, and as a result, charges are slowly collected via diffusion, causing inefficiencies, mostly at high thresholds (Chapter 7).

This effect was studied using TCAD simulation for the MuPix8 pixel structure.

Figure 60 shows the depletion width using a 2D cut of a 3D SDEVICE TCAD simulation results of the MuPix8 pixel in a 80 Ω cm substrate biased to -15 V. The results show that MuPix8 does not reach full depletion in the corner of the pixel for the study voltage. These findings correlate with the experimental results of the in-pixel efficiency presented in [77].

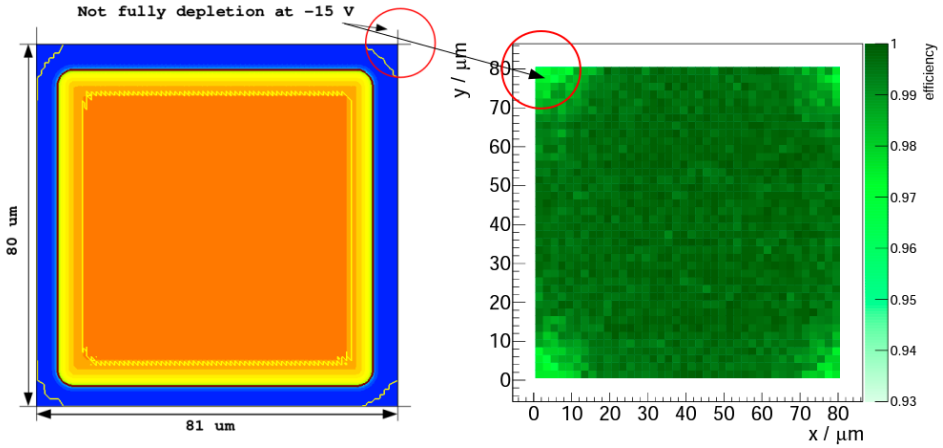

Figure 60.: 3D TCAD simulation study of the in-pixel efficiency in the MuPix8 pixel structure with pixel size 81x80 µm^2 and n-well size 63x63 µm^2 in an 80 Ω cm substrate at a bias voltage of -15 V [77]. The yellow line in the left figure represents the borders of the depletion zone.

5.2.7. MuPix10 depletion zone

This subsection studies the current-voltage characteristic (IV curve) of the MuPix10 HV-MAPS prototype. The experimental results reveal a sudden increase of leakage current at different voltages for different thicknesses, as shown in Figure 61 [78]. One explanation for this behavior is a high surface current contribution to the leakage current when the depletion region extends to the backside of the sensor due to a layer of damaged silicon created as a result of backside grinding (Subsection 2.1.5). Reports on this effect have been made before (e.g. [26]), and an additional etching step after backside grinding was found to mitigate it. To study the effect of the etching step over the current-voltage characteristic in HV-MAPS, the MuPix11 sensor (with the same pixel structure that MuPix10) is produced in similar wafer resistivities with a 50 µm thickness and processed with plasma etching.

TCAD simulations can be used to estimate the substrate resistivity of the wafer using the IV curves of the different sensor thicknesses. To this end, the experimental

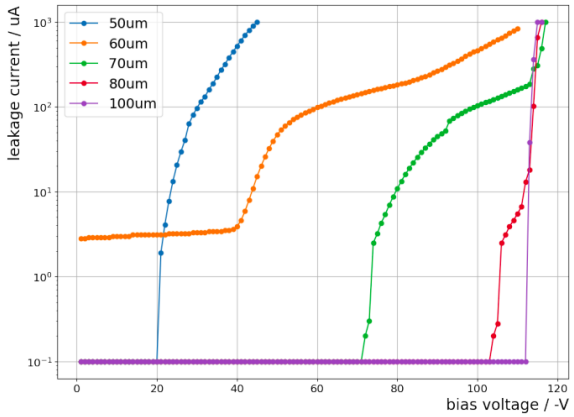

Figure 61.: IV curve for MuPix10 samples with different thicknesses. Each curve corresponds to a different sensor thinned down by mechanical grinding. [78]

breakdown voltages [3] (BDV) as a function of the sensor thicknesses are presented in Figure 62. Following the pn-junction equations where the depletion zone width (W) increases proportionally to the square root of the voltage ($\sqrt{V}$), the BDV results are fit with a quadratic equation (V$\propto W^2$). The data points and the fit agree very well, except for the last data point. This discrepancy can be explained if the BDV, for this sensor thickness, happens before the depletion zone reaches the backside of the detector.

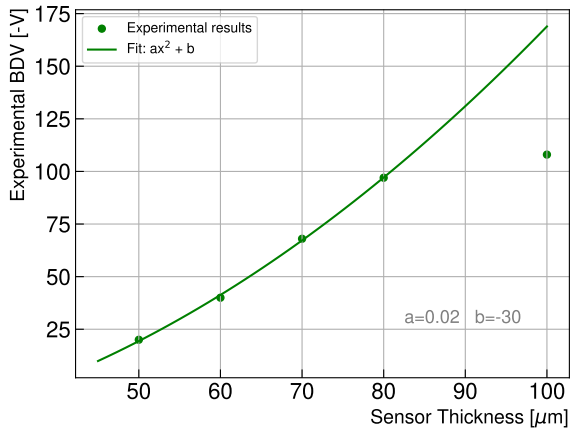

Figure 62.: MuPix10 experimental BDV results for different sensor thicknesses.

[3] Measured as the critical point where the current suddenly increases. The exact values are obtained by extrapolating the data points after the sudden increase to zero current.

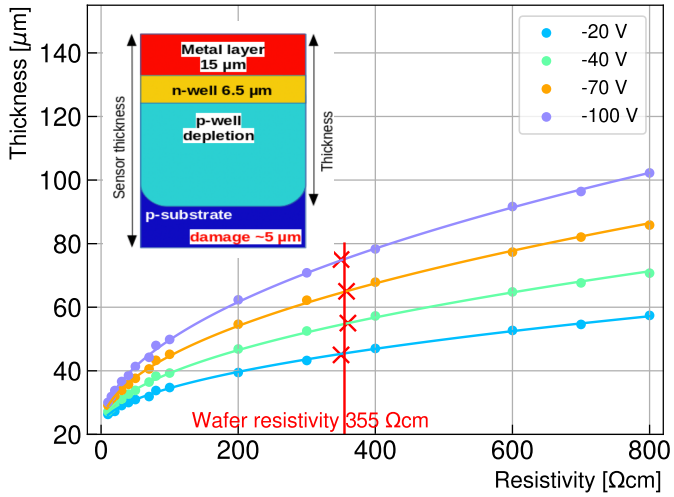

Figure 63.: Wafer resistivity estimation using TCAD simulation depletion values for different substrates resistivities and MuPix10 experimental BDV for the different thicknesses. Each thickness is intercepted with its corresponding voltage curve (the curve that follows the BDV obtained experimentally for each sensor thickness), as outlined by the red crosses. Subsequently, the wafer resistivity is obtained as the resistivity corresponding to the matched voltage curve.

Figure 63 shows the thickness (defined as the sum of the depletion zone inside the p-substrate, the n-well, and the metal layer) as a function of the substrate resistivity for different voltages. The selected voltages are those for which the different sensor thicknesses reach breakdown[4]. To estimate the wafer resistivity, each thickness is intercepted with its corresponding voltage curve (the curve that follows the BDV obtained experimentally for each sensor thickness), as outlined by the red crosses in Figure 63. Subsequently, the wafer resistivity is obtained as the resistivity corresponding to the matched voltage curve.

It is important to note from Figure 63 that the y-axis values used to intercept the voltage curves do not correspond exactly with the substrate thicknesses. A ∼5 µm damage layer at the back of the sensor has been reported [79] due to mechanical damage from grinding. Accordingly, the voltage curve has been associated with a thickness equal to the sensor thickness minus the 5 µm damage layer (e.g., the sensor with a thickness of 50 µm has a BDV of -20 V. The resistivity was estimated by

[4]The BDV for the 100 µm sensor was excluded from the analysts since the sudden increase in leakage current seems to be the effect of a high electric field in the inter-pixel area. This effect is studied in Section 5.3

intercepting a thickness of 45 µm with the -20 V depletion curve. The intercept corresponds to a resistivity of 355 Ω cm). All the different thicknesses result in a 355 Ω cm resistivity. The resulting value is inside the 200-400 Ω cm range reported by the wafer supplier.

5.3. Inter-pixel Region

When ionizing particles cross the oxide layer, holes from the electron-hole pairs generated can get trapped in the oxide. The oxygen valence electrons at the interface create deep local traps for those holes. The mobility of electrons in SiO_2 (20 cm^2/Vs) is higher than for holes (2x10^{-5} cm^2/Vs). Consequently, electrons are rapidly collected while holes accumulate near the interface [80]. This accumulation creates a positive charge layer, attracting free electrons from the silicon to form a compensating layer of free carriers at the Si-SiO_2 interface, as shown in Figure 64. Tunneling is the only mechanism by which carriers can cross the interface potential barrier, and only a few carriers can do so, leaving the charged layer, called an inversion layer, almost permanently at the interface.

The presence of this electron layer at the interface can form a conductive path between different electrodes, increasing crosstalk and leading to unwanted parasitic leakage paths in the sensor. The density of this charged layer varies almost linearly with the exposed fluence from 2x10 to 3x10^{12} ^{11} n_{eq}/cm^{-2} between 0 and 10^8 rad [28].

5.3.1. Crosstalk

The phenomenon of crosstalk occurs when a signal is collected on one pixel, and through capacitive coupling, it also induces a signal in its neighboring pixels. This can result in a higher fraction of double and triple hits that need to be considered when reconstructing the position of the charge. Crosstalk can cause false signals, reduce the signal-to-noise ratio, and compromise the accuracy of the detector measurements. The induced signals on the neighboring pixels can lead to errors in position reconstruction, making it challenging to accurately determine the exact location of the track.

Figure 65 shows an example of the effect of cross-talk in an HV-MAPS with an interface trap concentration of 2x10^{11} cm^{-2}. A two pixels structure is simulated when a MIP particle with a linear energy transfer (LET) of 1.8x10^{-5} ps µm^{-1} hits one of the pixels in the center of the n-well (Figure 66). The current collected in the two neighbour pixels in a 5 ns time interval for a 40 µm sensor is simulated, and Figure 65 shows the integrated charge results.

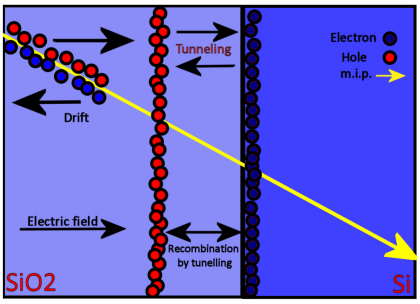

(a)

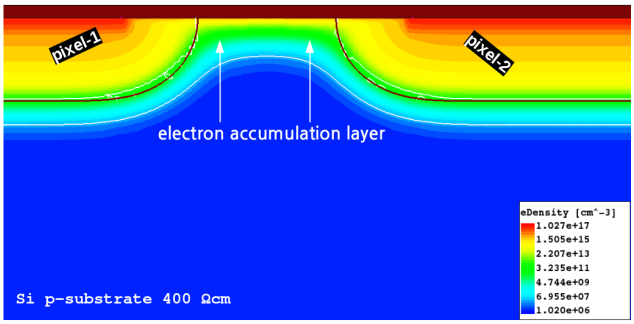

(b)

Figure 64.: Electron accumulation layer formation process and results. (a) Schematics of radiation damage effect at the Si-SiO_2 interface. [81]. (b) TCAD simulation of electron density in the inter-pixel region in a generic HV-MAPS with a 400 Ω cm substrate and an interface trap concentration of 2x10^{11} cm^{-2}.

The SDEVICE simulation reveals a collected charge in the neighbor pixel due to crosstalk of ∼36% from the total deposited charge, only ∼13.5% less than the charge collected in the hit pixel. The crosstalk between adjacent pixels depends on the distance between the n-wells, the size of the n-well, and the applied voltage. To reduce the impact of crosstalk, techniques such as using an insulation layer between pixels can be employed, which decreases the electron accumulation layer and minimize the induced charge. This layer is typically created by adding additional implants to the Si substrate.

5.3.2. Inter-pixel Isolation

There are two primary methods to create the isolation layer: the *p-stop* and *p-spray* techniques [28]. The p-stop technique (Figure 67) utilizes high-dose p implants between the two n-wells (Figure 67a) to interrupt the conductive electron layer

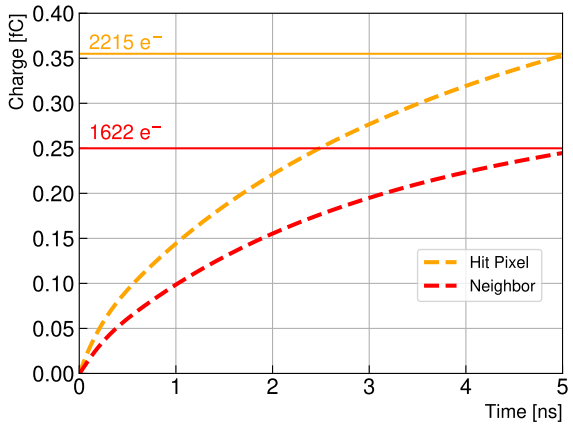

Figure 65.: TCAD simulation integrated charge during a 5 ns time interval for a 40 µm HV-MAPS with pixel size of 80 µm^2 in a 400 Ω cm substrate at -20 V with an interface trap concentration of 2x10^{11} cm^{-2}, without isolation.

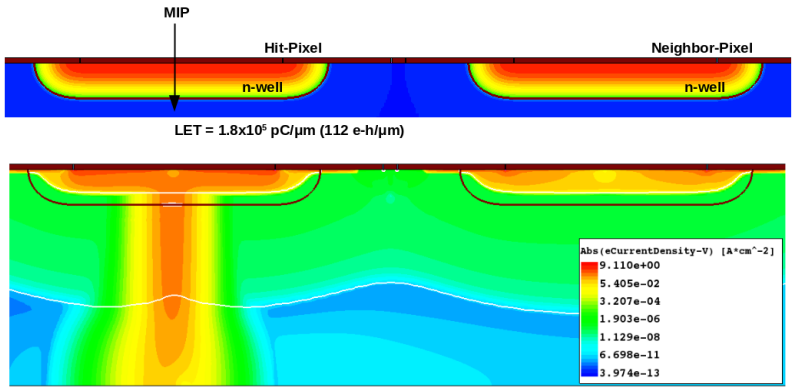

Figure 66.: Upper sub-figure shows the MIP trajectory in the generated TCAD SDE structure. The bottom sub-figure shows the electron current density 2 ns after the particle hit the sensor. LET is defined as linear energy transfer.

created by the fixed positive layer in the interface (Figure 67b). An additional mask during the sensor manufacturing is required to achieve precision in the alignment of the p-stop implants, resulting in a more expensive process than the p-spray. The necessary alignment tolerances also limit the minimum spacing between two n-wells.

Figure 68 presents the effect on the accumulation layer for different p-stop concentrations in a 400 Ω cm substrates with an interface concentration of 2x10^{11} cm^{-2}. If the p-stop concentration is insufficient, the electron layer will keep connecting the

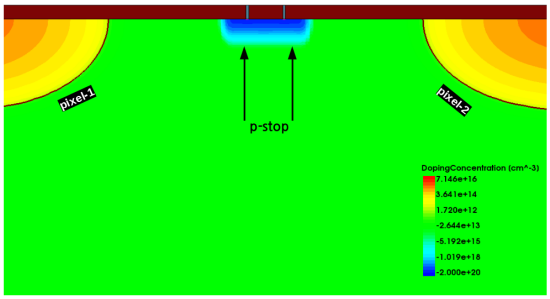

(a) TCAD SDE simulation of the doping concentration distribution using a high dose p-stop implant.

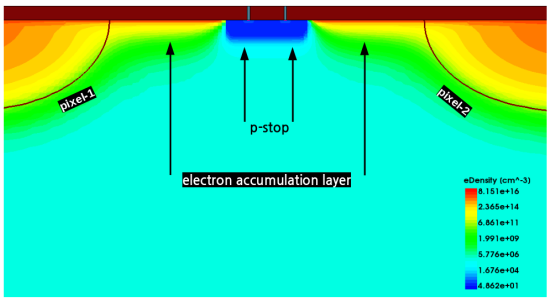

(b) Electron density distribution using the p-stop technique. The accumulation layer is interrupted.

Figure 67.: P-stop pixel isolation technique using a high boron dose implant in the inter-pixel region with a concentration of $2x10^{20}$ cm^{-3} .

two n-wells (Figure 68a). For a higher p-stop concentration, the accumulation layer might be interrupted (Figure 68b).

Figure 69 shows the integrated charge induced in the neighbor pixel for a MIP with a LET of 112 e-h/µm in a 40 µm thickness, and for a p-stop concentration of $1x10^{20}$ cm^{-3}. The used p-stop concentration results in an induced charge in the neighbor pixel of ∼29% from the total deposited charge, ∼7% less than for the non-isolation case. The effect of the p-stop depends on the concentration and size of the implant. While high concentrations are ideal for reducing the crosstalk further, high electric fields created at the junction between the p-stop and the accumulation layer reduce the detector's maximum operating voltage.

The electric field distribution in the inter-pixel region is shown in Figure 70. The high electric field at the edge of the p-stop is visible. The high doping concentration from the p-stop is not the only factor determining the BDV, the concentrations of electrons in the accumulation layer also contribute to reducing the operating voltage. As a result, after irradiation, when the accumulation of electrons increases, higher electric fields and lower BDV are expected.

Conversely, the p-spray method involves the application of a medium-dose p-spray

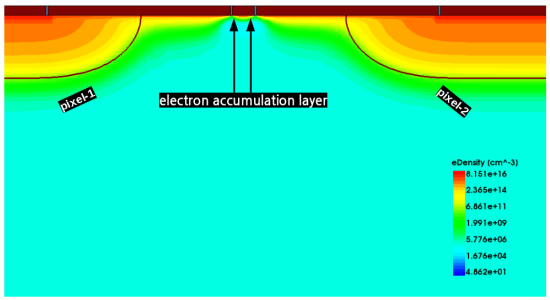

(a) 1x10^{15} cm^{-3}.

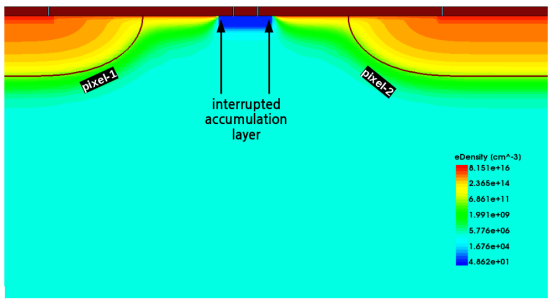

(b) 1x10^{20} cm^{-3}.

Figure 68.: Electron density for different p-stop concentrations for an interface charge concentration of 2x10^{11} cm^{-2} in a 400 Ω cm substrate.

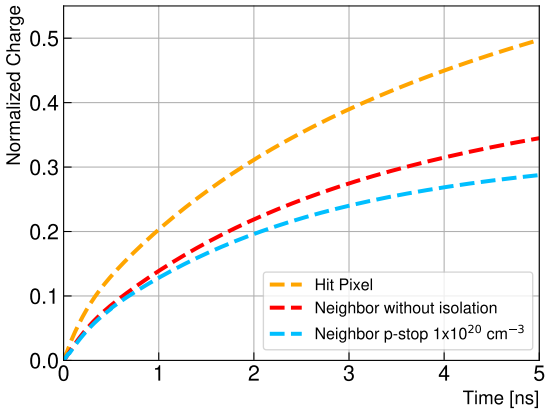

Figure 69.: Integrated charge in a 400 Ω cm substrate at -20 V with an interface charge concentration of 2x10^{11} cm^{-2} and a p-stop concentration of 1x10^{20} cm^{-3}. The particle pass by the middle of the n-well with an equivalent energy transfer of 112 e-h/µm in a 40 µm thickness.

implant to the entire wafer, compensating for the accumulated electrons everywhere (Figure 71). The absence of a photolithographic step is an advantage of this technique because it allows for narrow spacing between neighboring n-wells.

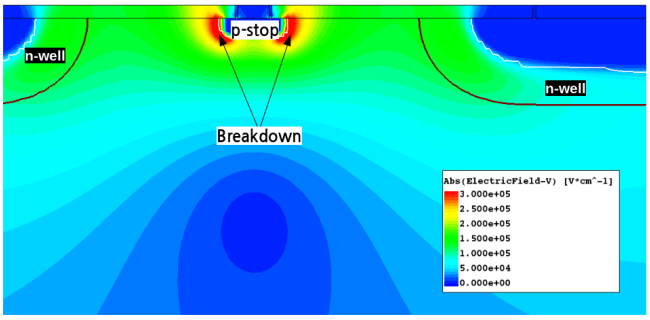

Figure 70.: Electric field distribution in the inter-pixel region. A high electric field is created at the edge of the p-stop between the high concentration of electrons in the accumulation layer and the high dose of boron used for insulation.

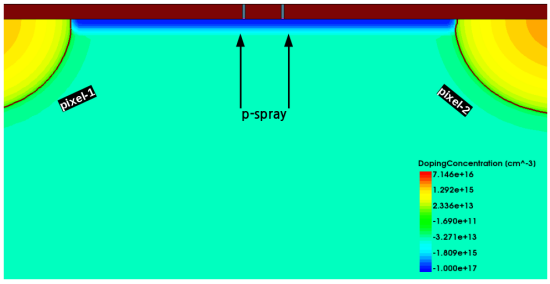

(a) TCAD simulation of the doping concentration distribution using a medium dose p-spray implant.

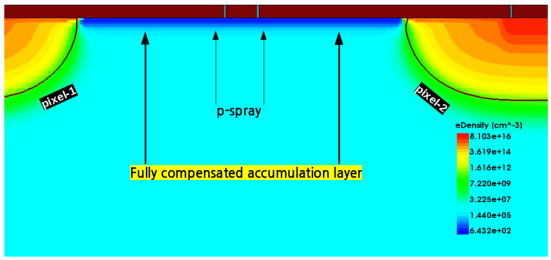

(b) Electron density using the p-spray technique. Fully compensated accumulation layer.

Figure 71.: Electron density for a p-spray pixel isolation technique using a medium boron dose implant to the entire wafer with a concentration of $1x10^{17}$ cm^{-3}.

Equally, as in the p-stop case, if the p-spray concentration is too small, insufficient electrons will be compensated, and the accumulation layer will remain. In the opposite case, when a high p-spray concentration is used, for example, to assure good isolation after irradiation, the holes will outmatch the number of electrons in the accumulation layer before irradiation, and a high density of holes will be presented

in the inter-pixel region (Figure 72). As a result of the excess of holes, a high electric field is created between the insulation layer and the n-well (Figure 73). After irradiation, when the interface traps are increased, and more electrons are attracted, the number of holes will be reduced, and an increase in the BDV is expected.

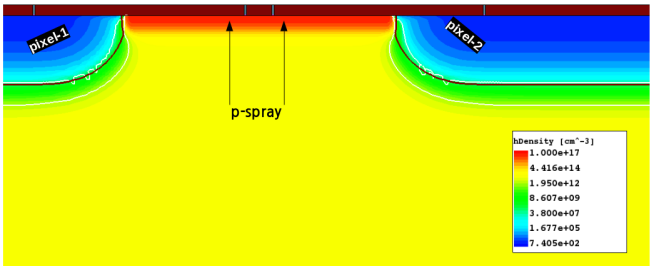

Figure 72.: Hole density for a p-spray concentrations of 10^{17} cm^{-3} and an interface charges of 3x10^{11} cm^{-2} in a 400 Ω cm Si substrate.

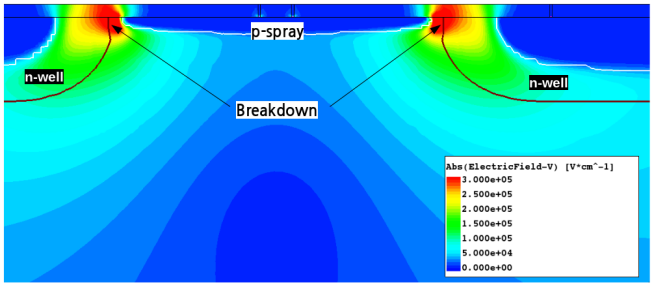

Figure 73.: Electric field distribution in the inter-pixel region. If a high p-spray concentration is used to isolate the pixels, a high electric field is created between the n-well and the excess of holes from the isolation layer.

Figure 74 shows the charge collected in the neighbor pixel for a MIP with a LET of 112 e-h/µm in a 40 µm thickness, for two p-spray concentrations, 5x10^{15} and 1x10^{17} cm^{-3}, in a 400 Ω cm substrate at -20 V with an interface charge of 2x10^{11} cm^{-2}. While the lower concentration result in similar crosstalk compared to the p-stop case (since not all the electrons were compensated), the highest p-spray concentration simulated offers good isolation and results in an induced charge in the neighbor pixel of ∼14% from the total deposited charge, ∼15% less than the p-stop case and ∼22% less than for the non-isolation.

The p-spray and p-stop concentration is part of the foundry process and can not be optimized during the sensor design, but a good understanding of their effect on the detector performance can help to optimize the inter-pixel region design and explain the detector behavior.

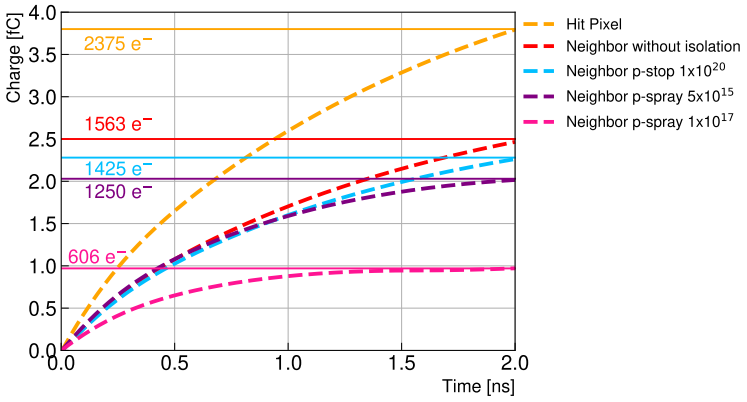

Figure 74.: Integrated charge in a 400 Ω cm substrate at -20 V with an interface charge concentration of 2x10^{11} cm^{-2} using p-spray and p-stop isolation technique. The particle pass by the middle of the n-well with an equivalent energy transfer of 112 e-h/µm in a 40 µm thickness.

5.3.3. Breakdown Voltage

In an infinite pn-junction, the maximum electric field and breakdown point are at the junction, and its strength is determined by the doping concentration and the potential difference across the junction, as discussed in subsection 2.3.1. In a detector pn-junction, the n-well exhibits curved edges due to the lateral-diffusion effect, resulting in an increased electric field at these edges (Figure 75). The curvature causes the electric field lines to bend towards the region of higher doping concentration, resulting in a higher density of electric field lines near the junction edges. The strength of this electric field depends not only on the curvature of the junction but also on factors such as doping levels and potential differences. Consequently, substrates with lower resistivity and higher voltage configurations tend to exhibit a stronger electric field at the junction edges.

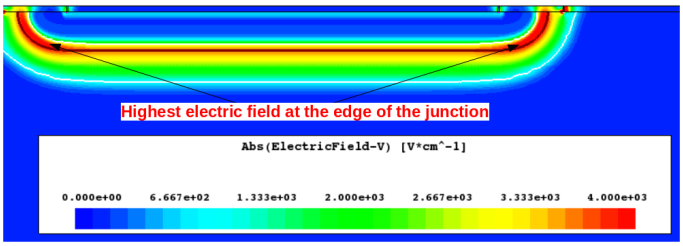

Figure 75.: Electric field distribution. The higher electric field at the edge of the junction is highlighted.

In an ideal detector pn-junction, the breakdown voltage can reach values larger than -200 V, especially for high-resistivity substrates. But in reality, HV-MAPS shows lower breakdown voltage. TCAD simulation was used to study their breakdown point.

The p-spray technique creates large electric fields between the implant and the n-well. The high electric field can reduce the breakdown voltage to values under -100 V. The lowest electric field is reached when the p-spray boron implant matches the oxide charge's saturation value. However, if the implantation dose is too low, the isolation might not be sufficient to compensate for all the electrons. Therefore, it is a common practice to use implant doses slightly higher than the necessary concentration to compensate for process variations during manufacturing. To improve the highest operable voltage of devices with p-spray while keeping good isolation, an alternative p-spray technique can be used. A low dose p-spray is placed around the pn-junction to improve the voltage performance, and a high boron dose is implanted in the middle of the gap to ensure good isolation (Figure 76).

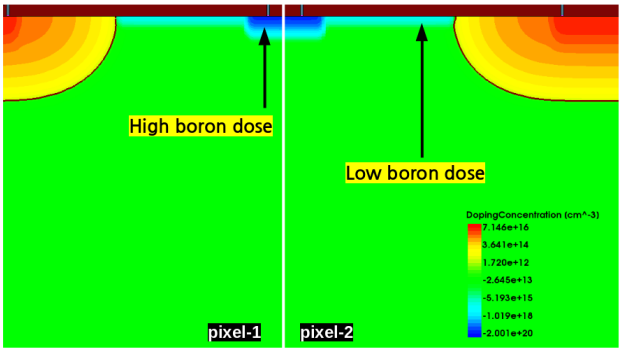

Figure 76.: Doping concentration distribution for an alternative p-spray technique.

Figure 77a shows the charge induced in the neighbor pixel, including an example of the modified p-spray technique. For this case and the used oxide charge ($2x10^{11}$ cm^{-2}), the induced charge in the neighbor pixel is ∼22% from the total deposited charge (17% lower than the p-stop case and 13.5% higher than the p-spray). The advantage of this technique is that the breakdown voltage increases (Figure 77b) while keeping better isolation than when only the p-stop is employed. The moderate p-spray reduces the accumulation layer and accordingly behaves as a p-stop insulation with a lower crosstalk and electric field.

For the modified p-spray (and the p-stop technique), a shorter mask between the n-well and the high-dose boron implant decreases the breakdown voltage (Figure 77c).

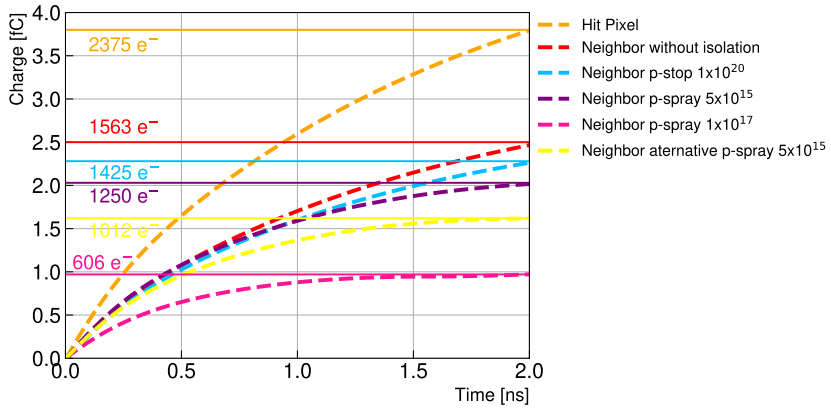

(a) Integrated charge using different pixel isolation techniques.

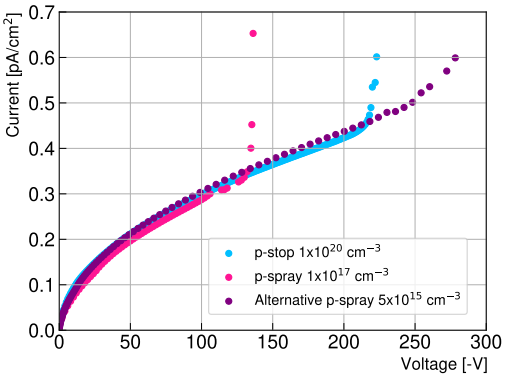

(b) Current-Voltage curves for different pixel isolation techniques. For the modified p-spray technique, the high dose boron implant is placed 16µm from the n-well.

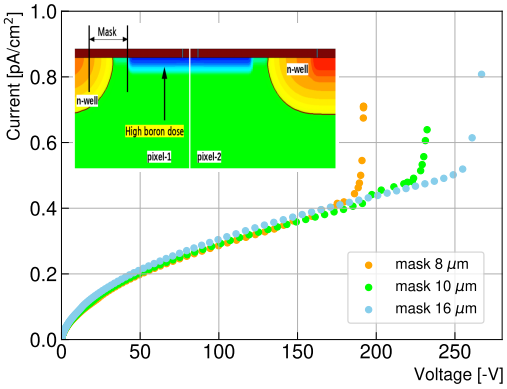

(c) Current-Voltage for different distances (defined as "mask") between the n-well and the high dose implant. For a short mask the implant behave as a p-spray.

Figure 77.: Integrated charge and breakdown voltage for a 400 Ω cm substrate at -20 V with oxide charge of 2x10^{11} cm^{-2} for the different isolation techniques. The inter-pixel distance was set to 36 µm. Note that due to the lateral diffusion during the n-well implantation, the distance between the n-well and the high boron implant is lower than the layout design (c).

A smaller gap between pixels has the same effect on the breakdown since the high boron dose implant would be closer to the n-well. The mask is not the only factor affecting the breakdown. The first metal layer (M1) is used to bias the sensor (Figure 78), and the shape of the electric field is influenced by its design (Figure 78a). The short distance between the M1 connecting the n-well and the substrate results in large electric fields due to a fast change in the potential in the area between the two

M1 (Figure 78b). An increase in this distance results in higher breakdown voltages, as shown in Figure 78e.

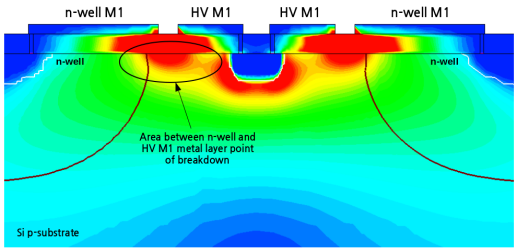

(a) Electric Field under M1

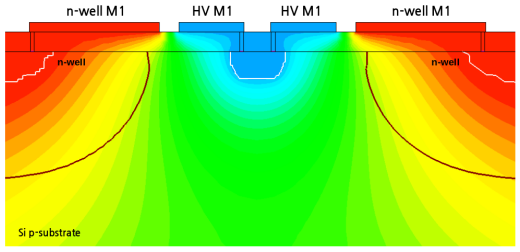

(b) Electrostatic Potential under M1

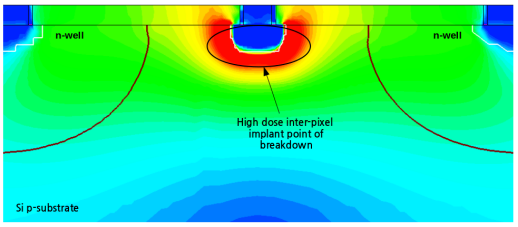

(c) Electric Field without M1

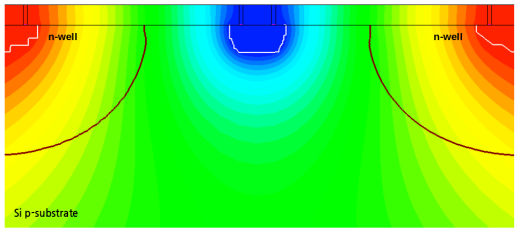

(d) Electrostatic Potential without M1

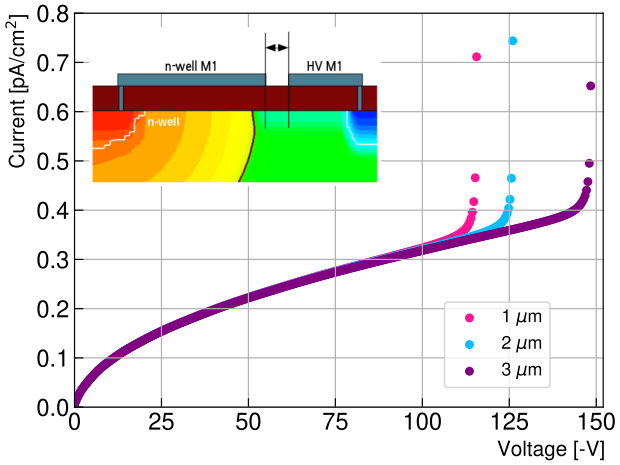

(e) Current-Voltage characteristic for different distances between the metal layer used to bias the substrate and n-well.

Figure 78.: Electric Field distribution and current-voltage characteristic as a result of a short distance between the metal layer used to bias the substrate and n-well.

The breakdown (Figure 78a and 78c) depends on the doping concentration, interface charges, gap between pixels, metal layer, and mask size. The concentration of the isolation is a process parameter, but the inter-pixel dimension can be simulated to predict the sensor breakdown voltage and optimize the design.

5.3.4. MuPix10 breakdown voltage

HV-MAPS prototypes have been produced in different wafer resistivities. To study the effect of the resistivity over the breakdown in the inter-pixel area, the MuPix10 pixel design is used. Figure 79 presents some of the dimensions affecting the breakdown voltage. Since the concentration of the compensation implant is unknown, various concentrations were studied and tuned later to the experimental breakdown values.

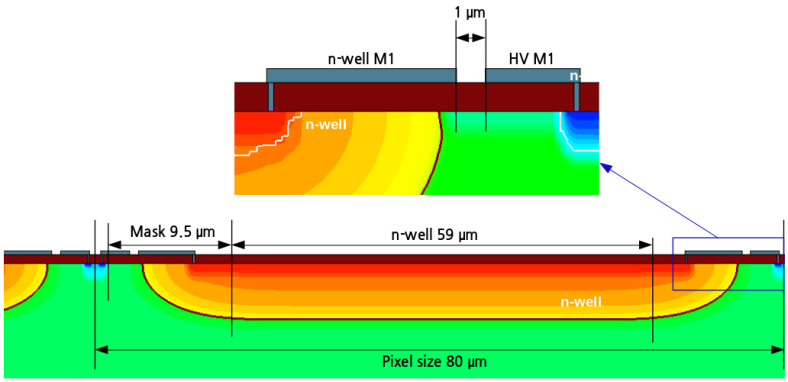

Figure 79.: MuPix10 pixel structure dimensions.

The electron accumulation layer behaves differently based on the resistivity of the substrate. Lower resistivity p-substrates with higher doping concentrations result in a smaller accumulation layer. The accumulation layer is formed from excess electrons that do not recombine with the acceptor atoms near the interface when they are attracted to the oxide charges. Lower resistivities have more acceptor atoms available for recombination, resulting in a smaller accumulation layer. When extra boron atoms are added to create the implant (assuming that the same dose was used to create the isolation for all the substrates), a lower concentration is more effective in fully or partially compensating the accumulation layer of lower resistivity substrates. Fewer electrons in the accumulation layer generate smaller electric fields with the high-dose implant, similar to the p-stop technique (Figure 80a and 80b). Consequently, low resistivity substrates have higher breakdown voltages. This correlates with the MuPix10 current-voltage studies, where sensors with ± 400 Ω cm substrate resistivity show breakdown around -110 V and those with a substrate ± 10-20 Ω cm that breaks down at -130 V.

Figure 81 shows the effect of different p-spray concentrations. As the p-spray dose increases to values over the interface saturation, the excess of holes produces lower breakdowns with the n-well, similar to the p-spray technique. An optimum

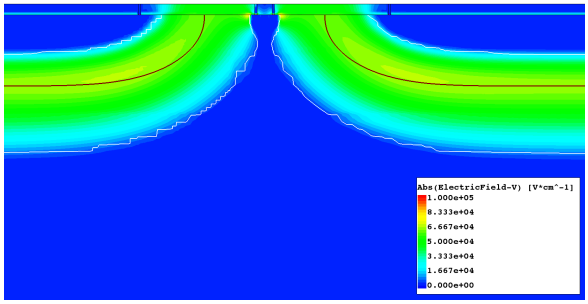

(a) 20 Ω cm substrate

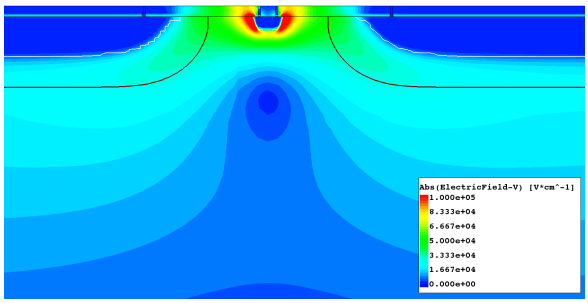

(b) 400 Ω cm substrate

Figure 80.: Effect of a modified p-spray technique in two substrate resistivities with oxide charge 2x10^{11} cm^{-2}. Lower p-spray concentration 1x10^{14} and high concentration 1x10^{18} cm^{-2}.

concentration for the inter-pixel isolation needs to consider the wafer resistivity. Since lower resistivity substrates reach full compensation, for lower p-spray concentrations, for certain concentration ranges in the simulated structure (e.g., 5x10^{16} cm^{-3} in Figure 81), the lower resistivity substrates might have lower breakdown voltage than high substrate resistivity sensors. This behavior was observed for the MuPix8 sensors [82].

Figure 82 shows the tuned breakdown voltages obtained for the MuPix10 structure (including the M1 structure). Without previous knowledge of the doping concentration used for isolation, it is difficult to predict the exact value of the breakdown voltage, but the tuned results can be used to describe the experimental behavior.

5.4. Pixel Capacitance

The pixel capacitance is another of the parameters that can be studied with TCAD simulations. Capacitance is a sensitive parameter in the operation of a silicon tracking detector, as it directly affects the signal-to-noise ratio and the detector's response

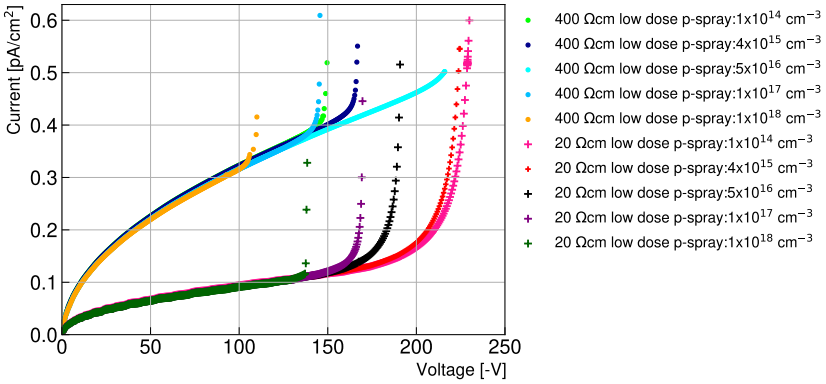

Figure 81.: Current voltages characteristic for a MuPix10-like (without M1) in a 400 and 20Ω cm substrate with 2x10^{11} cm^{-2} oxide charges. The high doping implant has a boron concentration of 1x10^{18} cm^{-3}.

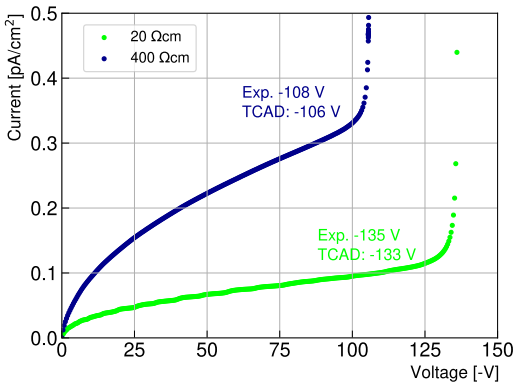

Figure 82.: TCAD current-voltage characteristic for MuPix10 with 2x10^{11} cm^{-2} oxide charges and a modified isolation technique with a high boron concentration of 1x10^{18} cm^{-3} and p-spray of 2x10^{16} cm^{-3}.

time. In addition, the capacitance between a pixel and its neighbor determines the crosstalk level. Typical Si detector electronics are designed to operate with pixel capacitances in the order of 1x10^2 fF. The total capacitance (C$_{det}$) presented by a pixel to the front-end electronics includes several components (Figure 83). One of them is the inter-pixel capacitance (C$_i$), which is dominated by the contributions between the pixel and its eight nearest neighbors in the array. The second is the junction capacitance (C$_j$) between the pixel electrodes. In addition to those, an HV-MAPS might have other significant contributions, like the capacitance of the extra deep or shallow p-well (C$_p$) located inside the n-well to form the PMOS transistors for the in-pixel electronic.

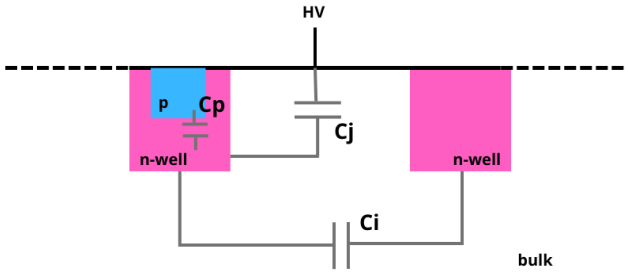

Figure 83.: Schematic cross-section of the capacitance contributions in an HV-MAPS. The total capacitance presented by a pixel to the front-end electronics includes several components: the inter-pixel capacitance (C_i), the junction capacitance (C_j) between the pixel electrodes and the capacitance of the extra deep or shallow p-well (C_p) located inside the n-well to form the PMOS transistors for the in-pixel electronic.

Proper capacitance estimation is crucial for suitable circuit analysis and design. The pixel capacitance can be affected by various factors, such as the size and geometry of the detector, the gap between the pixels, and the biasing voltage. This section discusses the different contributions to the total capacitance in a pixel detector.

5.4.1. Junction Capacitance

The capacitance of each pixel depends on its size, geometry, doping concentration, and bias voltages. Figure 84 shows a plot of the junction capacitance as a function of the pixel size (in one dimension) for different substrate resistivities and voltages. A linear fit was applied using the capacitance formula (equation 25). The thickness of the depletion layer for the fit was extracted from the TCAD simulations of the depletion zone. It is important to note that the capacitance values are given in fF/µm because of the 2D simulations. Hence to obtain the real pixel capacitance, the presented results must be multiplied by the pixel dimension in the transverse direction. The results show the expected behavior since high resistivity substrates (large depletion) and high voltages, which create larger depletion, result in lower capacitance values. In addition, the pixel size is proportional to the capacitance. As a result, pixels with large areas have worse signal-to-noise ratio and time resolution. The fit shows a good agreement with the TCAD simulated capacitance values except for the dataset at -120 V bias voltage and a resistivity of 200 Ω cm. For those conditions, full depletion was reached for the simulated detector thickness, and accordingly, the capacitance reached its saturation value.

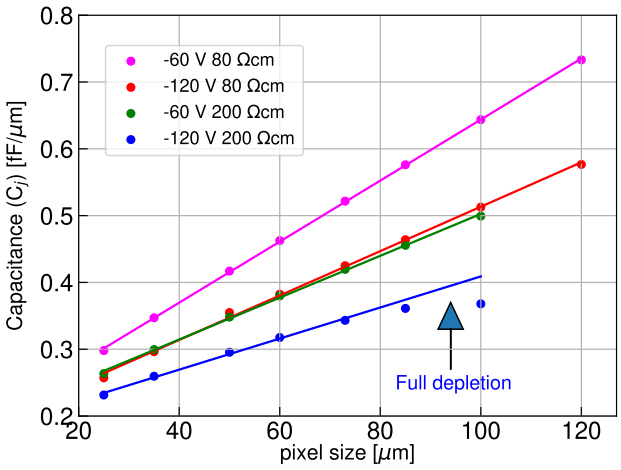

Figure 84.: TCAD simulated junction capacitance for a generic HV-MAPS as a function of the pixel size for different substrate resistivities and voltages. A linear fit was applied using the capacitance formula (equation 25).

5.4.2. Inter-pixel Capacitance

The inter-pixel capacitance depends on the distance between the pixels. After irradiation, when the interface traps increase, a higher accumulation layer increases the inter-pixel capacitance, and a higher noise rate is expected. Because of this, obtaining a general parametrization for the inter-pixel capacitance is difficult. Hence TCAD simulations are necessary to estimate these values for specific design isolations. Figure 85b shows the inter-pixel capacitance for different substrate resistivities and voltages as a function of the gap between pixels. The results are presented for an oxide charge concentration of $2\text{x}10^{11}$ cm^{-2} with a modied p-spray concentration technique with a concentration of $5\text{x}10^{16}$ (high concentration implant $1\text{x}10^{18}$ cm^{-3}). The simulation results show an inter-pixel capacitance lower than 1 fF due to pixel isolation. The curve behavior shows an inter-pixel capacitance increase for higher voltage and substrate resistivity due to an increase in the depletion zone and the signal induced in the neighbor pixels. Additionally, a small gap between the pixels increases crosstalk and the inter-pixel capacitance. The total inter-pixel capacitance also depends on the pixel size and is evaluated as the sum of four (parallel) capacitors, each one between the central pixel and one of the nearest four, plus the contribution of the four diagonal terms (Figure 85a). The length shared by the diagonal pixels is small compared with the parallel pixels and, accordingly, can be neglected. The contribution from the far-away pixels is also considered to be negligible.

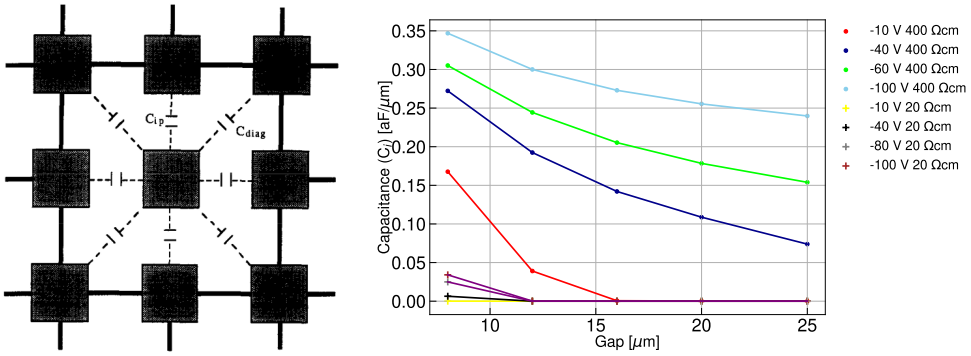

(a) Inter-pixel capacitance scketch **(b)** TCAD simulation Inter-pixel capacitance.

Figure 85.: Inter-pixel capacitance effect as a function of the gap between pixels with oxide charge of 2x10^{11} cm^{-2} with a modified p-spray technique with concentration 5x10^{16} (high concentration implant 1x10^{18} cm^{-3}). The lines are for visualization aid

5.4.3. Shallow p-well

In common pixel detectors, the inter-pixel capacitance has the principal contribution to the detector capacitance. However, with proper isolation in HV-MAPS, the inter-pixel capacitance can be neglected compared to the pixel junction and the capacitance from the small depletion created between the shallow or deep p-well and the collection electrode (n-well). Like the pixel junction, the behavior depends on the size and applied voltage. Figure 86 presents the TCAD simulation results for some of the typically applied voltages as a function of the p-well size. Tow voltages are scanned, the one from the n-well and the p-well. The voltage study shows that an increase in the operational voltage of both wells significantly impacts the decrease of the capacitance. Additionally, a decrease in the p-well reduces the pn-junction area and, as a result, the capacitance. The small depletion zones are responsible for the significant contribution from the shallow/deep p-well to the detector capacitance.

5.4.4. HV-MAPS capacitance

The capacitance values obtained for the TCAD simulated designs shown in Figure 87 using a substrate resistivity of 200 Ω cm at a bias voltage of -60 V are presented in Table 3. As previously shown, the inter-pixel capacitance is neglectable with proper isolation, and the junction and p-well have the highest contributions to the pixel capacitance.

These results show one more of the importance of a proper sensor design for

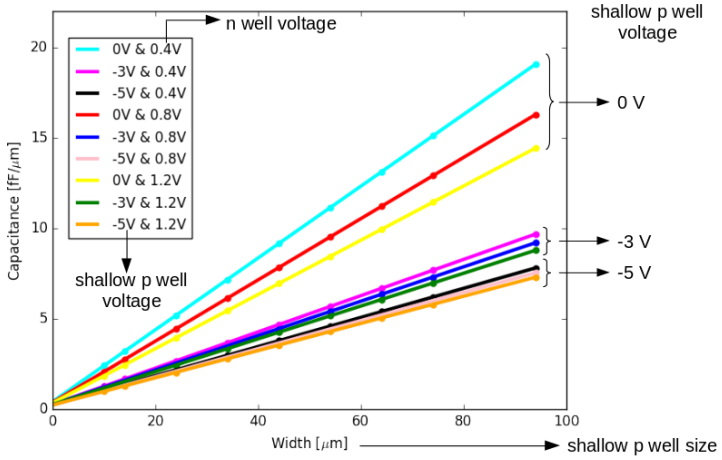

Figure 86.: P-well capacitance as a function of the p-well size for different voltages. The shallow p-well was considered to have a concentration of $1x10^{20}$ cm^{-3}.

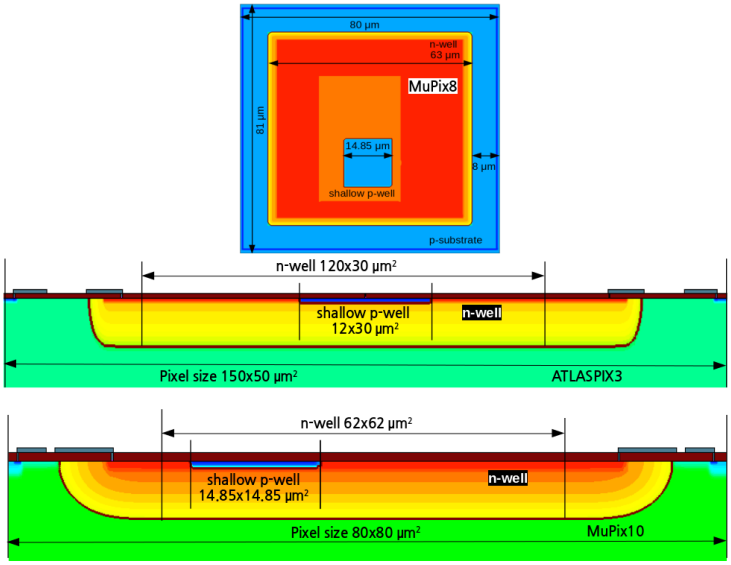

Figure 87.: SDE sketch (not to scale) of three simulated HV-MAPS prototypes: MuPIx8, ATLASPix3, and MuPix10.

specific applications. While a large pixel sensor creates more space for the pixel electronic and reduces the crosstalk between the connection lines, it also increases the pixel capacitance and consequently affects the time resolution. Additionally, higher substrate resistivities result in large depletions that reduce the capacitance but the lower electric fields cause slower collection times with the consequent deterioration of

Table 3.: TCAD simulated capacitance of HV-MAPS prototypes in a 200 Ω cm substrate at -60 V, with an oxide charge concentration of 2x10^{11} cm^{-2}. The modified p-spray technique was sued to isolate the pixels. For the shallow p-well, a 0 V was considered.

Sensor	C_j [fF]	C_i [fF]	C_p [fF]	C_{det} [fF]
MuPix8	36.0	< 1	59.4	95.4
MuPix10	36.4	< 1	59.4	95.8
ATLASPix3	60	< 1	90	150

the pixel efficiency and resolution, primarily in high rate applications.

Part III.

From TCAD Simulation to Experimental Data

Chapter 6

Testbeams Campaigns of HV-MAPS, Reconstruction and Analysis

Experimental evaluations known as testbeam (or beam tests) involve particle beams' used to assess particle detectors' characteristics, such as tracking resolution and hit reconstruction efficiency. These tests provide a unique opportunity to evaluate detector prototypes under real experiment-like conditions, which laboratory tests cannot replicate. Therefore, testbeams are an essential component of detector research and development.

For the R&D of HV-MAPS, several testbeam campaigns have been conducted at the DESY-II Test Beam Facility [55]. These campaigns aimed to evaluate the performance of different HV-MAPS prototypes. Some of the findings from these campaigns using the MuPix10 sensor are presented in this chapter.

6.1. The DESY-II Test Beam Facility

The DESY-II Test Beam Facility, as sketched in Figure 88, facilitates the provision of electron/positron beams within the GeV energy range. These beams are generated through a dual-conversion process utilizing the DESY-II electron beam. A carbon fiber target is initially inserted into the electron orbit to obtain bremsstrahlung photons. Subsequently, these photons traverse the extraction beam pipe and collide with a secondary target made of Cu or Al. Within the target, the photons undergo pair-production, converting into electrons and positrons. The particle type and momentum can be selectively chosen by manipulating the polarity and strength of the field in a dipole magnet. This process enables the achievement of particle momenta ranging from 1 to 6 GeV/c.

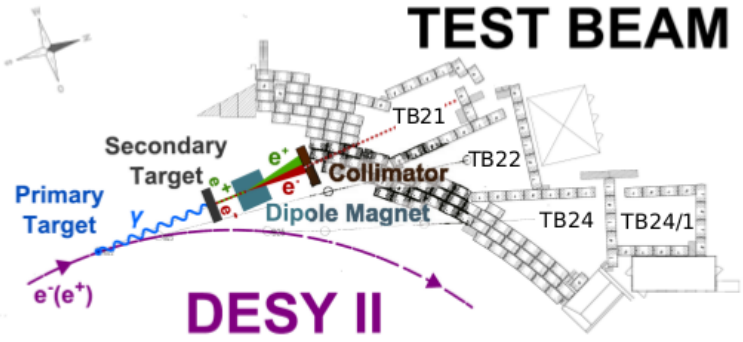

Figure 88.: Schematic of the DESY II test-beam facility with the testbeam areas TB21, TB22, TB24, and TB24/1.

To support the testbeam experiments, the testbeam facility comprises three distinct experimental areas. These areas have dedicated beamlines, comprehensive environmental monitoring instruments, and versatile, movable stages. A control hut connects each experimental area, enabling users to operate their instruments and oversee the experiments remotely. Additionally, a pixel telescope is provided in each experimental area to track the particles' trajectory precisely.

6.2. Beam Telescopes

During testbeam activities, evaluating the intrinsic resolution, tracking efficiency, and noise characteristics of the detector under examination is customary. It is crucial to employ an unbiased reference tracking system for comparison to ensure accurate measurements. This reference system, known as a beam telescope, typically employs pixel detector planes with high spatial resolution in the range of a few micrometers, offering well-established detection performance. The infrastructure supporting the beam telescope encompasses mechanical support, power supplies, and cooling systems (if needed) for the detector and trigger and data acquisition systems (TDAQ). The telescope planes are divided into two arms: upstream and downstream, depending on their placement in relation to the device under test (DUT), which refers to the evaluated detector system. The upstream arm consists of planes positioned before the DUT, while the downstream arm consists of planes located behind the DUT. By positioning the DUT between these two arms, it becomes possible to compare its particle detection performance against the reference tracks provided by the telescope. This arrangement allows for an effective assessment of the DUT's performance.

The most important parameter of a beam telescope is in the accuracy of the reconstructed tracks at the position of the device under test (DUT), commonly referred to as the pointing resolution. This resolution directly influences the measured resolution of the DUT and demands meticulous determination. The pointing resolution relies on two main factors: the intrinsic resolution of the telescope detector planes and the number of points obtained per track, corresponding to the number of telescope planes used.

Since the track positions are extrapolated, the telescope planes' geometric arrangement, or positioning, plays a crucial role in determining the track pointing resolution. To minimize uncertainty in the extrapolation of the track position, it is imperative to place the DUT as close as possible to its adjacent telescope planes. This close proximity ensures that the track extrapolation is more precise, improving the pointing resolution and subsequently obtaining reliable measurements of the DUT's resolution.

At DESY, there is one EUDET-type beam telescope [83] per experimental area. The EUDET-type beam telescope uses MIMOSA26 [84] sensors and has been a precise reference beam telescope for more than ten years. These telescopes are about to reach their end of life and need a successor. The ADENIUM (ALPIDE sensor-based DESY Next testbeam Instrument) [85] telescope is under study at DESY as a next-generation beam telescope. As the long-term availability of the MIMOSA26 sensors is not clear, the highly available ALPIDE [86] sensor is chosen for the ADENIUM telescope. It consists of six-pixel detector planes equipped with ALPIDE detectors, produced in a 180 nm CMOS Image Sensors (CIS) process and fabricated on p-type wafers with a 50 to 100 µm thickness, to reduce the impact of multiple Coulomb scattering, including a high resistivity 25 µm thick epitaxial layer. The sensors have an array of 512 × 1024 pixels with a pixel size of $26.88 \times 29.24\,\mu m^2$. Even though ALPIDE sensors have a slightly larger pitch, they offer a larger active area and significantly shorter readout times than the MIMOSA26 sensor.

The telescope planes are mounted in aluminum jigs with an opening for the beam, and 25 µm thick polyimide sheets protect the sensors. In contrast to the MIMOSA26 sensors, no active cooling is implemented as the overall heat dissipation of the sensor is relatively low.

The AIDA-2020 TLU [87] handles data synchronization on the hardware level by sending a global trigger signal, typically generated by a scintillator coincidence, to all connected detectors. Two sets of plastic scintillators provide triggering with light guides and Hamamatsu photomultiplier tubes. The scintillators are located before

the first and behind the last ALPIDE plane. Therefore, a fourfold coincidence of the scintillators' signal indicates that a particle traversed the entire telescope and is the most commonly used triggering scheme. Alongside the trigger signal, the AIDA TLU sends a trigger ID included in the telescope data stream. The synchronization gets more robust by including it in the DUT's data stream.

The TLU plays a crucial role in the testbeam setup by distributing the global clock and a global time reset and handling various trigger veto conditions, including busy signals. When a detector is being read out, it generates a busy signal indicating its unavailability to accept further triggers until the reading process is completed and the signal is pulled down. This process, known as "handshaking," ensures proper synchronization. The TLU manages and incorporates these busy signals into the trigger handling mechanism.

To accommodate the 2 µs peaking time of the ALPIDE sensor's analog circuits, a readout time of 10 µs is chosen to ensure that the hit corresponding to the trigger is successfully read out. It is possible to record multiple hits per trigger. However, since there is no on-chip time stamping provided, ambiguities may arise. One approach to resolve these ambiguities is to include an additional tracking plane consisting of a high spatial and time resolution detector. Alternatively, these ambiguous events can be addressed during the offline analysis stage.

The data acquisition system is responsible for reading out the telescope planes and the TLU is controlled by EUDAQ2 [88]. EUDAQ2 is specifically designed for beam tests and offers seamless integration with user-specific data acquisition systems like the MuPix-like DAQ. It provides global control and data streams to all detectors involved in the testbeam setup. Additionally, EUDAQ2 facilitates online monitoring functionalities and generates binary files containing the data streams collected from all participating detectors during the testbeam.

6.3. MuPix10 Testbeam Setup

The HV-MAPS group of Heidelberg University has carried out several testbeam campaigns at the DESY-II Test Beam Facility, including different setups such as the EUDET-type, ADENIUM, and MuPix telescope. The setup used through the campaigns presented in this thesis uses the ALPIDE telescope with different MuPix10 (thickness and resistivities) sensors as DUTs. The MuPix10 characteristics are introduced in 3.2.2. In addition, for studies of the cluster size, the DUTs were rotated using a rotation station provided by DESY, to obtain different beam incidence

angles. Figure 89 shows the basic setup employed, which comprises the ADENIUM telescope and the device under test. As mentioned, the DUT is placed between the two arms of the beam telescope, and the distance from its two adjacent planes is kept as short as possible.

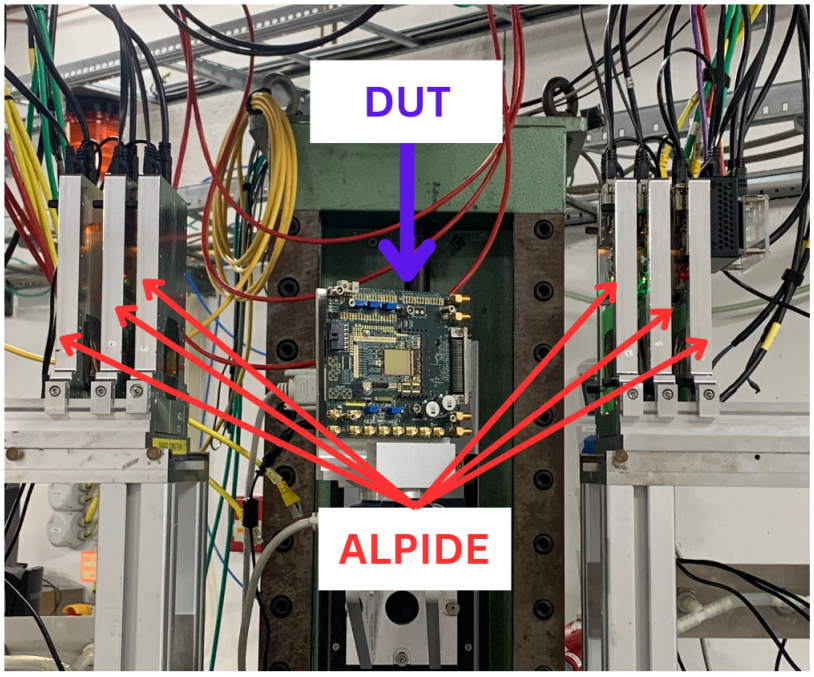

Figure 89.: Testbeam setup. The ALPIDE planes are highlighted in red, and the DUT is depicted in blue.

6.4. Data Taking

The Online Monitor from EUDAQ2 is employed to monitor the data's quality. The Online Monitor displays the data captured by each individual detector plane as well as the spatial and temporal correlations between data obtained from various planes. To monitor individual detector planes, their signal response, the number of triggered events, the number of channels fired, and the trigger rate are all checked. The correlation plots provide the first indication of data integrity by revealing whether the data is aligned in space and time.

Data is typically collected as part of various types of scans, including threshold scans. Additionally, scans are conducted at different beam incidence angles, with different bias voltages, or a combination of these factors.

6.5. Testbeam Reconstruction using Corryvreckan

The analysis of data obtained during the testbeam campaign can be divided into two primary steps. The first step is known as data reconstruction, which involves identifying detector hits from raw data, aligning all detector planes in the setup, and fitting (reconstructing) particle tracks. The identified hits and reconstructed tracks are then utilized in the second step, which involves analyzing detector performance.

The testbeam data reconstruction is achieved using the Corryvreckan [89] reconstruction software. Corryvreckan is a highly modular software designed explicitly for testbeam applications, which integrates the reconstruction and analysis phases into a single software package. Figure 90 illustrates a typical Corryvreckan reconstruction chain utilized for reconstructing and analyzing data from the MuPix10 testbeam.

6.5.1. Event Building

In the data reconstruction process, the initial step is the event definition, which is carried out using the `EventLoaderEUDAQ2` module. Upon detecting a coincidence between scintillator signals, the TLU generates a trigger signal with an accurate timestamp and trigger ID distributed to all detectors in the telescope. Subsequently, an event is constructed by matching all telescope data associated with the same trigger ID and centering the event time around the trigger timestamp. The ALPIDE readout chain sets the duration of the event.

The module `EventLoaderMuPix` integrates the DUT signal in the event. This module loops over all the hits in the DUT detector and matches the hits with a timestamp inside the event time window.

6.5.2. Clustering

The charges generated by one traversing ionizing particle may be collected in two or more adjacent pixels. Therefore adjacents pixels inside a defined time and distance window are grouped into clusters.

The clustering algorithm used for the MuPix10 sensors is the `Clustering4D`. This module combines direct neighbors (including pixel corners) if they lie within a time frame and a space range that depends on the sensor rotation. The cluster timestamp is defined by the earliest pixel within the cluster to mitigate the time spread from different drift times. The cluster center can be calculated as the arithmetic means or as the ToT-weighted center of gravity.

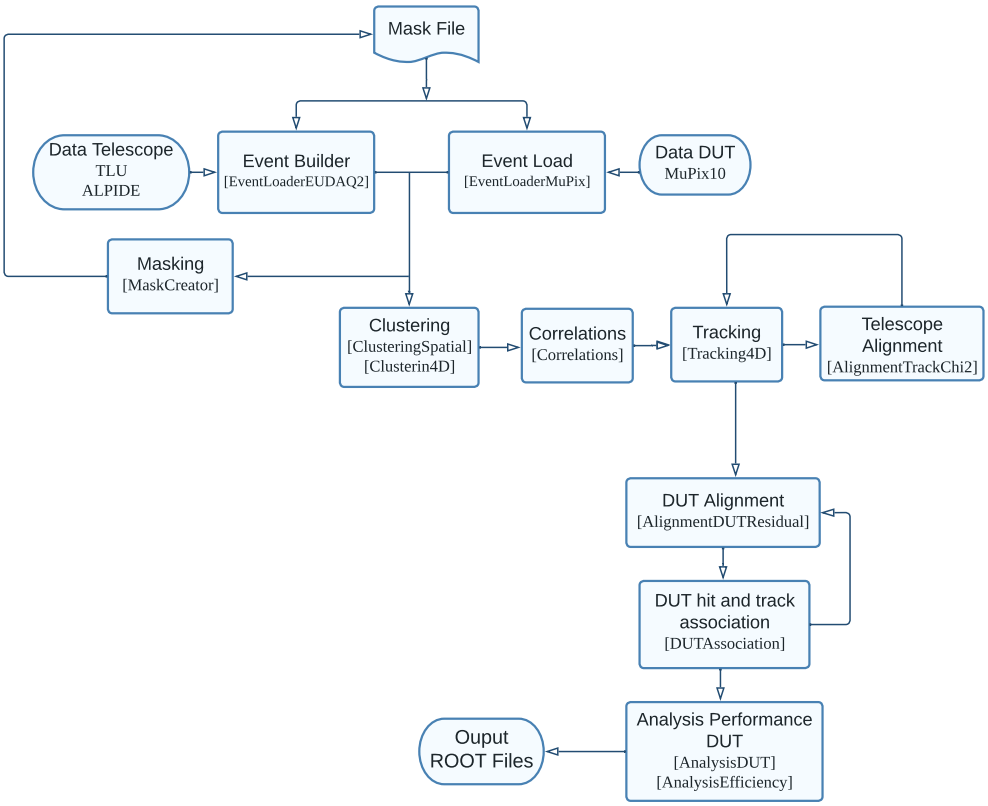

Figure 90.: Example of a reconstruction chain using the Corryvreckan framework. The main processes and the corresponding Corryvreckan modules are labeled.

The clustering algorithm only uses spatial information since no on-chip time stamping is provided for the ADENIUM telescope. The Corryvreckan module employed is the `ClusteringSpatial`. The timestamp assigned to the cluster is equal to the TLU trigger timestamp corresponding to the pixels in the cluster. The cluster center's coordinates are calculated as the arithmetic mean of all the pixels in the cluster since no ToT information is recorded.

Figure 91 shows an example of the cluster size distribution and a cluster hitmap for one of the ALPIDE layers. Figure 91a shows that the average cluster size is higher than 1 due to charge sharing. The regions in Figure 91b with no cluster hits are due to the use of a collimator of $2{\times}2$ cm^2, which is smaller than the ALPIDE sensor area. The distributions for the other ALPIDE planes are comparable during all the testbeam campaigns.

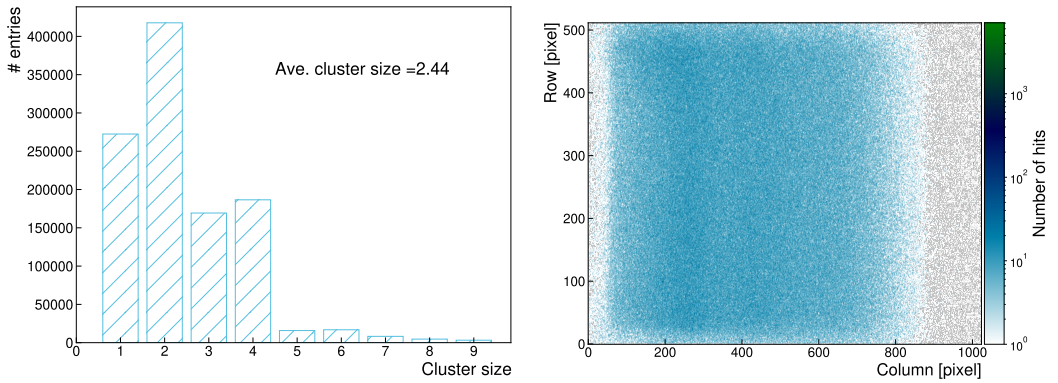

(a) Cluster size

(b) Cluster hit map

Figure 91.: Cluster characteristic of an ALPIDE detector plane from the ADENIUM telescope at DESY.

6.5.3. Masking of Noisy Channels

A mask is applied to remove noisy or hot pixels from the data to prevent the reconstruction of false tracks. The `MaskCreator` module in Corryvreckan generates a mask by storing the coordinates of the noisy pixels. This mask contains a list of all noisy pixels, which other modules in the reconstruction chain utilize to ignore the hot pixels. A simple frequency cut algorithm determines if a pixel is noisy. If a pixel fires more than the average number of hits on the sensor times a defined frequency cut, it is considered noisy and masked. The number of noisy pixels of the ADENIUM telescope was found to be between 0 and 5 pixels per layer. In the case of the MuPIx10 DUTs, the masking of noisy channels is usually done in extreme cases where noisy pixels overshadow the correlations, making it difficult to align the detector. For example, between 1 and 10 noisy pixels are masked for low thresholds study of the DUTs. However, the procedure is the same as for the telescope.

6.5.4. Correlations

A spatial correlation plot between two detector planes shows the difference in position between the hits on a detector plane taken as a reference and any other plane. The correlation plots are obtained using the `Correlation` module. In an ideally aligned setup with no magnetic field and negligible scattering, the correlation should follow a straight line with a slope of one and an intercept of zero, as the tracks are parallel. However, if the detector plane positions are displaced relative to each other, the intercept of the straight line corresponds to the physical offset in each direction.

Figure 92a shows a correlation between the first (reference) ALPIDE layer and the third, while Figure 92b shows a correlation between the same reference and a MuPix10 DUT. From the latest figure, it is clear that the setup of MuPix10 in the telescope follows a different configuration than the ALPIDE sensors, 180^0 around the y-axes and 90^0 around z-axes, with z-axes pointing in the beam direction (this configuration was chosen for the cabling and mechanical structure of the sensor). Also, the parallel line patterns to the column axes are due to noisy pixels in the DUT, and the lines parallel to the correlation are the result of crosstalk effect on the data lines of the MuPix10 (this effect is addressed in [90])

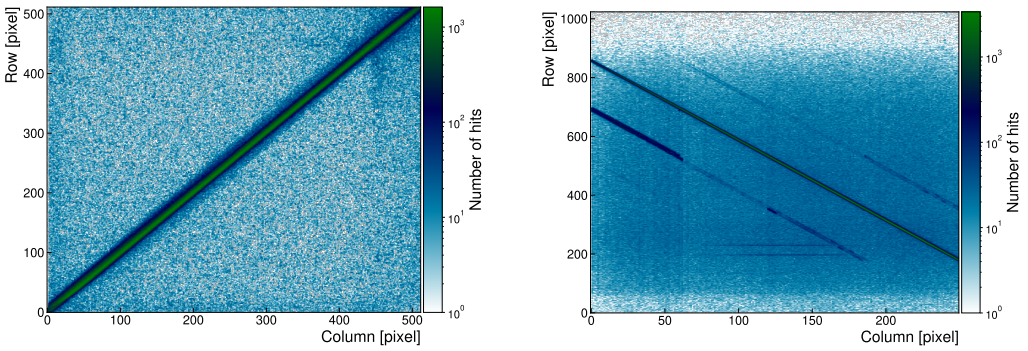

(a) Row-Row ALPIDE_0 and ALPIDE_2 **(b)** Row-Column ALPIDE_0 and MuPix10

Figure 92.: Spatial Correlation. The lines parallel to the Row-Column correlation (b) are the result of crosstalk effect on the data lines of the MuPix10 (this effect is addressed in [90])

6.5.5. Tracking

Tracking is the process of determining the trajectory of a particle in space, and a track is a mathematical object that represents this trajectory. Detectors are used to reconstruct tracks based on their hits. During testbeam, only reference telescope hits are used to avoid biasing the analysis of the DUT's properties. The `Tracking4D` module of Corryvreckan performs both track finding and track fitting. Track finding, also known as pattern recognition, combines clusters from the telescope planes to create track candidates. The process begins with identifying all combinations of clusters in the first and second telescope planes and connecting them with a straight line. The line is then extrapolated to the next detector plane, and clusters found within a search window defined by cuts are added to the track candidate collection if they belong to the same event. The line is then refitted, and the process is repeated for the other telescope planes.

The process of track fitting involves fitting a given track model to the positions of the clusters through a minimization of the track model's χ^2. Corryvreckan, in particular, employs two primary track models: the straight-line and the General Broken Lines (GBL) [91, 92].

The straight-line model is straightforward and is well-suited for high-energy heavy charged particles such as those used at the CERN Super Proton Synchrotron beam test facility. Conversely, the GBL model is more appropriate for low-momentum light particles at the testbeam, where multiple Coulomb scattering is expected. The GBL model accounts for multiple Coulomb scattering by allowing a kink angle at each detector plane involved in the fitting or a passive material along the particle's trajectory. A linear extrapolation is performed between two consecutive detector planes. Figure 93 shows both track models.

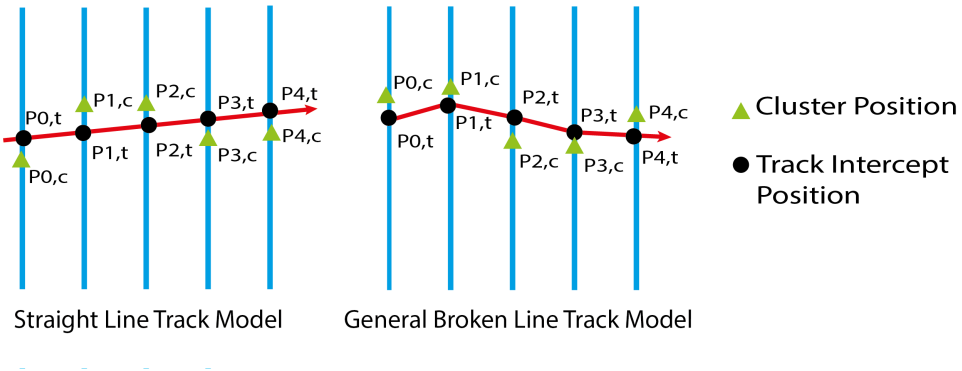

Figure 93.: Schematic representation of the straight line and general broken lines track models.

During beam tests at DESY, electrons and positrons with a maximum momentum of 6 GeV are utilized, and the impact of multiple Coulomb depends on the radiation length. Choosing the straight-line model can result in a decreased number of high-quality tracks, adversely affecting the overall track resolution at the DUT position and the precision of the performance analysis. Hence, the GBL model has been utilized for all the analyses discussed in Chapter 7.

As indicated before, for adding a cluster to a track, the candidate must be found within the given time of the event and inside an ellipse defined by two spatial cuts. The spatial cuts are chosen based on the telescope planes' intrinsic resolution (reported in [85] as $\sigma_x = 2.8$ ns for an optimal setup) and the correlation plots' width.

For instance, Figure 94a shows an example of spatial correlation plots between the reference and second plane of the telescope. To add a cluster to the track candidate,

a cut of ±140 µm in X and Y and ±20 μs are set. It should be pointed out that the spatial cuts are used after the alignment of the planes is completed. During the alignment procedure, the cuts are relatively large and are reduced to the values containing the entire width of the correlation distributions of the planes. The time cut is chosen in order to cover the extent of an entire event because the ALPIDE hits may stem from any time within the given event derived from the trigger timestamp, as previously discussed.

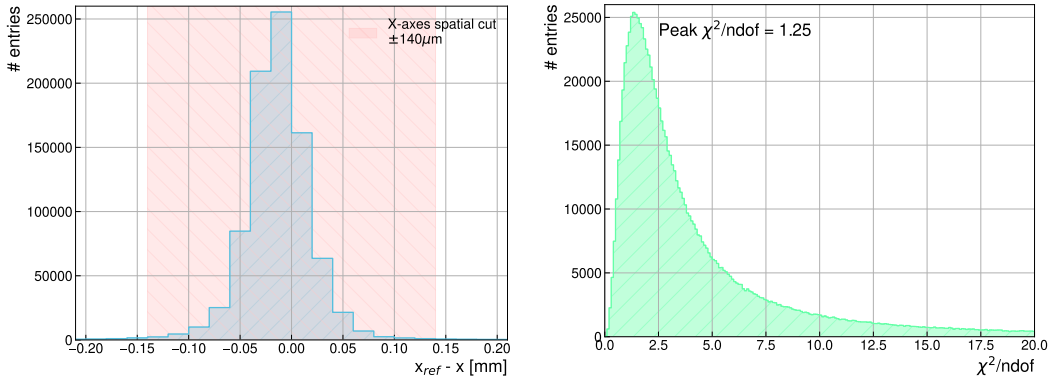

(a) Spacial correlation in x between the reference and ALPIDE_1.

(b) χ^2 distribution of the reconstructed tracks in the ADENIUM-type telescope.

Figure 94.: Track selection and quality plots.

The quality of the fitted track is evaluated using the χ^2 distribution, with Figure 94b displaying the $\chi^2/ndof$ distribution of the reconstructed tracks, with $ndof$ denoting the number of degrees of freedom of the fit. The distribution peaks at $\chi^2/ndof \approx 1.0$, implying that most of the fits and their corresponding reconstructed tracks have good quality. An increase in the spatial cut leads to a slight increase in the total number of reconstructed tracks. However, most of the additional tracks have a large $\chi^2/ndof$ and would thus be excluded from the further analysis for which only tracks with $\chi^2/ndof \leq 3.0$ are accepted to ensure good statistics while keeping only high-quality tracks.

6.5.6. Telescope Track-Based Alignment

If the geometry of the measurement setup is not accurately known, a precise evaluation of detector performance can't be achieved. The properties of all tracks are highly reliant on the geometrical configuration of the measurement setup. While laser systems can be used to align detector layers, this method is not sufficiently precise. Laser alignment is cumbersome even for a few detector planes because it involves

physically moving the detector planes. Furthermore, sensor positions are imprecise as they are either enclosed in protective boxes or held in holders. On the other hand, track-based alignment offers submicrometer accuracy and does not require any movement of detector planes, saving time and minimizing the risk of physical damage. The alignment problem arises due to imprecise knowledge of the setup geometry, necessitating the assumption of initial detector positions, rotations, and sensor bow.

To align the telescope planes, the track-based method involves iteratively adjusting the positions (X and Y) and rotations (around the x-, y- and z-axes) of all planes with respect to a reference plane using the module `AlignmentTrackChi2`. This is done by refitting tracks to minimize the sum of all track χ^2 values using Minuit2 [93]. The alignment process is continued until convergence, which is achieved when no further improvements in the biased residuals of the telescope planes are observed, and the $\chi^2/ndof$ shows a peak at 1.0. The residual is a difference between the intercept of the extrapolated track with the detector plane and the associated hit measured by this detector. Figure 95 shows the telescope residuals after alignment.

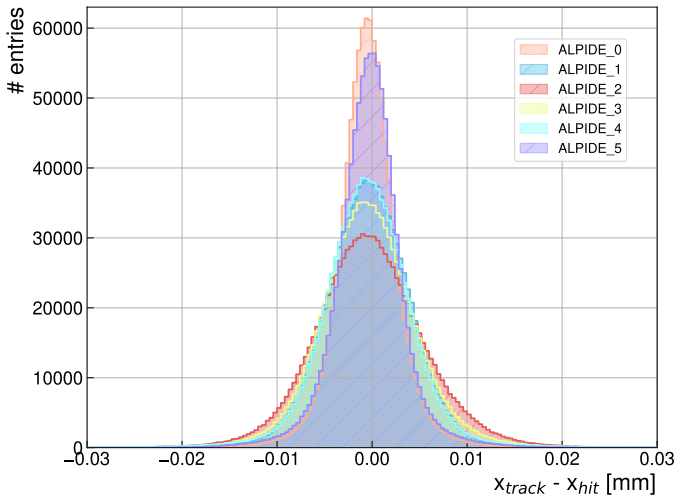

Figure 95.: Telescope residuals after alignment.

6.5.7. Track-DUT Hit Association

As mentioned, the DUT clusters are excluded from the track candidates to prevent bias in evaluating their performance. Thus, a separate step is required to associate these clusters with one of the reference tracks. The association procedure involves determining the intersection point of the track with the DUT, and subsequently, all clusters within a defined spatial and time range are associated. To determine whether

a cluster is within the range, the distance between the track intercept and either the cluster's center or the center of the closest pixel to the track intercept in the cluster is compared. The latter method is preferred as it reduces the impact of delta electrons, which can cause large clusters whose centers are displaced away from the track incidence point. The effect of delta electrons is a well-known phenomenon and has been extensively researched, as shown in [94]. Association cuts are determined following the same criteria as for the track finding and depend strongly on the DUT rotation. The time interval was chosen based on the width of the time correlation plots, as shown in Figure 96. The displacement of the curve peak from zero is due to a 157 ns delay. Also, the visible tale in the curve is the product of the time walk discussed in section 3.2.2

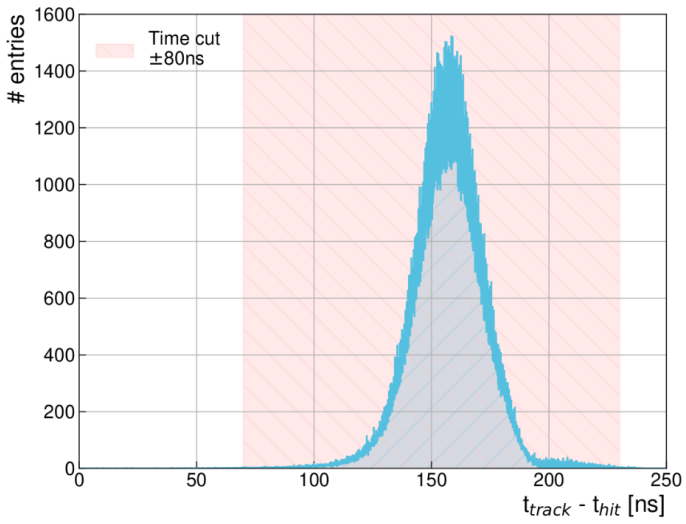

Figure 96.: Time residual distribution for MuPix10

6.5.8. Track-Based DUT Alignment

The alignment procedure for the DUT is similar to that of the telescope. The alignment is carried out using the `AlignmentDUTResiduals` module, which minimizes the RMS value of the spatial residual distribution of the DUT by varying its positions and rotations. Figure 97 shows an example of a residual distribution after alignment for one of the tested MuPix10 sensors. After alignment, the residual is centered around zero, and the tails are about one order of magnitude smaller because alignment reduces the number of uncorrelated and noise hits. The unbiased residual distributions allow for an estimation of the DUT's position resolution and are the first figure of merit to examine during a beam test analysis.

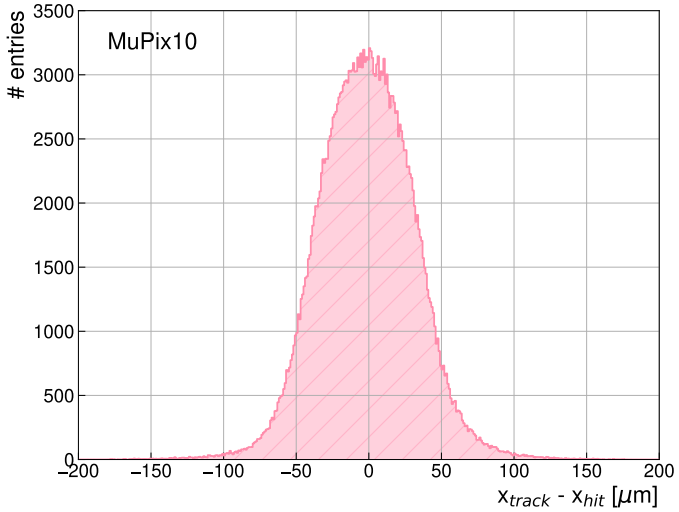

Figure 97.: Spacial residual distribution for MuPix10 after aligment.

6.6. Chip Characterization parameters

6.6.1. Hit Reconstruction Efficiency

The testbeam evaluates the hit reconstruction efficiency as one of the most important parameters for a given threshold. The efficiency corresponds to the probability of detecting a particle passing through the detector and is obtained as the ratio of the number of tracks with an associated cluster in the DUT and the total number of reconstructed tracks passing through the DUT detection area, known as reference tracks. Equation 37 defines the efficiency, where k is the number of tracks with an associated cluster in the DUT and N is the total number of reference tracks.

$$\epsilon = \frac{k}{N}, \tag{37}$$

6.6.2. Spatial Resolution

The accuracy of the reconstructed hit location is constrained by the pixel's finite size (known as pitch) and the inherent statistical fluctuations during charge deposition and collection. As a result, the reconstructed position on the DUT is always displaced relative to the track position. The difference between the position of the track intercept and the center of the associated cluster, $x_{track} - x_{hit}$, is called the unbiased residual, and the RMS of its distribution, defined in Equation 38, is employed to

estimate the DUT spatial resolution $\sigma_x(DUT)$.

$$RMS_x = \sqrt{\frac{1}{N}\sum_{i=1}^{entries}(x_i - x_{mean})^2} \tag{38}$$

Equation 34 defines the spatial resolution achievable through binary readout for a single pixel cluster. Assuming an infinitely precise track-pointing resolution, the unbiased residuals would produce a box-shaped distribution, with a width equivalent to the pixel pitch. However, the box edges become blurred due to the finite track-pointing resolution of a real telescope. To account for this effect, the telescope resolution can be modeled as a Gaussian normal distribution, and a convolution of a box function with a Gaussian can be used to describe the width of the unbiased residuals. Additionally, the shape of the residual may be influenced by the occurrence of multi-pixel clusters, particularly at the corners and edges of a pixel, resulting in a bias towards small residuals for these clusters. The result in an achievable spatial resolution directly correlated with its clustering behavior, which is analyzed in Chapter 7. In the case of a normal distribution, the RMS is identical to the standard deviation of the Gaussian.

It's crucial to note that the total width of the unbiased residuals is a convolution of two factors: the DUT's intrinsic resolution and the reference telescope's resolution. Assuming a Gaussian residual distribution, the telescope resolution can be subtracted in quadrature as:

$$\sigma_{DUT} = \sqrt{\sigma^2_{measured} - \sigma^2_{telescope}} \tag{39}$$

When the resolution of the telescope is much smaller than the one of the DUT, $\sigma_{telescope} \ll \sigma_{DUT}$, the influence of the telescope can be neglected, and equation 39 becomes

$$\sigma_{DUT} \approx \sigma_{measured} \tag{40}$$

6.6.3. Time Resolution

Similar to spatial resolution, time resolution can be estimated from the width of unbiased time residuals between the reference track and the associated cluster on the DUT.

$$t_{residual} = t_{\text{track intercept}} - t_{\text{associated cluster}} \tag{41}$$

In general, achieving improved time resolutions can be attributed to either a substantial increase in the signal or a decrease in the detection threshold. This alteration results in a sharper threshold crossing, diminishing the comparator jitter susceptibility. In other words, it minimizes the impact of time fluctuations caused by noise variations in the signal, which inevitably contribute to the overall time resolution. One should note that the time residual might exhibit an asymmetric distribution due to timewalk, as elaborated in Section 3.2.2.

Chapter 7

Test Beam Measurements

This chapter presents the measurement and analysis results from testbeam campaigns using three MuPix10 sensors with different thicknesses and resistivities. These studies investigate the in-pixel hit detection efficiency, cluster size, and spatial and time resolution under different thresholds and voltage conditions. The sensor settings used for all the measurements presented in this thesis are listed in Appendix C.

In many applications, particles may not enter the sensor perpendicular to its surface, and studying its performance at different incident angles can help determine its capabilities, limitations, and suitability for various applications. Therefore the sensor's performance in detecting particles that enter at different angles is also presented.

7.1. Hit Detection Efficiency

The hit detection efficiency is defined as the probability of detecting a traversing ionizing particle as described in subsection 6.6.1.

7.1.1. Threshold dependence

The efficiency is studied during the testbeam as a function of the threshold set in the discriminators. Scanning the discriminator threshold and obtaining the efficiency for each step leads to the so-called "s-curve". The efficiency s-curve can be fitted with an empirical skewed complementary error function [95].

Figure 98 shows the hit detection efficiency for a MuPix10 sensor thinned to 100 µm with a 200-400 Ω cm substrate resistivity at three different voltages as a function of the threshold. Higher voltages exhibit a broader threshold range, approximately 130 mV

wide, with efficiency above 99%. For higher thresholds, the efficiency decreases appreciably. This behavior is expected, and it is caused by the fact that, with the increase of the threshold, only events with large charge depositions lead to hits, and according to the Landau distribution of the deposited charge, the fraction of such events is small. The same trend is observed as the voltage decreases, and the threshold range for which the efficiency remains above 99% is significantly reduced compared to the high voltages. The range shrinks to approximately 30 mV for a bias voltage of -20V, as seen from the inset in Figure 98. This reduction corresponds to a decrease in the sensor's performance and is a direct consequence of the decrease in the width of the depletion region.

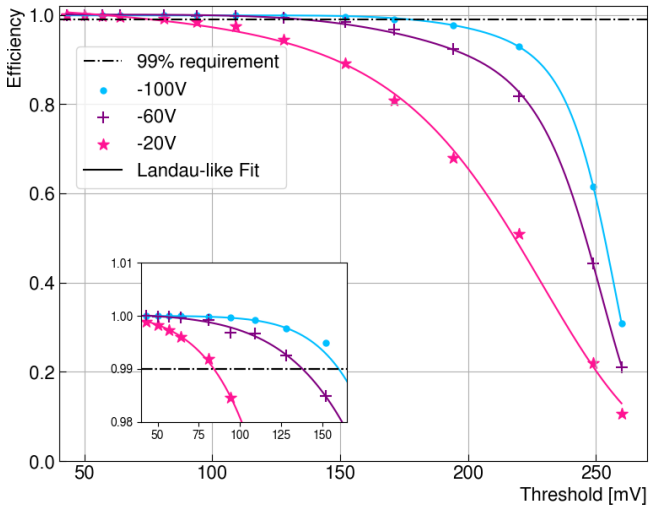

Figure 98.: Efficiency as a function of the threshold for different bias voltages for a MuPix10 sensor thinned to 100 µm.

The charge deposited in the undepleted volume is collected via diffusion, as no electric field is present. Thus, charges move slower, with a low contribution to the electrodes' collected charge within the detector's total integration time. In addition, the slower movement also increases the recombination probability.

7.1.2. Efficiency uniformity

The in-pixel efficiency is studied by combining the in-pixel efficiency results of all the pixels inside the region of interest (ROI). The sensor must have a uniform performance to properly study the in-pixel effects because the threshold setting is

applied globally to the entire matrix. An inhomogeneous response will lead to areas of lower hit detection efficiency, affecting the resulting in-pixel efficiency distribution.

Figure 99 shows efficiency maps for different thresholds and voltages. The color scale represents the efficiency for a set column/row and threshold; the x-axes represent the column/row number, and the y-axes the applied threshold. The results show that the response across all the columns and rows shows good uniformity over the entire studied threshold range.

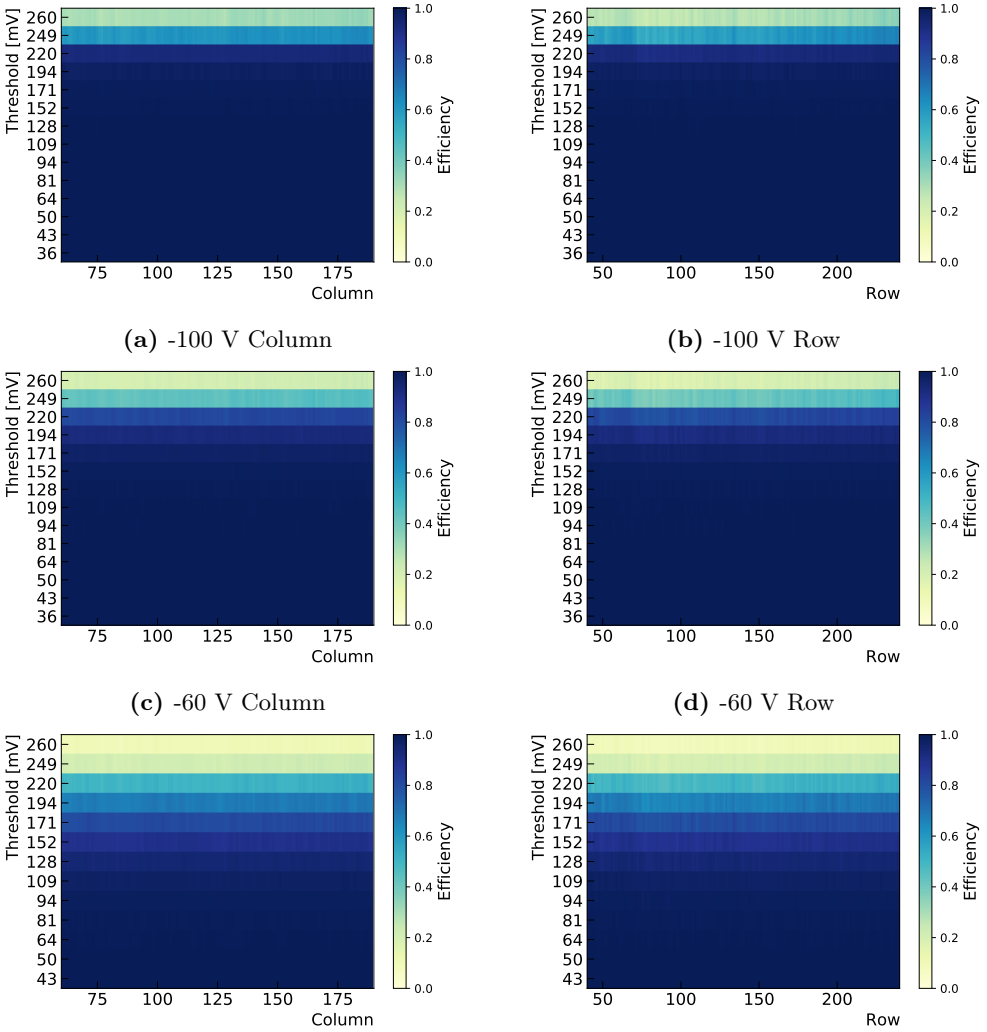

(a) -100 V Column **(b)** -100 V Row

(c) -60 V Column **(d)** -60 V Row

(e) -20 V Column **(f)** -20 V Row

Figure 99.: Column and Row dependence of the hit detection efficiency for different thresholds and bias voltages.

Figure 100 shows a schematic of an ALPIDE telescope plane and the MuPix10 sensor. The ALPIDE is larger than the DUT in the horizontal direction. However, in the vertical direction, MuPix10 extends from the telescope. Consequently, the entire MuPix10 chip can not be characterized in a single run, and the data used for the analysis is restricted to the overlapping region and further reduced to an ROI.

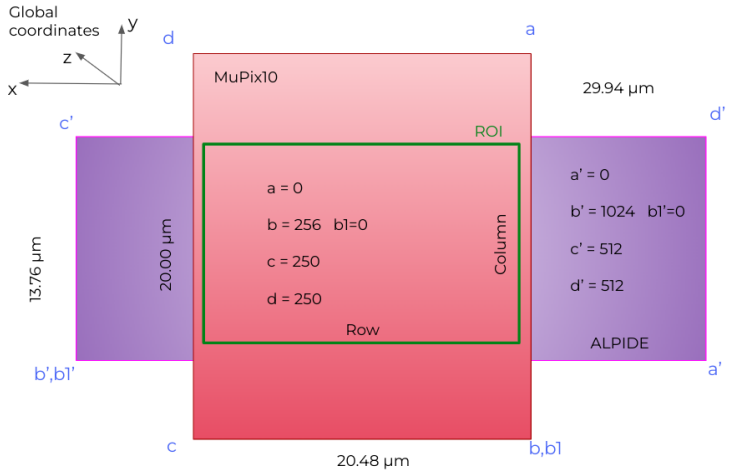

Figure 100.: Schematic showing the telescope coverage of the DUT (MuPix10) and the ROI. The global coordinate system used through all the following analyses is defined.

7.1.3. In-Pixel Efficiency

The in-pixel efficiency for different thresholds in a MuPix10 sensor biased to -100 V is shown in Figure 101. The efficiency remains above 99% for low thresholds, and no spatial dependency within the pixel is observed. For higher thresholds, the efficiency is the highest within the pixel center and decreases towards the edges and corners. A shift of the highest efficiency from the pixel center along the x-direction is observed due to a small rotation about the y-axes during data taking (section 7.7.1 presents the effect of rotation over the in-pixel efficiency). The low efficiency at the corners and edges is expected, given that the charge created by one traversing particle due to lateral diffusion may be collected in two or more adjacent pixels (Figure 102). This effect is called charge sharing. More charge sharing occurs near the corners and edges, leading to larger clusters. In the pixel edge, the charge sharing occurs between two pixels; in the corners, the charge can be shared by up to four pixels. Therefore, the collected charge in one pixel shrinks and likely remains below the threshold.

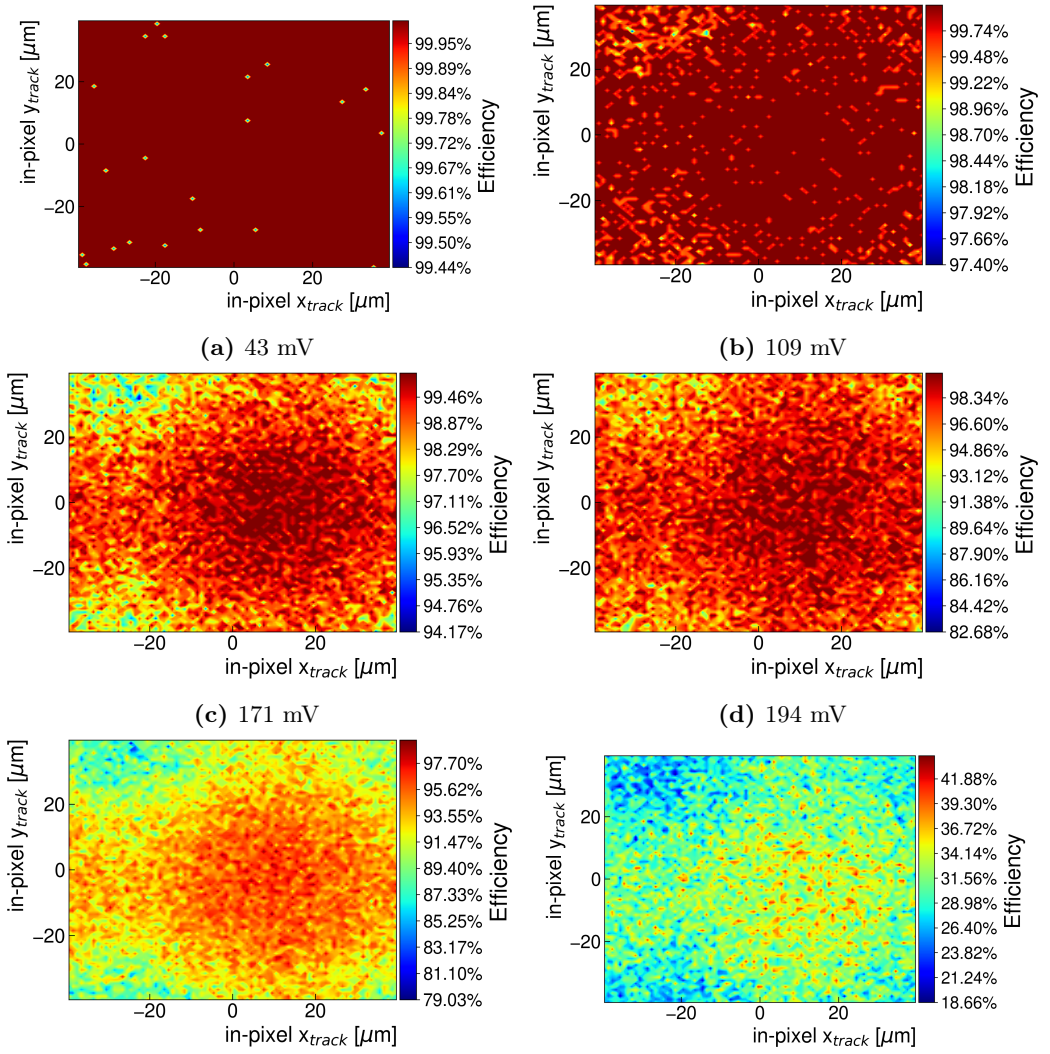

(a) 43 mV **(b)** 109 mV

(c) 171 mV **(d)** 194 mV

(e) 220 mV **(f)** 260 mV

Figure 101.: In-pixel efficiency at different thresholds for a MuPix10 sensor thinned to 100 µm and biased to -100 V.

Figure 103 compares the in-pixel efficiency for different voltages and thresholds. Low voltages have a smaller depletion zone and, as a result, lower efficiencies. The plots show that the efficiency drops at the corners and edges for all the voltages due to increasing charge sharing and lower depletion zones. For high thresholds, the efficiency is also affected for particles passing close to the center of the pixel. It is important to note that the rotation observed for the measurement at -100 V was corrected for lower voltages during the data taking.

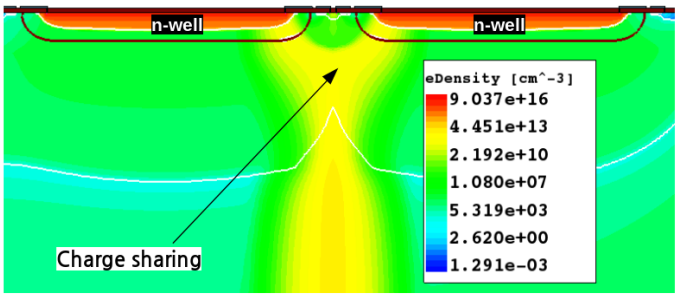

Figure 102.: Electron density distribution using TCAD simulation when a particle passes through the center of the gap between two pixels.

The collected charge when a particle traverses the center of the pixel and the gap was evaluated using TCAD simulations and is presented in Figure 104. The TCAD simulations results show a decrease up to ∼50% of the collected charge by one pixel within 5 ns when particles pass through the center of the gap. These results agree with the efficiency reduction at edges and corners due to charge sharing.

7.2. Cluster size

Because of charge sharing, a clustering algorithm is needed to group pixels related to one particle into a cluster. If a pixel hit timestamp is available, adjacent pixel hits can be combined into a cluster if they coincide within a specific time window. If no time information is available, the clustering is performed solely based on the hit positions. Figure 105 shows the normalized distribution of cluster sizes at -100 V and a 43 mV threshold. Single-pixel clusters make up the largest fraction, with ∼90.7%. In ∼8.5% of all cases, two-pixel clusters occur, and for ∼0.8%, the cluster size is ≥ 3.

7.2.1. Threshold dependence

Figure 106 shows the mean cluster size as a function of the threshold. The mean cluster size is close to one and decreases with increasing thresholds reaching a minimum at a threshold ∼230 mV. The decrease in the mean cluster size follows the expectation since, for a given charge sharing, the probability of the signal crossing the threshold decreases for a high threshold. For even higher thresholds, the cluster size increases. The increase can be attributed to a bias toward large energy depositions like delta rays. No notable difference is seen between the column and row cluster size width.

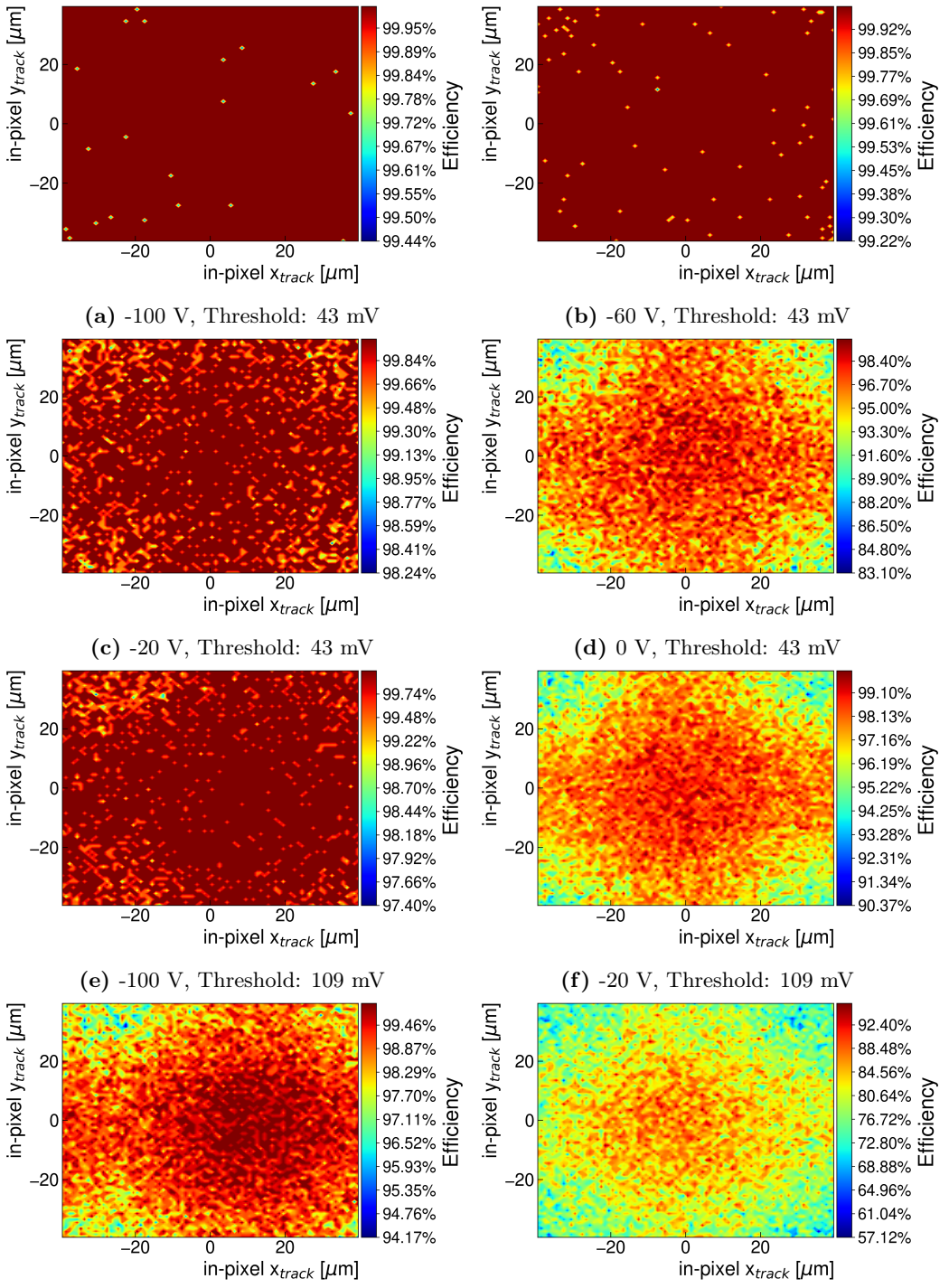

(a) -100 V, Threshold: 43 mV

(b) -60 V, Threshold: 43 mV

(c) -20 V, Threshold: 43 mV

(d) 0 V, Threshold: 43 mV

(e) -100 V, Threshold: 109 mV

(f) -20 V, Threshold: 109 mV

(g) -100 V, Threshold: 171 mV

(h) -20 V, Threshold: 171 mV

Figure 103.: In-pixel efficiency for a MuPix10 sensor thinned to 100 µm for different thresholds and voltages.

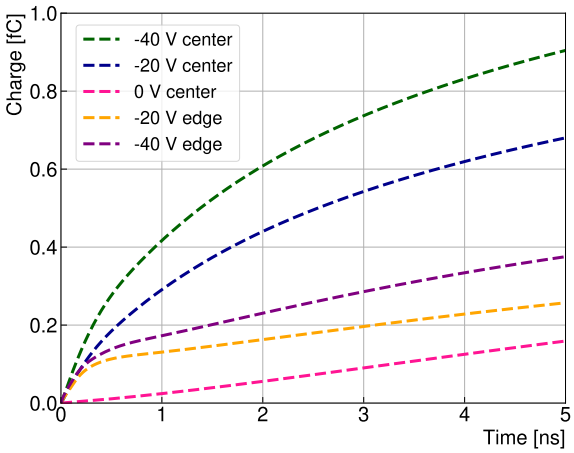

Figure 104.: Accumulated charge from a MIP during 5 ns for different bias voltages and in-pixel positions obtained from TCAD simulations in a MuPix10 sensor thinned to 100 µm.

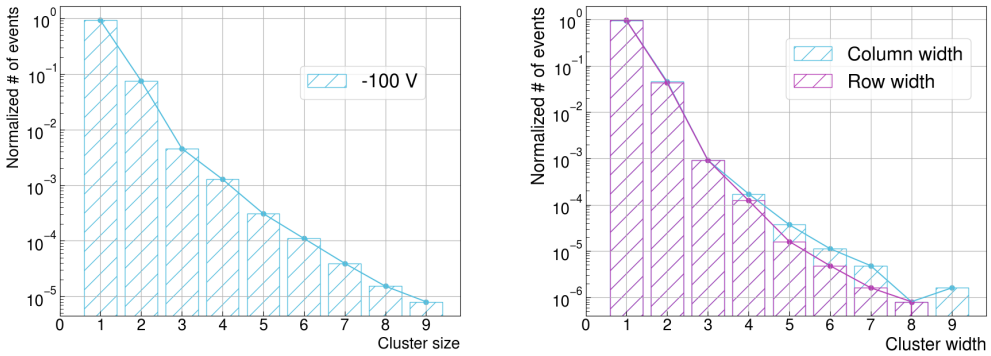

(a) Cluster size

(b) Cluster width in column and row direction.

Figure 105.: Normalized distribution of cluster size and cluster width for a MuPix10 sensor at -100 V and a 43 mV threshold.

7.2.2. In-pixel cluster size

The mean cluster size as a function of the track intercept within the pixel, refers in the following as in-pixel cluster size, offers evidence of the increased charge sharing for tracks closer to the pixel edge. Figure 107 displays the 2D mean cluster size distribution for different voltages and thresholds. For all the cases, the mean cluster size increases when the particles traverse close to the pixel edge and corners, as

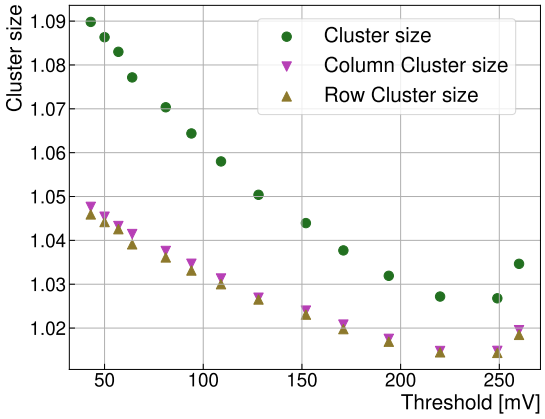

Figure 106.: Mean cluster size as a function of the threshold for a MuPix10 sensor thinned to 100 µm with a substrate resistivity and a -100 V voltage.

previously concluded from the in-pixel efficiency plots. This behavior depends on the threshold and voltage, which modulates at which distance from the pixel center the charge sharing is high enough to generate hits with cluster sizes larger than one.

The mean cluster size as a function of the in-pixel position in the y-axis is presented in Figure 108a for different voltages and thresholds. For low thresholds, particles passing throughout the center of the pixel produce hits with larger cluster sizes as the voltage decrease. This behavior is due to the larger diffusion in the undepleted areas. Less charge is collected via drift for very low voltages, and the probability of crossing the threshold decreases. As a result, the increased diffusion is not registered and the mean cluster size increases. For large thresholds, as shown in Figure 108b, particles passing by the center of the pixel result in a larger cluster size for the highest voltage since only hits with large signals are registered. Figure 109 compares the in-pixel efficiency and mean cluster size for different voltages. As previously concluded, a large cluster size due to increased charge sharing results in lower efficiencies.

Even if an increased cluster size at the pixel edge is responsible for the efficiency decrease, the mean cluster size is ∼1 for all the in-pixel positions. HV-MAPS complex electric field distribution results mainly in hits with cluster size one. Figure 110 shows the TCAD simulation results of the charge collected in a hit pixel and its neighbor for different in-pixel track positions. This result shows a charge induced in the neighbor pixel lower than 70% of the charge collected in the hit pixel for particles passing from the pixel center up to 5 µm from the pixel corner.

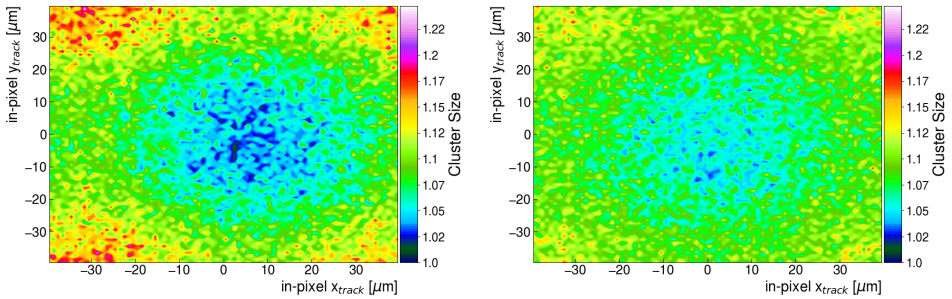

(a) -100 V, Threshold: 43 mV

(b) -60 V, Threshold: 43 mV

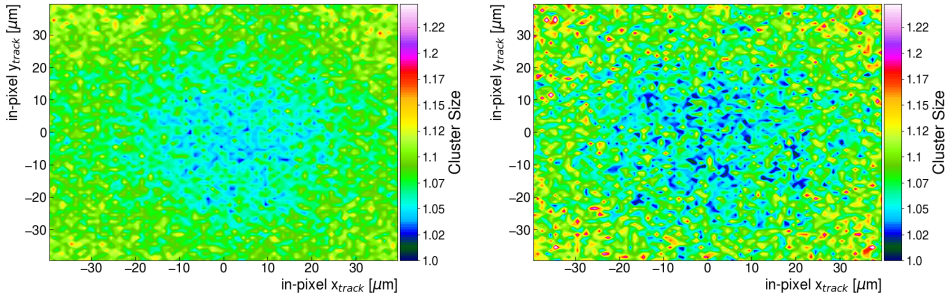

(c) -20 V, Threshold: 43 mV

(d) 0 V, Threshold: 43 mV

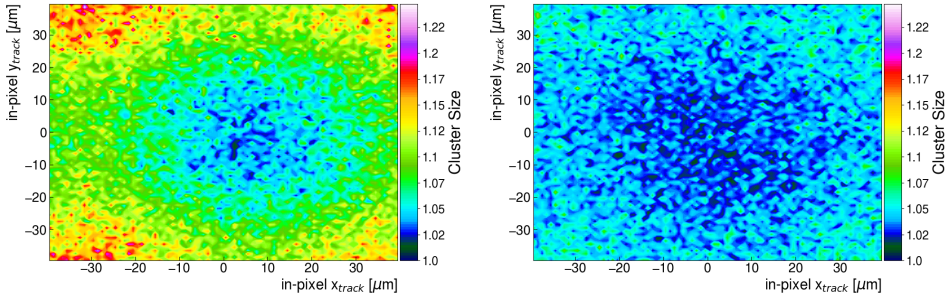

(e) -100 V, Threshold: 109 mV

(f) -20 V, Threshold: 109 mV

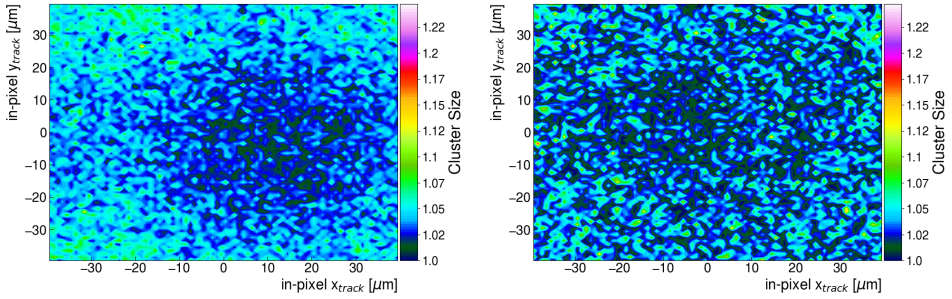

(g) -100 V, Threshold: 171 mV

(h) -20 V, Threshold: 171 mV

Figure 107.: Mean cluster size as a function of the track intercept for a MuPix10 sensor thinned to 100 µm for different thresholds and voltages.

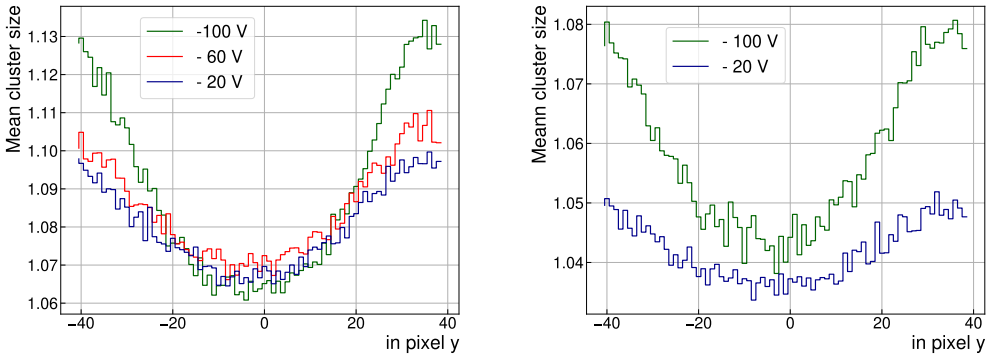

(a) Threshold: 43 mV **(b)** Threshold: 109 mV

Figure 108.: Mean cluster size along the y-axis as a function of the track intercept for different voltages for a MuPix10 sensor thinned to 100 µm.

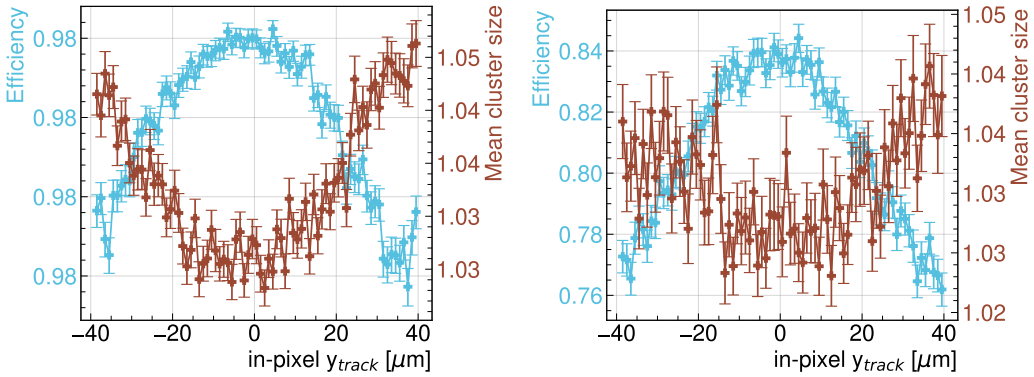

(a) -100 V. **(b)** -20 V.

Figure 109.: Mean cluster size and efficiency along the y-axis for different voltages at a 171 mV threshold for a MuPix10 sensor thinned to 100 µm.

Figure 111 shows the electron density for tracks with four different in-pixel positions. Both results indicate that particles passing 5 µm away or more from the pixel edge drift mainly to the hit pixel, and only a low signal is registered in the neighbor pixel. This behavior caused the observed mean cluster size ∼1, even for particles close to the pixel edge.

7.3. Spatial resolution

As discussed in subsection 6.6.2, the spatial resolution can be quantified as the RMS value of the unbiased spatial residual distributions (difference between the interpolated track intercept on the DUT sensor and its measured position).

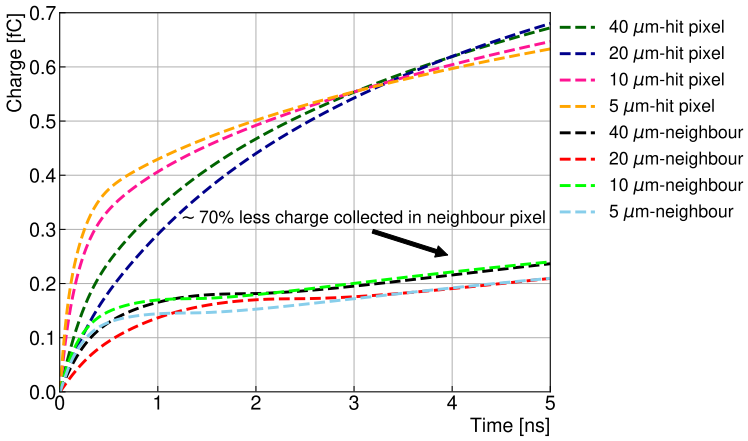

Figure 110.: TCAD simulation of the accumulated charge from a MIP with different entry points distances from the sensor edge in a MuPix10 pixel structure thinned to 100 µm with a -20 V applied voltage.

7.3.1. Threshold dependence

Figure 112a shows the normalized spatial residuals along the y-axes at a bias voltage of −20 and -100 V for a 43 mV threshold. The cluster positions were ToT-weighted for n pixels within the cluster, as follows:

$$y_{cluster} = \frac{\sum_{i=1}^{n} ToT_i * y_i}{\sum_{i=1}^{n} ToT_i} \tag{42}$$

The shape of these distributions and the position resolution depends on several factors, including the sensor pitch and experimental conditions, like the particle incidence angle and the operating threshold and voltage. For the sensor bias at -100 V, the increased charge sharing near the pixel edge results in an improved spatial resolution compared with the biased at -20 V.

Figure 112b shows the RMS distribution as a function of the threshold. It can be seen that the RMS increases with an increasing threshold. This behavior is expected because, with an increasing threshold, the number of multi-pixel clusters is reduced and the cluster position will move further from the real track position. After a maximum, the RMS fall-off results from an efficiency reduction, with only particles passing by the center of the pixel collecting enough charge to pass the threshold. The RMS increase again for a very large threshold since mostly particles with large energy depositions and large clusters are recorded.

The spatial resolution behavior can be better understood when the different

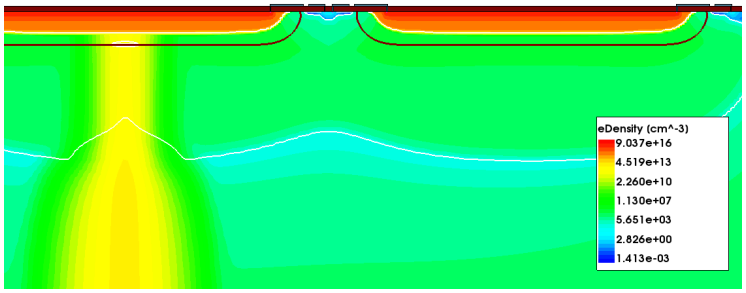

(a) 40 µm

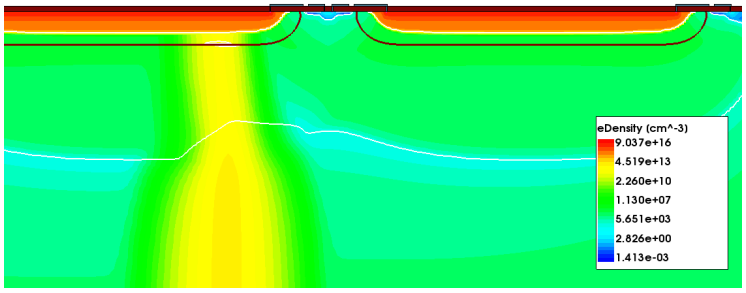

(b) 20 µm

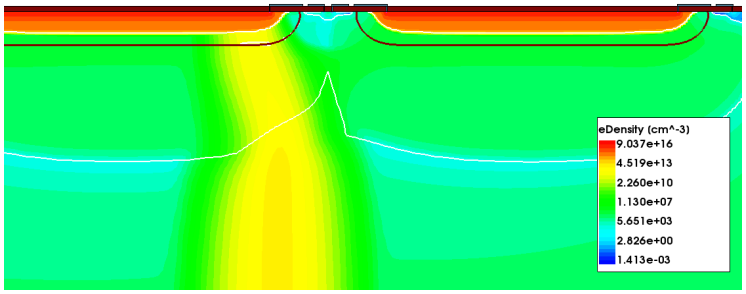

(c) 10 µm

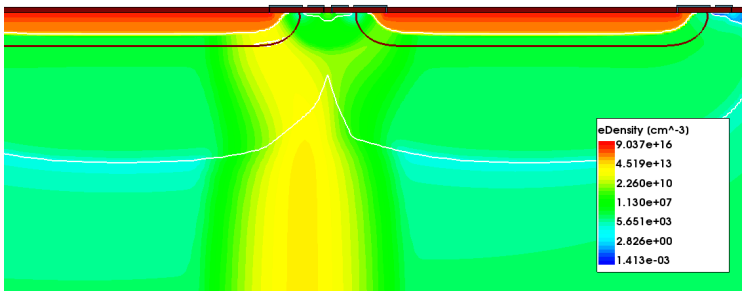

(d) 5 µm

Figure 111.: TCAD simulation of electron density from a track with different in-pixel positions in a MuPix10 sensor with a -20 V applied voltage.

cluster size contributions are investigated. Figure 113 displays the normalized spatial residuals for different cluster sizes at different thresholds and bias voltages. Since

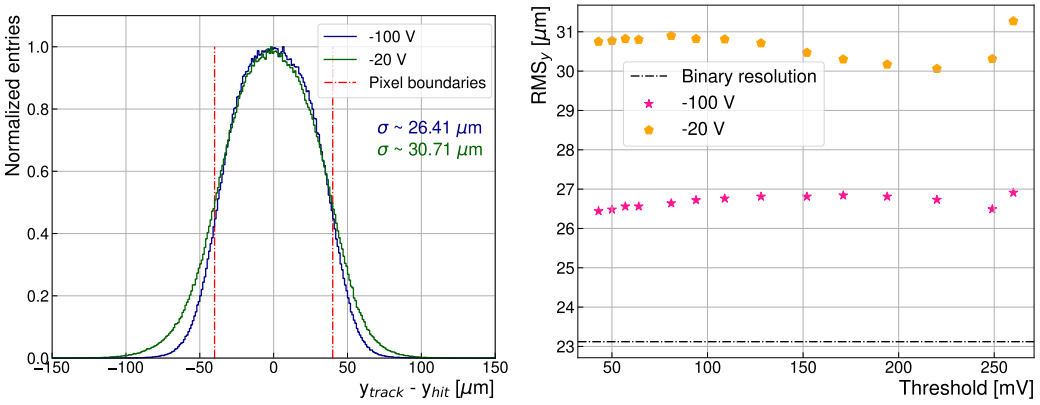

(a) For different voltages and a 43 mV threshold

(b) As a function of the threshold.

Figure 112.: Position resolution along the y-axis for different voltages for a MuPix10 sensor thinned to 100 µm.

single-pixel clusters comprise the largest fraction of events, even for tracks close to the edge of the pixel, the residual distribution shape and the RMS is dominated by single-pixel clusters.

Contrary to the effect of charge sharing on efficiency, a larger cluster size for tracks passing close to the pixel edge improves the position resolution. This behavior is expected since hits with cluster size two have a cluster center near the pixel edge, decreasing the track-cluster residual.

The position resolution results without using a ToT-weighted cluster size position are shown in Appendix D

7.4. Time resolution

As discussed in subsection 6.6.3 and analogously to the spatial resolution, the time resolution can be determined as the width of time residuals between the timestamp of the associated cluster in the DUT and the trigger scintillators.

Figure 114 shows the time residual for a -100 V applied voltage. Without any additional processing, a resolution of σ=14.27 ns is achieved. The time resolution was quantified as the Gaussian-shaped distribution's RMS. It is important to note that the distribution center is displaced from zero due to a system delay in the EUDAQ framework.

Two effects are mainly responsible for the distribution tail [58]. First, row-dependent signal variations caused by different line lengths of the pixel point-to-point connections and a non-uniform routing scheme involving multiple metal layers causes

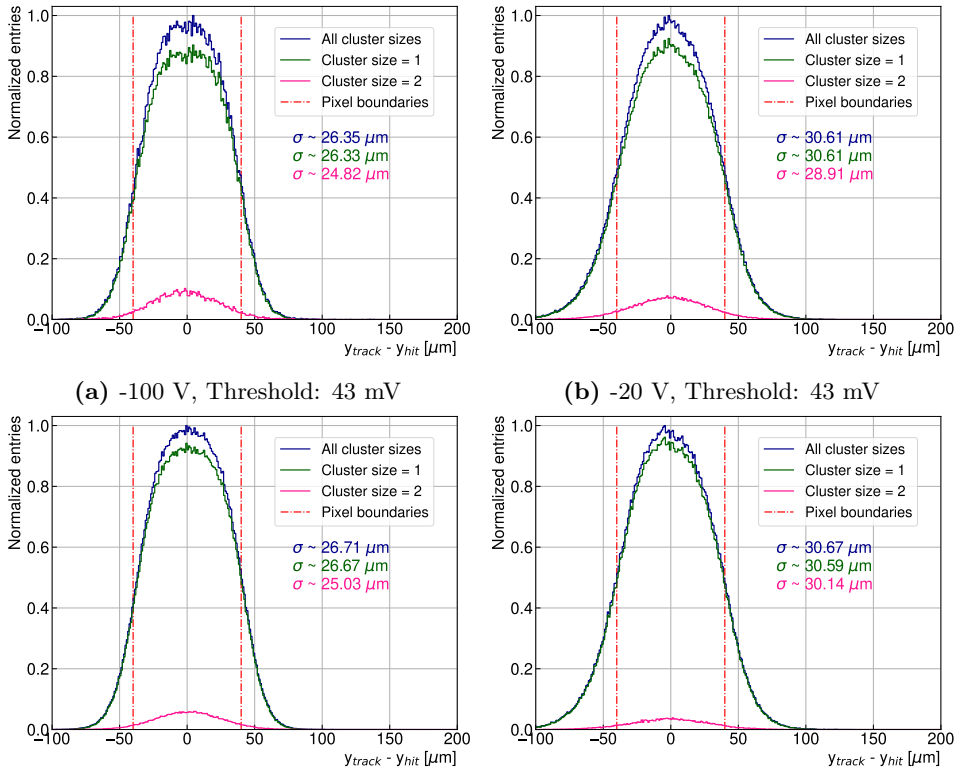

(a) -100 V, Threshold: 43 mV

(b) -20 V, Threshold: 43 mV

(c) -100 V, Threshold: 109 mV

(d) -20 V, Threshold: 109 mV

Figure 113.: Unbiased spatial residual distributions the y-axis for different cluster sizes at different thresholds and bias voltages for a MuPix10 sensor thinned to 100 µm.

variation in the line capacitance, which affects the signal shape and, consequently, the timing behavior. Second, timewalk from variations of the rising edge, depending on the amount of deposited energy.

Large signals can result in long ToT values that are not fully sampled. Figure 115 shows the ToT distribution of the studied sensor using the settings presented in Appendix C. The peak of the ToT distribution corresponds to the delay time, and a good ToT correction is not really possible. Consequently, no timewalk correction is applied to the presented results, and the uncorrected values are used to compare the behavior between the different studied configurations. With a proper delay value, the time resolution of the MuPix10 sensor can be off-line improved to values $\approx$ 7 ns, as shown in the work presented in [41]. MuPix11, the last MuPix prototype, fixed the delay circuit for sampling larger pulses, allowing better timewalk corrections.

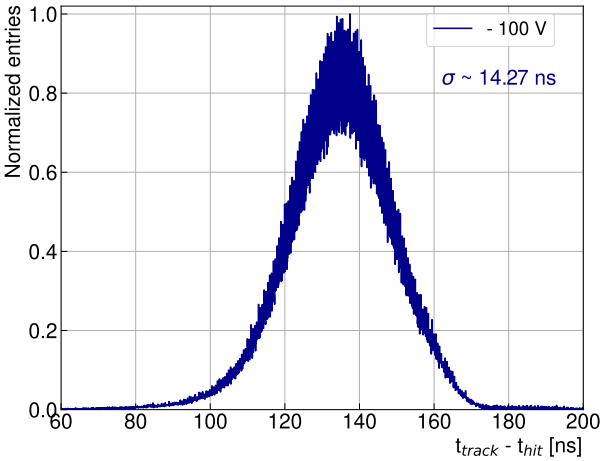

Figure 114.: Time residuals for a MuPix10 sensor thinned to 100 µm with -100 V voltage and 43 mV threshold.

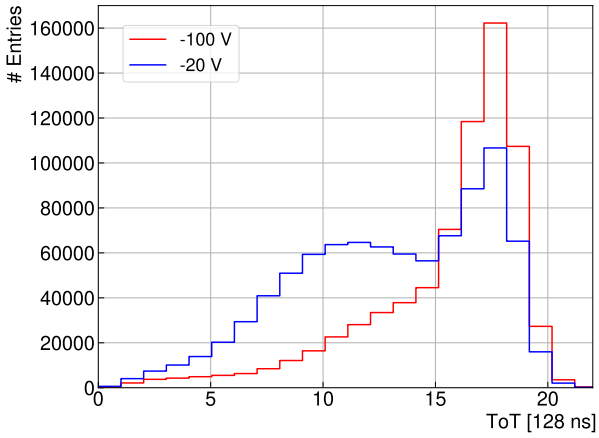

Figure 115.: ToT distribution for a MuPix10 sensor thinned to 100 µm at different bias voltage. The sensor settings are presented in Appendix C.

7.5. Studies with different sensor thicknesses

The previously studied sensor showed a large correlation between efficiency, charge sharing, and depletion depth. Increased charge sharing reduces the efficiency while large depletions improve it. To further study these effects, a MuPix10 sensor thinned to 50 µm was characterized. Chapter 5 showed that a MuPix10 sensor with the indicated thickness results in a breakdown of a few volts over -20 V. This section compares the cluster size and efficiency results of the 50 µm sensor with the 100 µm sensor at a voltage of -20 V.

7.5.1. Cluster size

A MuPix10 biased at -20 V results in almost full depletion for the 50 µm thinned sensor, while the 100µm has an extra ∼50 µm undepleted area where diffusion happens. This difference is shown in Figure 116 using TCAD simulations.

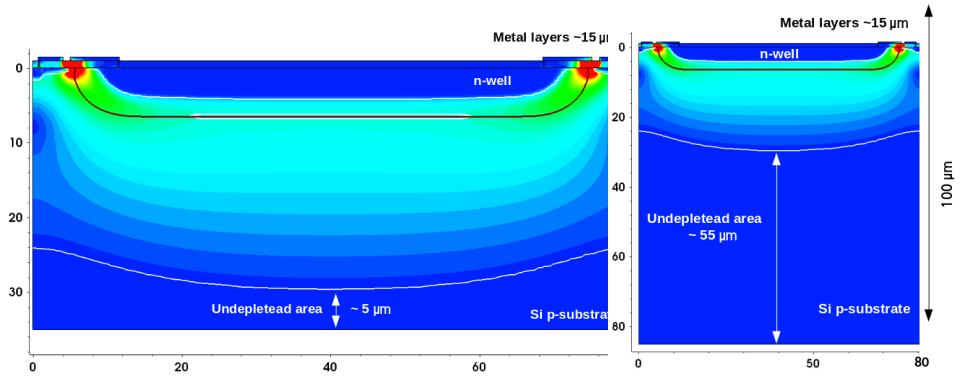

(a) 50 µm. **(b)** 100 µm.

Figure 116.: TCAD simulation of depletion depth for a MuPix structure with a substrate resistivity ∼355 Ωcm at -20 V for different sensor thicknesses.

Figure 117 shows the normalized cluster size distribution for both sensor thicknesses. A significant decrease in larger cluster sizes is observed for the 50 µm sensor. This decrease is related to the difference in the collected charge due to the diffusion component. The mean cluster size as a function of the threshold shows the expected behavior of a decrease with threshold increase until a minimum value, where the large energy deposition events start to be significant and increase the cluster size.

7.5.2. Efficiency

Figure 118 studies the efficiency as a function of the threshold for the different thicknesses. This result shows that for low thresholds, the charge collected in the first micrometers via drift is enough to pass the set threshold and result in efficiencies >99%. As the threshold increases, the sensor with the 50 µm thickness shows a reduced efficiency. The extra charge collected from the undepleted area for large threshold results in higher efficiencies for the 100 µm sensor. This effect was observed again in the in-pixel efficiency studies presented in Figure 119, where there is no significant difference in the in-pixel efficiency between the two sensor thicknesses at a 43 mV threshold. However, large thresholds show in-pixel efficiency distributions with the same behavior and lower efficiencies for the sensor thinned to 50 µm.

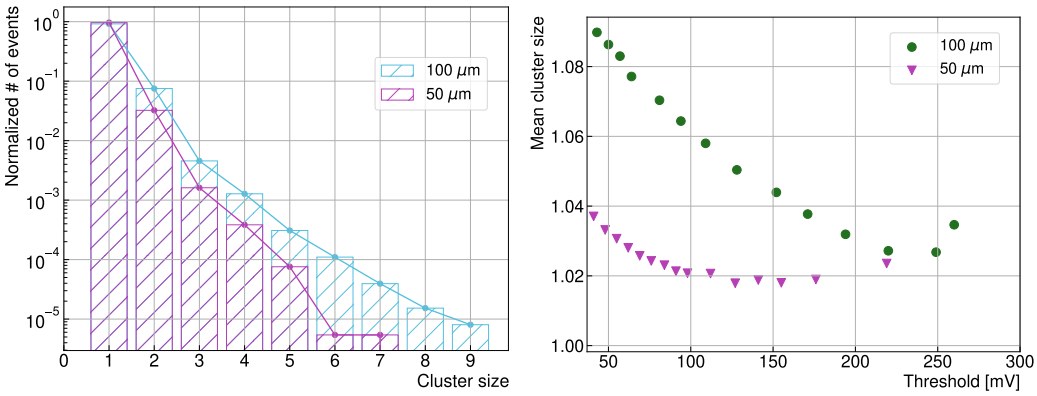

(a) Normalized cluster size for a 43 mV threshold. **(b)** Cluster size as a function of the threshold.

Figure 117.: Cluster size distribution for different MuPix10 sensor thicknesses at a bias voltage of -20 V.

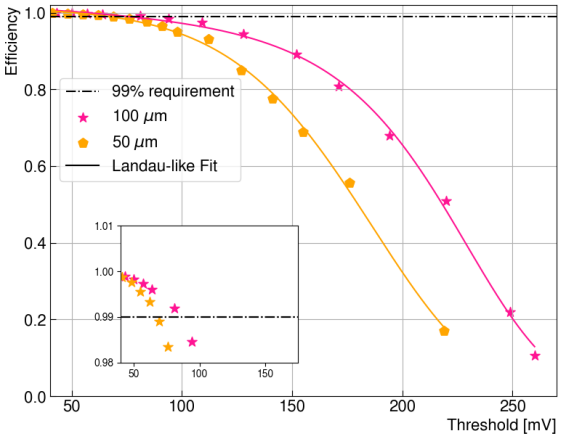

Figure 118.: Efficiency as a function of the threshold for MuPix10 sensors with different thicknesses at a bias voltage of -20 V.

7.5.3. TCAD simulation study of diffusion

The diffusion effect on the amount of collected charge was studied using TCAD. Figure 120 shows the electron density of a MIP passing through the center of the pixel along the full depth (combined), within the depletion zone (drift), and outside the depletion zone (diffusion). The simulated structure represents a MuPix10 sensor with a substrate resistivity of 355 Ω cm, biased at -20 V. The collected charge results (Figure 121) show that the diffusion represents ∼25% of the collected charge.

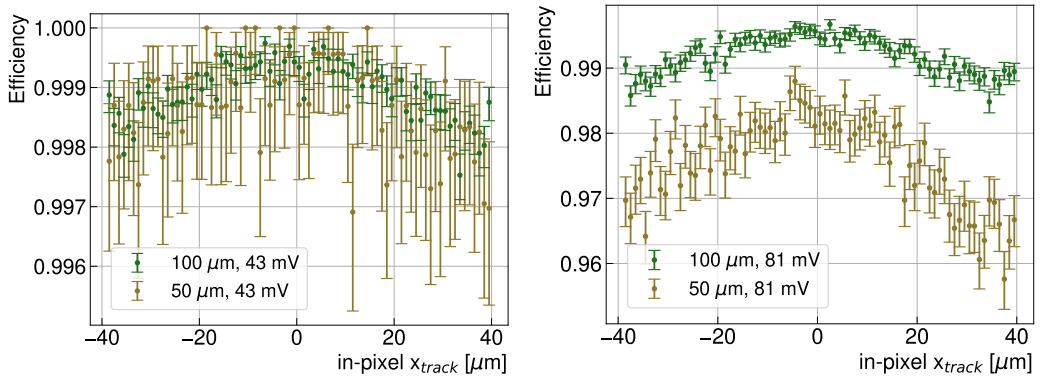

(a) Threshold:43 mV **(b)** Threshold: 81 mV

Figure 119.: MuPix10 in-pixel efficiency the x-axis for different thicknesses and thresholds at -20 V.

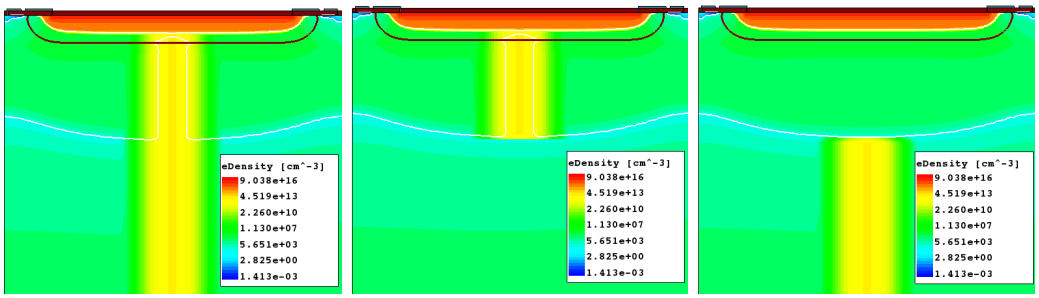

(a) Combined **(b)** Drift **(c)** Diffusion

Figure 120.: TCAD simulation of the interaction of a MIP with a Mupix10 sensor with a substrate resistivity $\sim$355 Ω cm at -20 V through different areas of the detector. The white lines define the border of the depletion zone. The color scale from sub-figure (c) describes the electrostatic potential for the three cases.

The difference between the combined simulation and the sum of the individual drift and diffusion components is related to the impact of the charge carriers on the electric field distribution during the drift and combined simulation [96]. The cloud of charges modified the strength of the electric field and, as a result, the charge collection process. Due to this, the diffusion is underestimated when simulated individually.

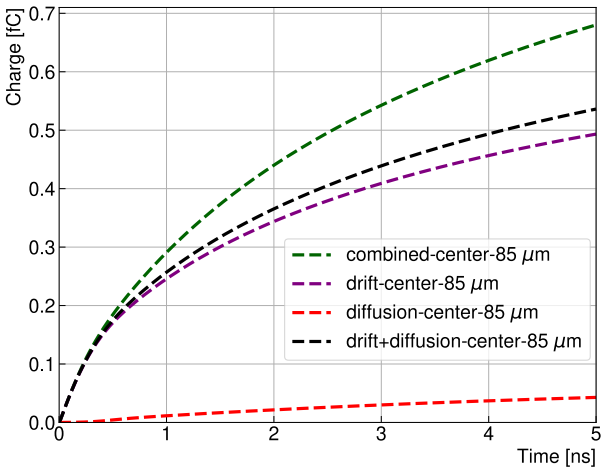

Figure 121.: TCAD simulation of accumulated charge for a MIP traversing through different areas of the detector in a MuPix10 sensor with a substrate resistivity ∼355 Ω cm and 100 µm thickness at -20 V.

7.6. Studies with different substrate resistivities

Chapter 5 discussed the difficulties of choosing the proper substrate resistivity. While a lower substrate resistivity results in a higher electric field, a high substrate resistivity has a larger depletion zone. This section shows the results of a MuPix10 sensor in a 10-20 Ω cm substrate thinned to 50 µm.

7.6.1. Efficiency

According to the results presented in Figure 82, a MuPix10 sensor with 10-20 Ω cm substrate has a breakdown voltage over -130 V. Figure 122 shows the efficiency result for a MuPix10 sensor in a 10-20 Ω cm substrate biased at -120 V. The threshold range for which the efficiency remains above 99% is significantly reduced compared to a similar sensor in a 200-400 Ω cm substrate.

The efficiency reduction is mainly due to the size of the depletion zone. Figure 123 presents the depletion zone for both resistivities at the highest operating voltage using TCAD simulation. While the higher resistivity substrate shows large depletions, the lower substrate for a higher voltage has a small depletion and might not be fully depleted in the inter-pixel region. If the detector cannot be operated at higher voltages due to breakdown, inefficiency in the edges and corners might disqualify the lower substrate for operation, particularly in high radiation environments where the damage caused to the substrate further reduces the depletion zone.

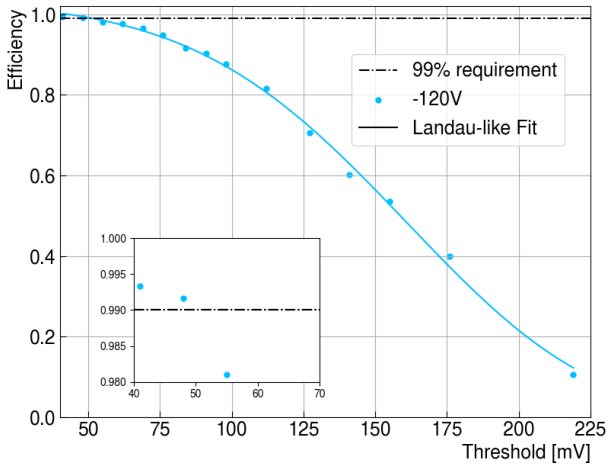

Figure 122.: Efficiency as a function of the threshold for a MuPix10 sensor with a substrate resistivity 10-20 Ω cm at -120 V thinned to 50 µm.

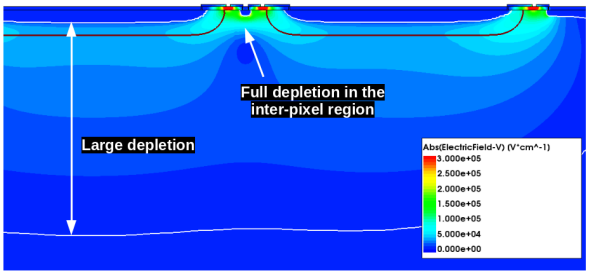

(a) ∼355 Ωcm at -100 V

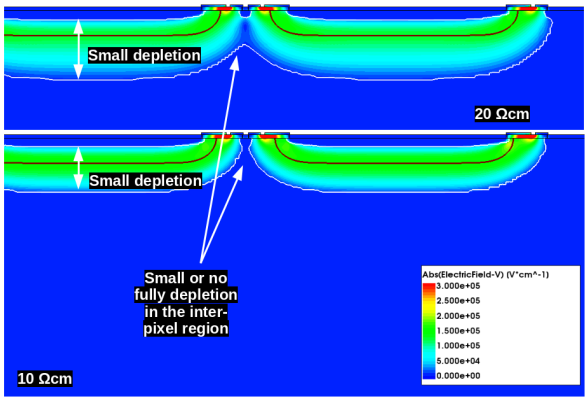

(b) 20 Ωcm at -120 V

Figure 123.: TCAD simulation of the depletion zone for a MuPix10 pixel structure thinned to 100 µm for different substrate resistivities.

In-pixel efficiency

The 10-20 Ω cm sensor results in efficiency with the same behavior as the previously analyzed detectors. The highest efficiency within the pixel center and a decrease towards the edge and corners can be observed in Figure 124a. A difference of the 200-400 Ω cm sensor, operating the detector at -20 V results in efficiencies below 99% even for the lower threshold (Figure 124b).

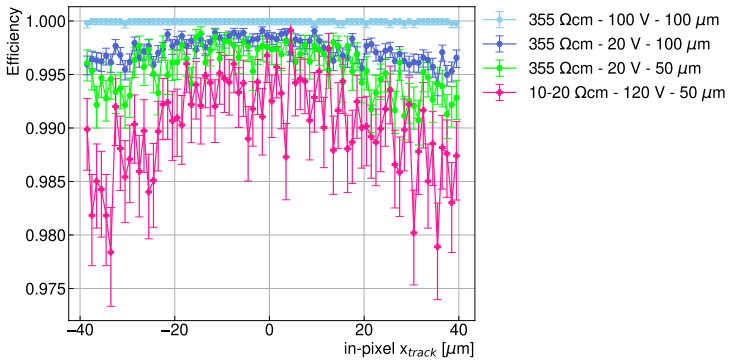

(a)

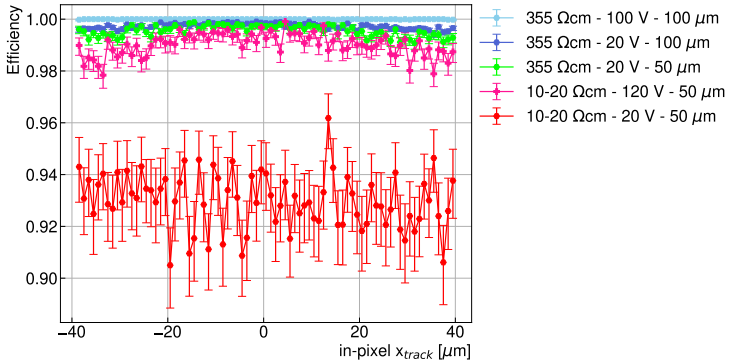

(b)

Figure 124.: (a) In-pixel efficiency along the x-axis for MuPix10 sensors with different substrate resistivity at a 50 mV threshold. (b) Longer efficiency range.

7.6.2. Time Resolution

The advantage of the low substrate resistivity is the high electric field that quickly collects signals via drift. As a result, the 10-20 Ω cm substrate quickly collects charge during the first micrometers, and then a slow diffusion process dominates the rest of the charge collection. Figure 125 shows the time residual for a 10-20 Ω cm at -120 V.

Compared with the previously studied sensor, the time resolution deteriorates due to the small depletion zone. These results suggest that the 200-400 Ω cm sensor has a better general performance for the current maximum operating voltages.

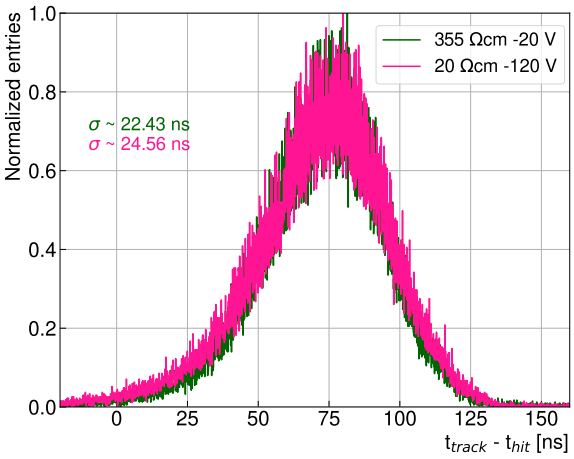

Figure 125.: Time residuals for MuPix10 sensors thinned to 50 µm with different substrate resistivities and voltages for a 43 mV threshold.

7.7. Rotation studies

HV-MAPS sensors are under study to be integrated into larger systems, such as particle detectors or medical imaging devices. Understanding how the particle's incidence angle affects the performance of the sensors is crucial for proper integration within such systems. By studying the sensors under different rotations[1], it is possible to identify the optimal orientation for achieving the best performance. Depending on the rotation, the cluster size is modified, and according to the analysis performed in the previous sections, the efficiency is also modified. It is important to note that the detector is rotated about the global y-axis, and as a result, the cluster size is modified in the row direction.

7.7.1. Cluster size

For a better understanding of the effect of the rotation on the detector behavior, the 100 µm MuPix10 sensor produced in a 200-400 Ω cm substrate was used. This sensor produces larger depletion zones than the 10-20 Ω cm and can be operated at higher

[1] At the testbeam, the orientation of the beam is fixed. Therefore, to change the particle's incidence angle the sensors need to be rotated.

voltages than the 50 µm prototype. The sensor was rotated by three different angles with respect to the normal to the sensor plane. The rotation angles are shown in Figure 126.

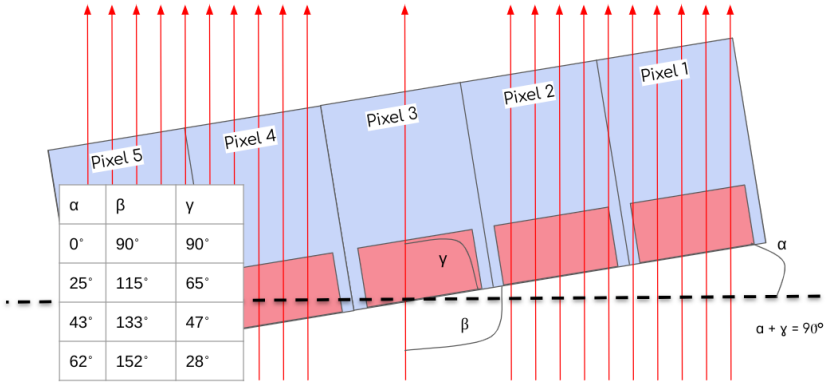

α	β	γ
0°	90°	90°
25°	115°	65°
43°	133°	47°
62°	152°	28°

Figure 126.: Sketch of the sensor rotations used during the testbeam and definition of the used angles. The red lines represent the beam.

The distance traveled by the particle inside the detector and how many pixels traverse for each rotation can be estimated using the pixel dimensions, as shown in Figure 127, where d represents the detector thickness, r is the distance along the row direction, and d' is the distance traveled by the particle inside of the detector. The distance along the row direction can be calculated as:

$$\begin{aligned} tan(\gamma) &= \frac{d}{r} = \frac{85}{r} \\ r &= \frac{85}{tan(\gamma)} [\mu\text{m}] \end{aligned} \tag{43}$$

For a 25° rotation:

In this case, the distance traveled along the row direction is equal to $r \approx 39.7\,\mu\text{m}$. Depending on the in-pixel position of the track, voltage, and threshold, the cluster size along the row direction will be between one and two, as shown in Figure 128a. Ideally, the cluster size is one for particles with an in-pixel position at the left of the pixel center and two for those with an in-pixel position at the right of the pixel center.

In reality, particles passing close to the edge diffuse to the neighbor pixel, and as a result, the cluster size can increase to two, as illustrated in Figure 128b. This behavior is affected by the applied voltage (size of the depletion zone) and the threshold. For

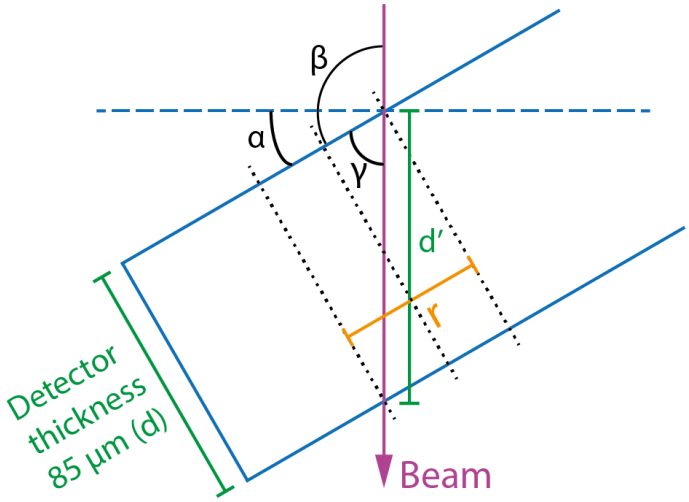

Figure 127.: Sketch to determine the distance a particle travels after rotation. The purple line represents the beam crossing the detector. The sensor thickness for the calculation was set to 85 µm due to the 15 µm of metal layers (Figure 63).

example, for particles traversing two pixels, the cluster size can be one for small depletion zones and high thresholds (Figure 128c) or two for low thresholds and large depletion zone (Figure 128d).

The resulting mean cluster size for different thresholds at -20 V is shown in Figure 129. The expected and previously described behavior for the row cluster size is observed. The mean cluster size increases for particles with an in-pixel position at the right of the pixel center as particles crossing the detector in this region traverse two pixels. The sensor depletion width is ∼30 µm for a bias voltage of -20 V. This results in a small area where the track passes inside the depletion zone of the two neighbor pixels. Since most of the charge in the neighbor pixel is created outside of the depletion zone, the resulting mean row cluster size width is ∼1. In the column direction, some unintentional rotation is observed due to the weight of the mechanical structure of the setup.

For a 43° rotation:

For this case, the distance traveled along the row direction is $r \approx 79.4\,\mu m$. Based on the voltage and threshold, the cluster size along the row direction is between one and two, as pictured in Figure 130.

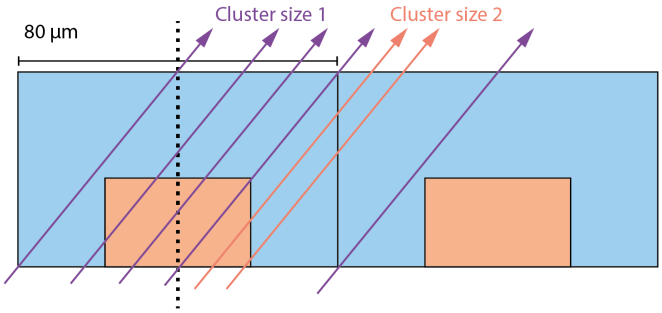

(a) Idea cluster size case.

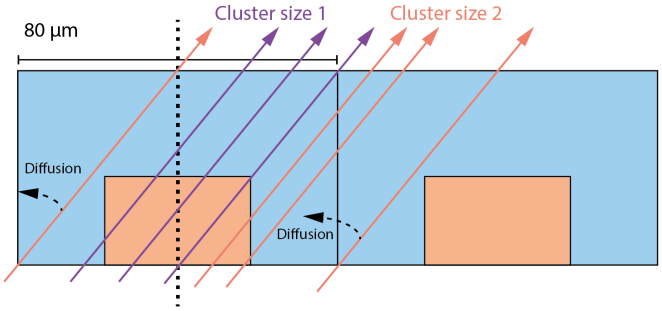

(b) Cluster size considering lateral diffusion.

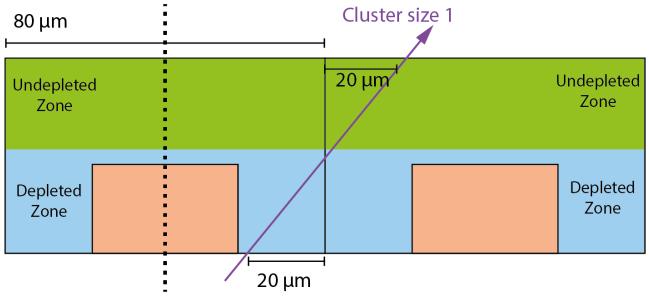

(c) Cluster size considering a small depletion zone.

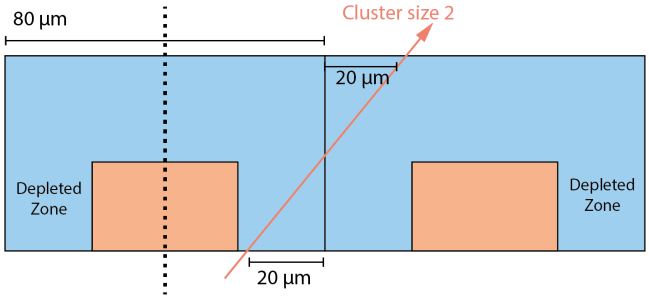

(d) Cluster size considering a large depletion zone.

Figure 128.: Sketch of the cluster size variations for a 25° rotation.

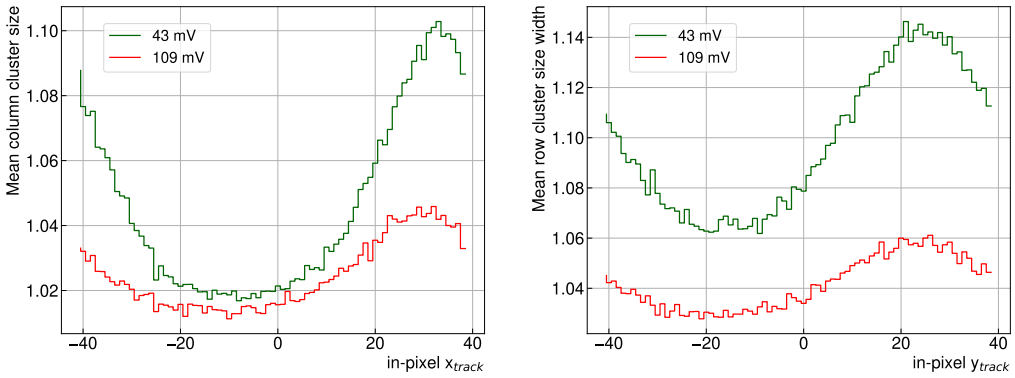

(a) Column **(b)** Row

Figure 129.: Mean cluster size width for a 25° rotation of a MuPix10 sensor thinned to 100 µm at a bias voltage of -20 V for thresholds of 43 and 109 mV.

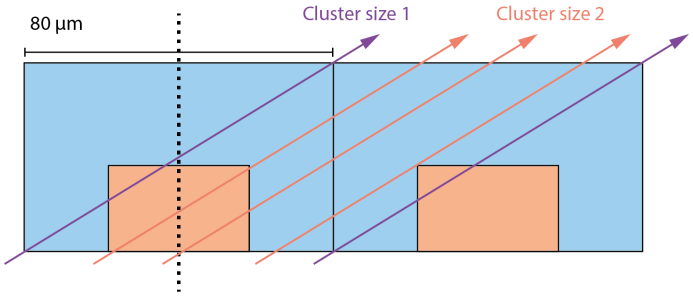

(a) Ideal cluster size case

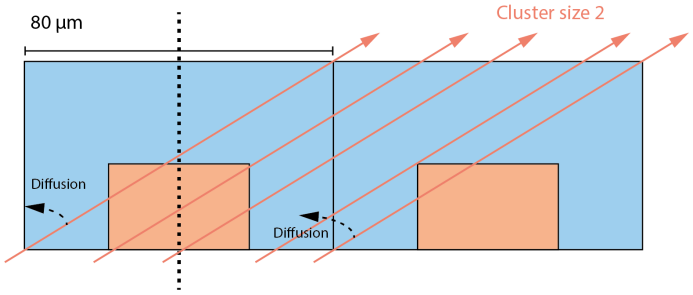

(b) Cluster size considering lateral diffusion.

Figure 130.: Sketch of the cluster size variations for a 43° rotation.

For particles entering the sensor at the edge, a cluster size of one is ideally expected because they have a path along one pixel (Figure 130a), but as seen in the case of the 25° rotation, due to diffusion, the cluster size increases in the edge (Figure 130b). For the rest of the in-pixel positions, the particles cross two pixels. As a result, a cluster size of two is expected for all the in-pixel positions.

This behavior depends on the depletion width. Compared with the 25° rotation, more particles will have a path inside the depletion zone of two adjacent pixels. Hence, an increase in the mean cluster size is observed. The resulting mean cluster size as a function of the track position along row direction within the pixel showing the previously described behavior is shown in Figure 131 for four bias voltages. Larger cluster sizes for higher voltages result from larger depletions that increase the amount of collected charge in the neighbor pixel.

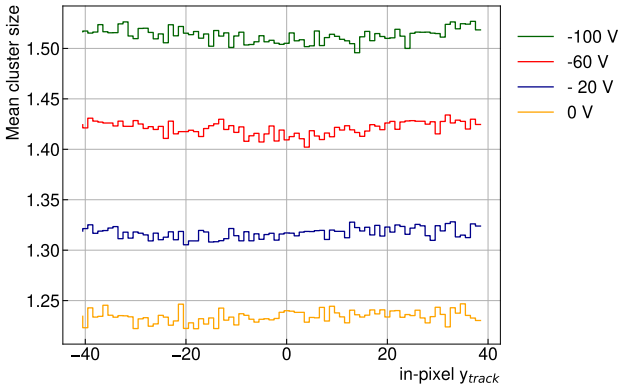

Figure 131.: Mean cluster size width as a function of the track position along row direction within the pixel for a 43° rotation of a MuPix10 sensor thinned to 100 µm at different voltages for a 43 mV threshold.

For a 62° rotation:

When particles enter the sensor at an angle of 62°, the distance traveled along the row direction is equal to $r \approx 160.4\,\mu m$. Depending on the voltage and threshold, the resulting cluster size along the row direction is between two and three, as shown in Figure 132a. For particles entering the sensor at the edge, a cluster size of two is ideally expected because they have a path along two pixels (Figure 132a), but as seen from the previous study rotations, due to diffusion, the cluster size increases in the edge (Figure 132b). For the rest of the in-pixel positions, the particles cross three pixels. As a result, a cluster size of three is expected for all the in-pixel positions (Figure 132b). Figure 133 shows the mean cluster size for different voltages. In the third pixel of the particles path, the charge is mostly deposited outside of the depletion zone, and as a result, a mean cluster size value closer to two is obtained. For lower voltages, as the depletion zone decreases, the charge created in the second pixel is also deposited outside the depletion zone, decreasing the mean cluster size.

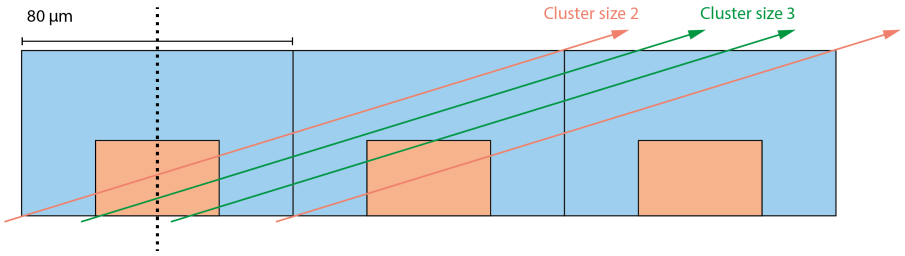

(a) Ideal cluster size case

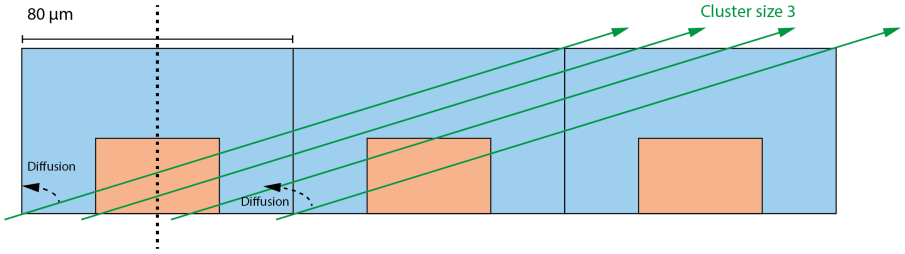

(b) Cluster size considering lateral diffusion.

Figure 132.: Sketch of the cluster size variations for a 62° rotation

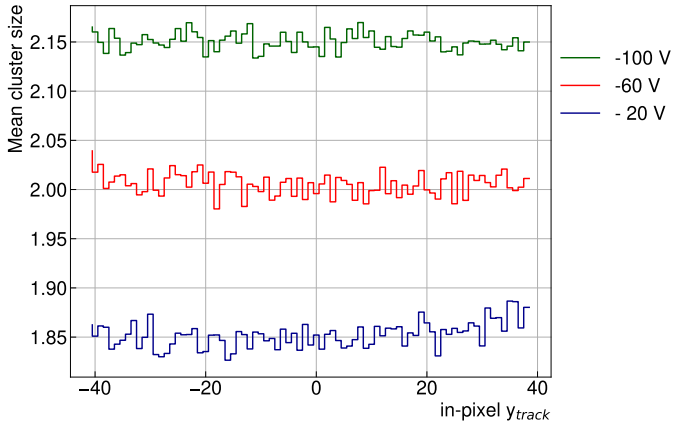

Figure 133.: Mean cluster size width as a function of the track position along row direction within the pixel for a 62° rotation of a MuPix10 sensor thinned to 100 µm at different voltages for a 43 mV threshold.

Figure 134 and 135 show the cluster size, column, and row width distribution for the different rotations, voltages, and thresholds. The results show an increase in cluster size for large rotations. For a 62° rotation, hits with cluster size two dominate for low thresholds at -20 V. For the highest voltage, two-pixel hits dominate even for high thresholds. The column cluster size width is dominated by single-pixel hits because there are only small unintentional rotations about the global x-axis.

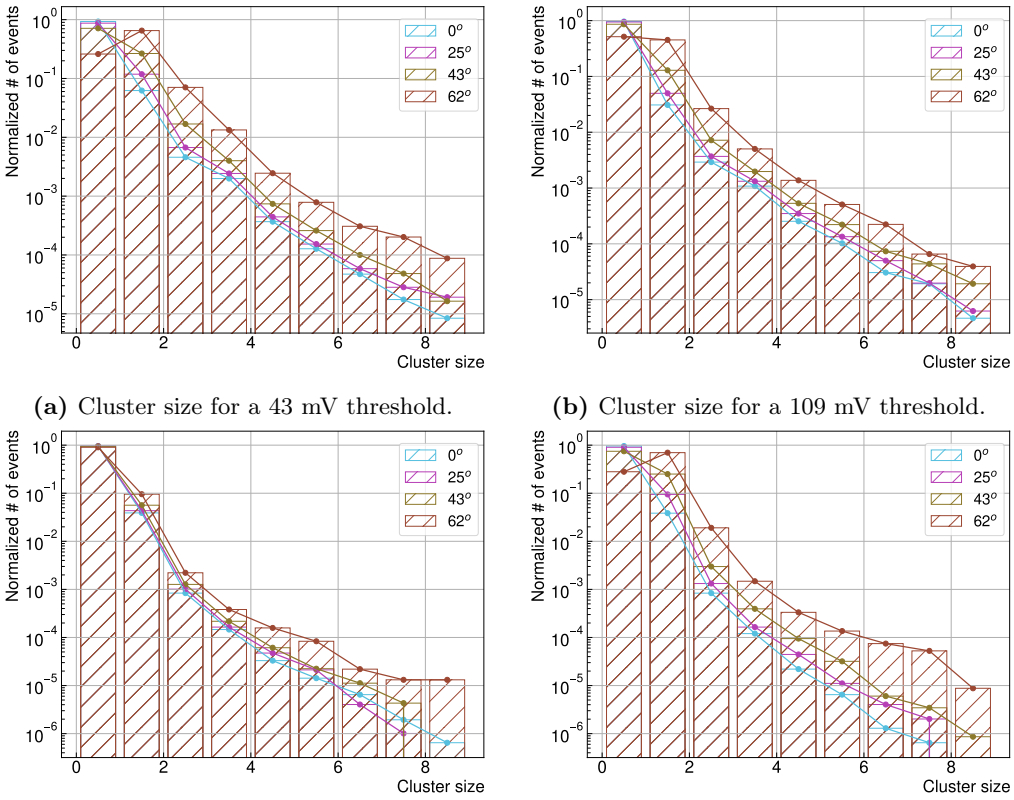

(a) Cluster size for a 43 mV threshold.

(b) Cluster size for a 109 mV threshold.

(c) Column cluster size for a 43 mV threshold.

(d) Row cluster size for a 43 mV threshold.

Figure 134.: Normalized cluster size, column, and row width distribution for MuPix10 sensors thinned to 100 µm at different rotations for a -20 V bias voltage.

7.7.2. Efficiency

Figure 136 shows the efficiency for different rotations at a -20 V bias voltage. The results show a slight decrease in efficiency up to a minimum of around 86% at ∼13°. For larger angles, the efficiency increases despite the larger cluster size. This behavior results from an increased path of the particle inside the depletion zone, which increases the collected charge. The distance travel by particles inside the detector (d') is defined in Figure 127 as:

$$\begin{aligned} sin(\gamma) &= \frac{d}{d'} = \frac{85}{d'} \\ d' &= \frac{85}{sin(\gamma)} [\mu\text{m}] \end{aligned} \tag{44}$$

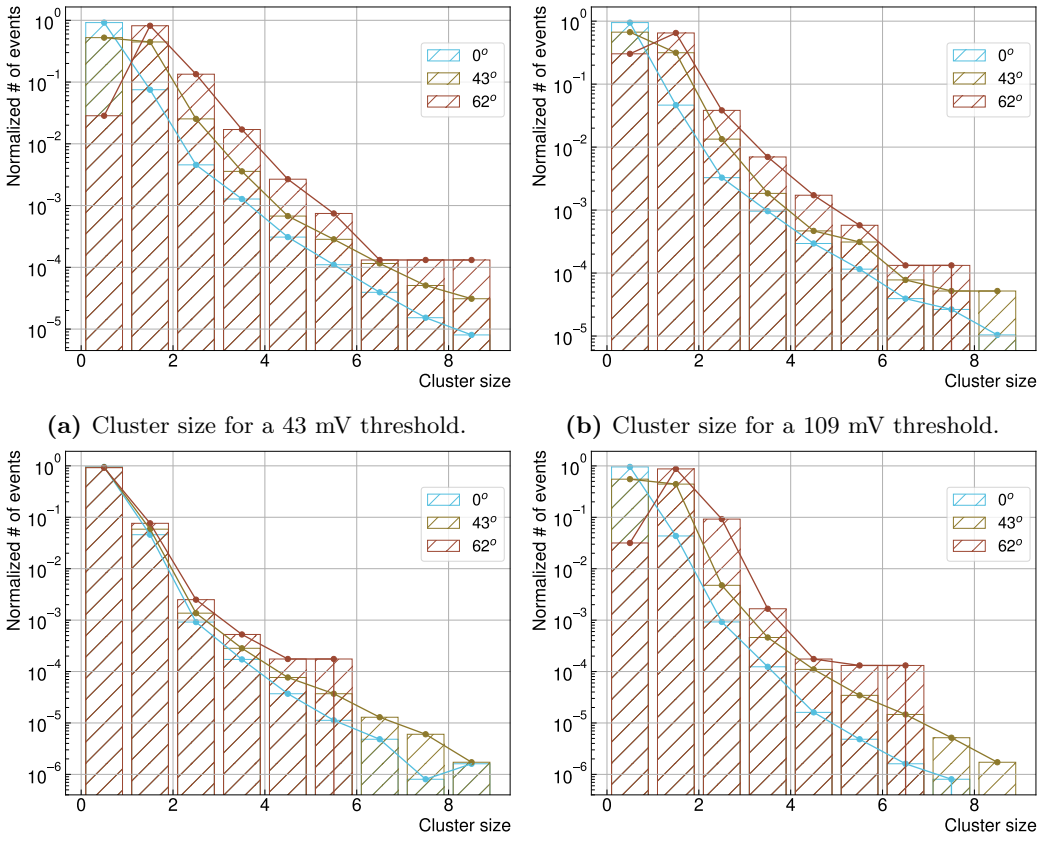

(a) Cluster size for a 43 mV threshold.

(b) Cluster size for a 109 mV threshold.

(c) Column cluster size for a 43 mV threshold.

(d) Row cluster size for a 43 mV threshold.

Figure 135.: Normalized cluster size, column, and row width distribution for MuPix10 sensors thinned to 100 µm at different rotations for a -100 V bias voltage .

A model that considers the individual contributions of the cluster size ($\propto \sin(\gamma)$) and the path inside the depletion zone ($\propto 1/\sin(\gamma)$) can be used to describe the efficiency behavior as a function of the angle.

The in-pixel efficiency results are shown in Figure 137. For the 25° rotation, the efficiency decreases correspond with the increased cluster size (Figure 137a). For the 43° and 62° rotation the efficiency increases as the particles have a longer path inside the detector (Figure 137b).

7.7.3. Resolution

Figure 138 presents the position resolution for a -20 V bias voltage and a 43 mV threshold for the investigated rotations.

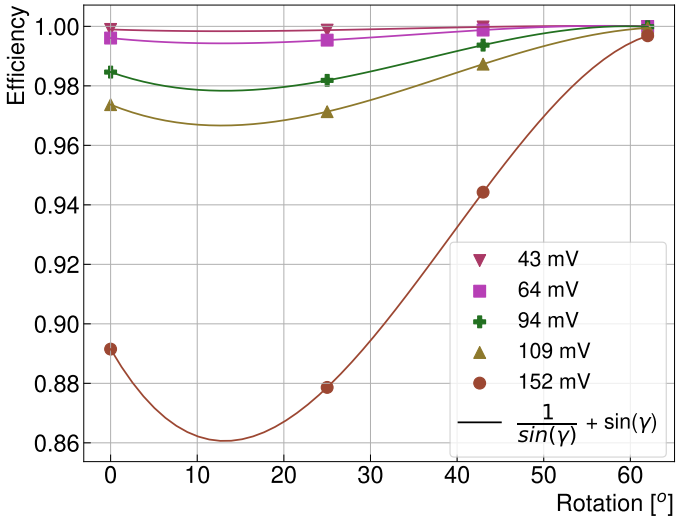

Figure 136.: Efficiency for different rotations of a MuPix10 sensor thinned to 100 µm at a -20 V bias voltage at different thresholds. Fitted as $1/\sin(\gamma)+\sin(\gamma)$

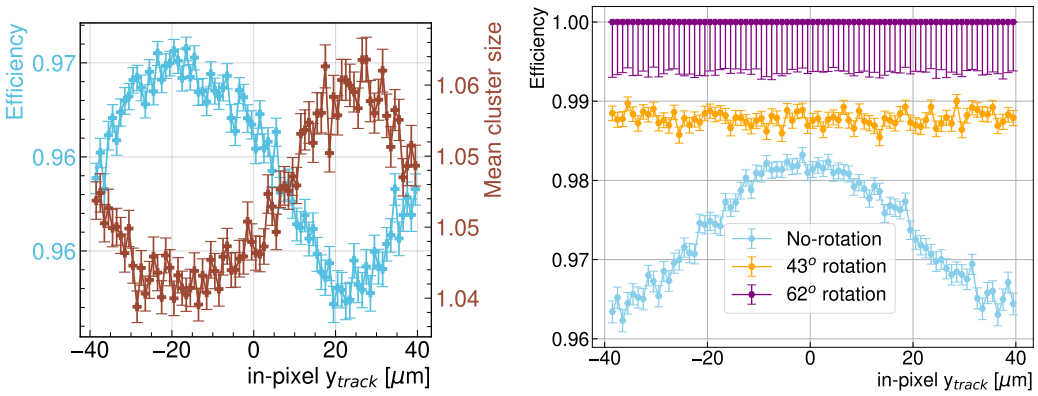

(a) 25°.

(b) 43° and 62°

Figure 137.: In-pixel efficiency along row direction within the pixel for different rotations of a MuPix10 sensor thinned to 100 µm for a -20 V voltage and a 109 mV threshold.

For the 25° rotation, the position resolution improves due to an increase in hits with cluster size two for tracks close to the right edge of the pixel, resulting in a resolution close to the binary resolution (23.12 µm). For a 43° rotation, the resolution worsens due to increased hits with cluster size two for particles with in-pixel positions close to the pixel center. Additionally, more tracks with an in-pixel position close to the right edge of the pixel are registered as a cluster-size one hit in the neighbor pixel,

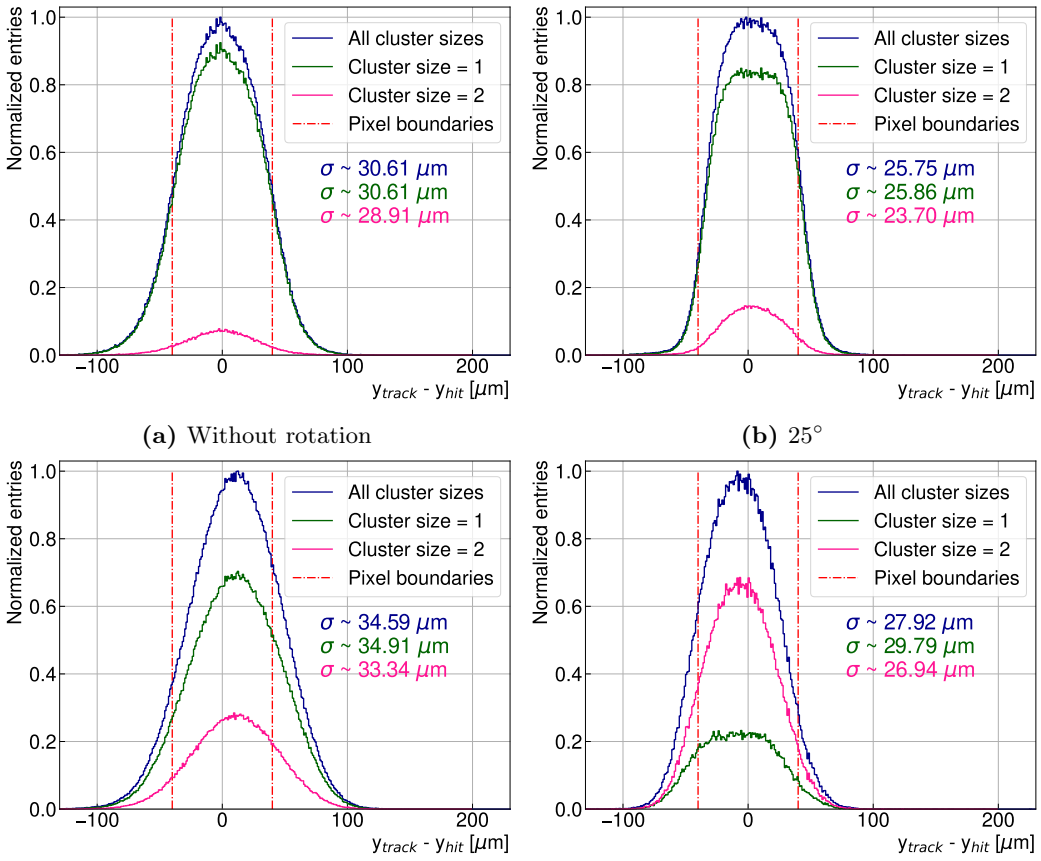

(a) Without rotation **(b)** 25°

(c) 43° **(d)** 62°

Figure 138.: Unbiased spatial residual distributions for different cluster sizes along row direction at a 43 mV threshold and a -20 V bias voltage for a MuPix10 sensor thinned to 100 µm.

producing an asymmetric residual distribution. For the 62° rotation, the increased number of cluster size two results in an improved position resolution.

These results show that the best position resolution is obtained for tracks that have cluster size one (as long as the hit is registered in the pixel where the particles first hit) and an in-pixel position near the pixel center and cluster size two for those with in-pixel positions close to the edge.

Figure 139 shows the position and time resolution behavior. In contrast to the spatial resolution, for a 25° rotation, the time resolution worsen due to the increased charge collection via diffusion for tracks close to the pixel edge. The particle's increased path inside the depletion zone improves the time resolution for larger rotations despite the increased charge sharing.

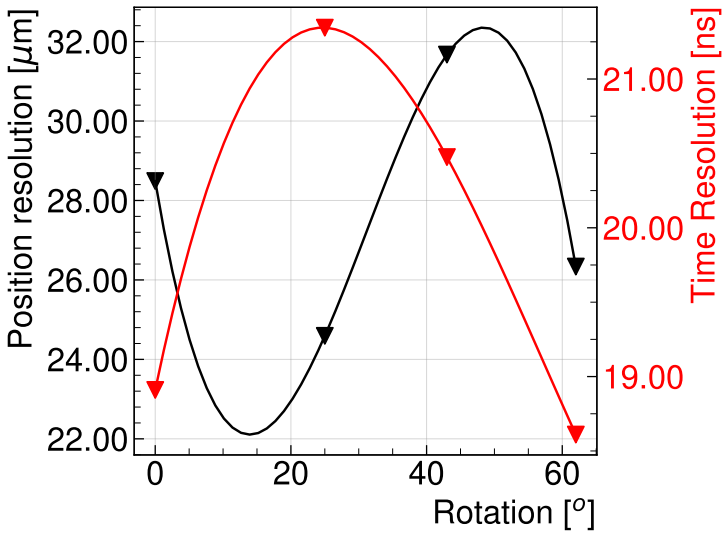

Figure 139.: Uncorrected time and spacial resolution along row direction for different cluster sizes at a 43 mV threshold and a -20 V bias voltage for a MuPix10 sensor thinned to 100 µm.

7.7.4. Sensor thickness

The efficiency, position, and time resolution for the different particle incidence angles depends on the sensor thickness. For example, for a 50 µm sensor[2] rotated 43°, the distance traveled along the row direction is equal to $r\sim$ 37 µm and the distance traveled by the particle inside the detector is equal to $d'\sim$ 51 µm. This results in a cluster size behavior similar to the previously shown for a 25° rotation for the 100 µm sensor. The in-pixel cluster size for the 50 µm sensor is compared with similar rotation in the 100 µm sensor in Figure 140a.

Another difference with the 100 µm sensor is that despite the increased mean cluster size for particles with in-pixel position to the right of the pixel center, the path of the particle in the neighbor pixel is inside of the depletion zone resulting in large charge collections and similar efficiencies for low thresholds in all the in-pixel positions (Figure 140b).

Figure 141 shows the resulting position and time resolution. Both resolutions show an improvement for the lower sensor thickness. The better position resolution for the 50 µm sensor is due to the smaller cluster size for tracks close to the pixel center and tracks being registered in the hit pixel.

[2]The sensor thickness for the calculation was set to 35 µm due to the 15 µm of metal layers

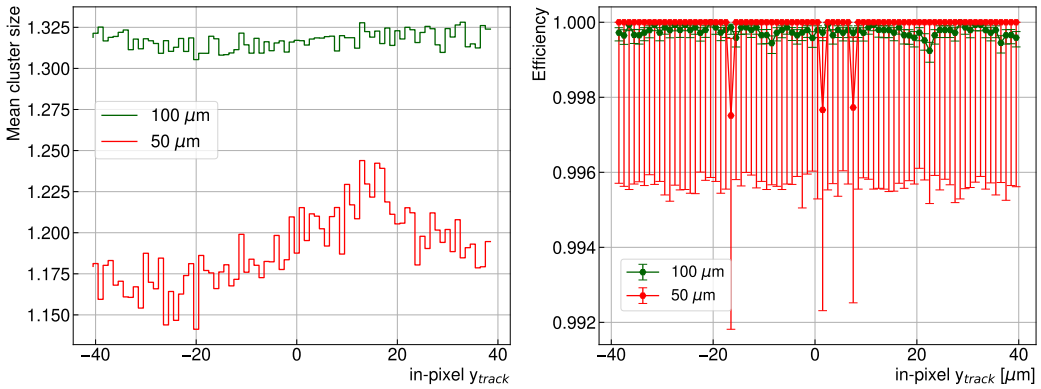

(a) Mean cluster size. **(b)** In-pixel efficiency.

Figure 140.: Mean cluster size and in-pixel efficiency along row direction for different substrate thicknesses at a 43 mV threshold and a -20 V bias voltage for a MuPix10 sensor with a 43° rotation.

The time resolution improvement results from most of the charge being collected via drift in contrast to the 100 µm sensor, where part of the charge is collected in the neighbor pixel via diffusion.

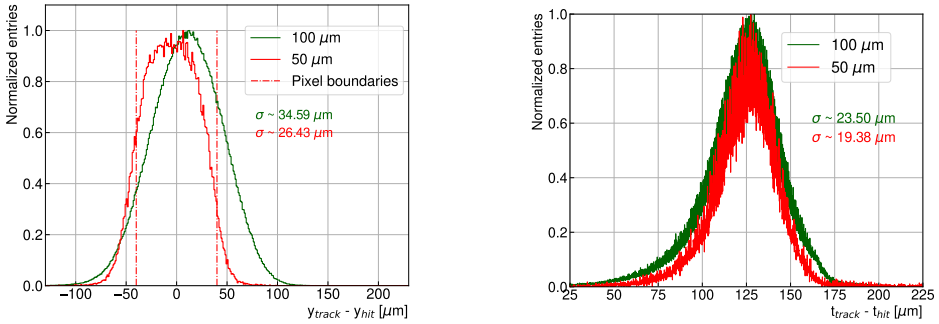

(a) Spacial resolution. **(b)** Time resolution.

Figure 141.: Uncorrected time and spacial resolution distributions for different substrate thicknesses at a 43 mV threshold and a -20 V bias voltage for a MuPix10 sensor with a 43° rotation.

Chapter 8

Conclusion

High-voltage Monolithic Active Pixel Sensors [38] have emerged as a highly promising technology in the field of silicon tracking detectors for particle physics experiments. The chips feature different pixel designs, with a variable pixel pitch and a highly doped n-well in a p-doped substrate as the collection electrode housing the in-pixel electronics integrated within the substrate. This design allows for the development of efficient and compact pixel sensors capable of handling high voltages, thereby enabling improved performance over traditional MAPS while keeping a low material budget. The sensors are biased through a high-voltage connection surrounding each pixel and an additional ring around the pixel matrix.

The foreseen tracking detectors are required to operate at high particle rates and unparalleled radiation damage levels, imposing stringent sensor performance requirements. These challenges have been addressed by the development of several HV-MAPS prototypes, which have been produced and extensively tested through a combination of testbeam measurements and simulations as part of dedicated research and development efforts for present and future detectors.

TCAD Simulations

Three different prototypes have been investigated using TCAD simulations in the framework of this thesis, MuPix8 [77], MuPix10, and ATLASPix [59]. The simulation focuses on the pixel layout, depletion zone, breakdown voltage, and electric field distribution to better understand their effects on pixel behavior. Such understanding enables pixel design optimization and a deeper comprehension of sensor behavior.

The simulation shows that the sensor's biasing structure affects the width of the depletion zone. A large depletion zone is crucial in detector operation as it enhances

the efficiency of charge collection and improves the overall sensitivity of the detector. HV-MAPS uses front-side biasing through the multi-metal layer structure offered by the technology [1]. The simulations indicate that the high voltage contact positioned outside the pixel matrix is critical to maintaining a constant electrostatic potential for the p-side of the junction, even when the depletion region covers the HV contacts in the inter-pixel region. As a result, the depletion zone exhibits a more gradual increase in size as a function of the applied voltage, leading to improved performance of the detector.

The lateral depletion was evaluated as a critical factor affecting the detector efficiency. Horizontal depletion is dominated by the applied voltage, substrate resistivity, and the radius of curvature of the n-well edge, all well-described 2D parameters. As a result, 2D simulation can accurately describe the lateral depletion width. In contrast, 3D simulation was found necessary to describe the depletion zone at the pixel corner. The depletion zone analysis in the corner of the pixel for a MuPix8 sensor biased at -15 V in an 80 Ω cm substrate shows that the pixel corners are not fully depleted, and consequently, during operation at high thresholds, the efficiency decreases in these areas. These results agree with the in-pixel efficiency studies presented in [77].

The substrate resistivity is an important factor that affects the electrical properties of the pn-junction. Accurate prediction of wafer resistivity is crucial in understanding and analyzing the behavior of the depletion region, allowing for better characterization and optimization of device performance. MuPix10 current-voltage curves obtained for different sensor thicknesses and TCAD simulation results of the depletion zone were used to estimate the sensor resistivity. This is done by measuring the sudden increase in leakage current for different thicknesses at different voltages. One explanation for this behavior is a high surface current contribution to the leakage current when the depletion region extends to the backside of the sensor due to a layer of damaged silicon (∼5 µm [79]) created as a result of backside mechanical grinding. Reports on this effect have been made in [26], and an additional etching step after backside grinding was found to mitigate it. The results for the different sensor thicknesses agree in a wafer resistivity of 355 Ω cm. The resulting value is within the 200-400 Ω cm range reported by the wafer supplier.

Isolation is critical for decreasing crosstalk between pixels, as it interrupts or eliminates the electron accumulation layer created between the pixels due to holes

[1] Front-side biasing is used in most of the HV-MAPS prototypes, but back-side biasing is possible and was studied in the work presented in [59].

trapped in the oxide interface. The inter-pixel region was investigated, and p-stop and p-spray isolation techniques [28] were tested. A modified isolation technique combining a high boron dose with a low-dose p-spray was also studied and showed the best behavior regarding higher breakdown voltage and lower crosstalk. The modified isolation technique with a high boron dose of $1x10^{18}$ cm^{-3} and a low p-spray of $2x10^{16}$ cm^{-3} was found to describe MuPix10 experimental breakdown voltages for different resistivities and sensor thickness for which the breakdown voltage doesn't correlate with the extension of the depletion zone to the backside of the sensor. For the 200-400 Ω cm sensors, an experimental breakdown of -108 V was measured for a 100 µm sensor thickness, and -106 V is obtained with TCAD simulation. Similar behavior is observed for the 20 Ω cm resistivity substrate, where simulation reveals a breakdown voltage of -133 V and experimental results of -135 V. Moreover, it was found that a short distance between the metal layers used to bias the substrate and the n-well modifies the electric field distribution in the inter-pixel region, reducing the maximum operating voltage of the sensor.

Capacitance is a sensitive parameter that directly affects the signal-to-noise ratio and the detector response time. Different contributions to the capacitance were studied using TCAD simulations for the ATLASPix3, MuPix8, and MuPix10 structures. An inter-pixel capacitance lower than 1 fF was determined due to pixel isolation. Junction capacitance and the capacitance created between the n-well and the p-well that houses the in-pixel PMOS transistors present the highest contribution. A capacitance in the order of 10^2 fF was estimated for all the structures, which is the typical capacitance for which Si detectors are designed to operate.

MuPix10 testbeam characterization

Further analysis was performed using the MuPix10 with an electron beam at DESY and the ADENIUM reference telescope, which provides a pointing resolution below 3 µm [85] that allows for resolving sub-pixel effects. These studies aimed to gain insights into the relationship between cluster size and efficiency. In addition, for studying the cluster size, the DUTs were rotated using a rotation station provided by DESY. In many applications, particles may not enter the sensor perpendicular to its surface. Therefore, studying its performance at different incident angles can help determine its capabilities, limitations, and suitability for various applications.

For a sensor thickness of 100 µm and a substrate resistivity of 200-400 Ω cm, the efficiency was found to exceed 99% for low thresholds and bias voltages of -100 V,

-60 V, and -20 V. However, the in-pixel efficiency results exhibited lower efficiencies at the edges and corners of the pixel due to increased charge sharing. In-pixel cluster size, defined as the mean cluster size as a function of the track position inside the pixel, confirmed the decrease in efficiency in areas with larger cluster sizes. These experimental findings were further studied by TCAD simulations, which showed up to ∼50% decrease of the charge collected for a MIP passing through the middle of the gap between two pixels compared to the charge collected when passing through the center of the pixel.

A spatial resolution of 26 µm, dominated by hits with cluster size one, was achieved at a bias voltage of -100 V. TCAD simulations revealed that due to the electric field distribution within HV-MAPS, a significant diffusion to neighboring pixels occurs only when particles traverse within a few micrometers from the middle of the gap ($<$ 5 µm), considerably reducing the number of hits with cluster sizes larger than one.

It was observed that reducing the sensor thickness leads to decreased efficiency as the sensing volume is reduced, and the charges deposited in the undepleted volume and collected via diffusion are absent. TCAD simulations showed that for a 100 µm thick sensor biased to -20 V, the collected charge via diffusion contributes up to 25% to the signal. Additionally, an investigation using a substrate resistivity of 20 Ω cm revealed that, despite the presence of a high electric field, the small depletion zone restricts the high efficiency ($>$99%) to low thresholds.

The sensors were rotated with respect to the beam incidence direction such that the normal to the sensor plane and the beam direction formed three angles 25°, 43°, and 62°. These studies demonstrated that the efficiency increases with the rotation angle except for low rotations ($<$ 13° according to the fit). These results can be well described by a model which considers the individual contributions of cluster size and the path inside the depletion zone.

For the lowest rotation angle (25°), tracks with an in-pixel position close to the pixel edge traverse two pixels. In the second pixel, the charge is mostly deposited in the undepleted portion of the volume, leading to a collected charge below the threshold and, thus, a decrease in efficiency. The time resolution is also affected for low rotations due to the increased charge collected via diffusion. The contrary effect is seen in the position resolution, where low rotation angles offer the best performance. The improved performance is due to an increase in cluster size two for tracks with an in-pixel position close to the sensor edge, whereas cluster size one is predominant for particles close to the center of the pixel.

Table 4 summarizes the efficiency, position, and time resolution (without offline

corrections) for the different studied angles for a sensor biased to -20 V and a 43 mV threshold. All these parameters are strongly dependent on the threshold and applied voltage since this directly impacts if a signal is registered and, accordingly, the cluster size.

Table 4.: Efficiency, position, and time resolution for different rotations for a MuPix10 sensor with a substrate resistivity 200-400 Ω cm, 100 µm thickness, -20 V and operated to a 43 mV threshold. The case without rotation was defined as 0.

	0	25°	43°	62°
Efficiency [%]	99.89	99.87	99.97	99.99
Position Resolution [µm]	30.61	25.74	34.59	27.92
Time Resolution [ns]	19.82	24.69	22.95	19.22

For a 50 µm sensor thickness, as required for the Mu3e experiment, the rotation effect was studied at -20 V for a 43° rotation. This voltage results in an almost fully depleted sensor (∼45 µm according to TCAD simulations) for the 50 µm sensor. The results show that for low threshold with efficiencies over 99% (for both sensors), the time resolution improves (19.38 ns) compared with the 100 µm sensor due to drift-dominated charge collection. Additionally, the 50 µm sensor results in a mean cluster size two for tracks with an in-pixel position close to the sensor edge, whereas cluster size one is predominant for particles with an in-pixel position close to the center of the pixel, similar to the behavior of the 100 µm sensor with a 25° rotation. As previously seen, this configuration results in an improved position resolution (26.43 µm).

The studies presented in this thesis are not just relevant to the Mu3e tracking system. The detailed study for different resistivities, bias voltages, pixel geometries, and cluster size analysis is also relevant for other applications where the HV-MAPS technology is foreseen to be employed.

In conclusion, it was shown that high-voltage monolithic active pixel sensors represent an attractive technology for many applications in future particle physics experiments and beyond. At the time that this thesis is being finalized, the next large-scale iteration of HV-MAPS prototypes, MuPix11, is being characterized.

Appendices

Appendix A

Carrier Concentration in Intrinsic Semiconductors

To obtain the electron density (i.e., the number of electrons per volume unit) in an intrinsic semiconductor, we first evaluate the electron density n(E) in an incremental energy range dE. n(E) is given by the product of the density of states N(E) and by the probability of occupying that energy range F(E). As a result, the electron density in the conduction band is given by integrating N(E)F(E)dE from the bottom (equal 0 for simplicity) to the top of the conduction band E_C:

$$n = \int_{E_C \equiv 0}^{\infty} n(E)dE = \int_{E_C \equiv 0}^{\infty} N(E)F(E)dE \tag{45}$$

The density of states is the density of allowed energy states per energy range per volume unit and calculated [7] as:

$$N(E)dE = 4\pi(\frac{2m_n}{h^2})^{2/3}E^{1/2}dE \tag{46}$$

Where m_n is the effective mass of electrons and F(E) is the probability that an electron occupies an electronic state with energy E, which is given by the Fermi-Dirac distribution as a function of the Fermi energy E_F (the energy at which the probability of occupation by an electron is one-half) as:

$$F(E) = \frac{1}{1 + e^{(E-E_F)/kT}} \tag{47}$$

Then the density of electrons n (p) results in:

$$n = N_C e^{-\frac{E_C - E_F}{kT}} \qquad \text{with } N_C = 2(\frac{2\pi m_n kT}{h^2})^{3/2} \tag{48.1}$$

$$p = N_V e^{-\frac{E_F - E_V}{kT}} \qquad \text{with } N_V = 2(\frac{2\pi m_p kT}{h^2})^{3/2} \tag{48.2}$$

Where m_n (m_p) is the effective mass of electrons (holes), E_C (E_V) is the energy of the conduction (valence) band, and E_F is the Fermi energy. N_C (N_V) is known as the effective density of states in the conduction (valence) band. Using the relationship of electrons and holes for an intrinsic semiconductor (Eqs. 1), the Fermi level for an intrinsic semiconductor is obtained:

$$E_F = \frac{E_C + E_V}{2} + \frac{kT}{2} \ln \frac{N_V}{N_C} \tag{49}$$

At room temperature (300 K), $\frac{kT}{2} \ln \frac{N_V}{N_C} \gg \frac{E_C + E_V}{2}$. Therefore, E_F of an intrinsic semiconductor generally is very close to the middle of the bandgap.

Figure 142 shows schematically, from left to right, the band diagram, the density of states N(E), which varies as $\sqrt{E}$ for a given electron effective mass, the Fermi distribution function, and the carrier concentrations for an intrinsic semiconductor.

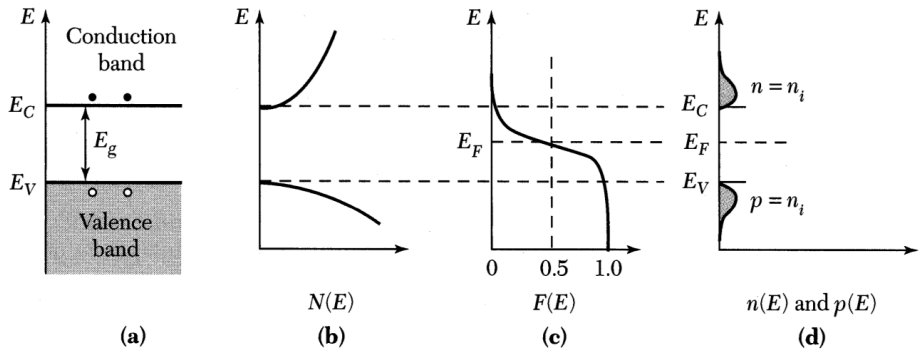

Figure 142.: Intrinsic semiconductor. (a) Schematic band diagram. (b) Density of states. (c) Fermi distribution function. (d) Carrier concentration. [7]

The product of electrons and holes concentrations

$$np = n_i^2 = N_C N_V e^{-\frac{E_g}{kT}} \tag{50}$$

is independent of E_F and, hence, also independent of the doping concentration, and the intrinsic carrier density is equal to:

$$n_i = \sqrt[2]{N_C N_V} e^{-\frac{E_g}{kT}} \tag{51}$$

At room temperature, n_i = 9.65x10^9 cm^{-3} for silicon [7].

Appendix B

Physics in TCAD Simulations

```
Physics
        {
                Temperature = 293
                Fermi
                eQCvanDort
                Mobility
                        (
                                DopingDependence
                                eHighFieldSaturation
                                hHighFieldSaturation
                        )
                Recombination
                        (
                                SRH
                                        (
                                                DopingDependence
                                                TempDependence
                                                ElectricField
                                                        (
                                                                Lifetime=Schenk
                                                                DensityCorrection=Local
                                                        )
                                        )
                                Auger(WithGeneration)
                                Band2Band
                                eAvalanche (Okuto ElectricField BandgapDependence)
                                hAvalanche (Okuto Electricfield BandgapDependence)
                        )
                EffectiveIntrinsicDensity(JainRoulston)
        }
```

Figure 143.: Physics used in SDEVICE TCAD simulations [75]

Appendix C

Sensor configuration

DAC/Configuration bits	value	DAC/Configuration bits DAC/Configuration bits	value
VNPix	a	VPVCO	18
VNFBPix	5	VNVCO	1a
VNFollPix	2	VPDelDclMux	14
VNPix2	0	VNDelDclMux	a
VNBiasPix	0	VNDelDclMux	f
VPLoadPix	2	VNDelDcl	a
VNOutPix	5	VPDelDclEmp	a
VNDel	a	VNDelDclEmp	f
VPComp1	a	VPDcl	1e
VPDAC	0	VNDcl	f
BLResDig	2	VNLVDS	a
VPComp2	a	VNLVDSDel	0
VPTimerDel	1	VPPump	28
VNTimerDel	28	invert	0
sendcounter	0	SelEx	0
tsphase	0	SelSlow	0
linksel	0	EnPLL	1
Ensync_SC	0	ckdivend	0
slowdown|DCol|End	7	ckdivend2	1f
En2thre	1	timerend	1
AlwaysEnable	1	slowdownend	0
Tune_Reg_R	0	maxcycend	3f
Tune_Reg_L	0	resetckdivend	0
Aur_res_n	1	count_sheep	0
Ser_res_n	1	SelFast	0
RO_res_n	1	Bandgap_on	0
conf_res_n	1	BiasBlock_on	5
disable_HB	1	VNHB	0
TestOut	8	VPFoll	0

Figure 144.: Configuration settings.

Appendix D

Comparison of Arithmetic and ToT-weighted cluster center

For the results presented in Chapter 7, the cluster center is determined as the ToT-weighted of the pixels within the cluster using Equation 42. In contrast, Figure 145 shows the unbiased residuals for different cluster sizes and voltages for a cluster position determined as the arithmetic mean according to the equation:

$$y_{cluster} = \frac{1}{n} \sum_{i=1}^{n} y_i \tag{52}$$

The comparison shows that due to a large number of single-pixel clusters, the overall difference is insignificant.

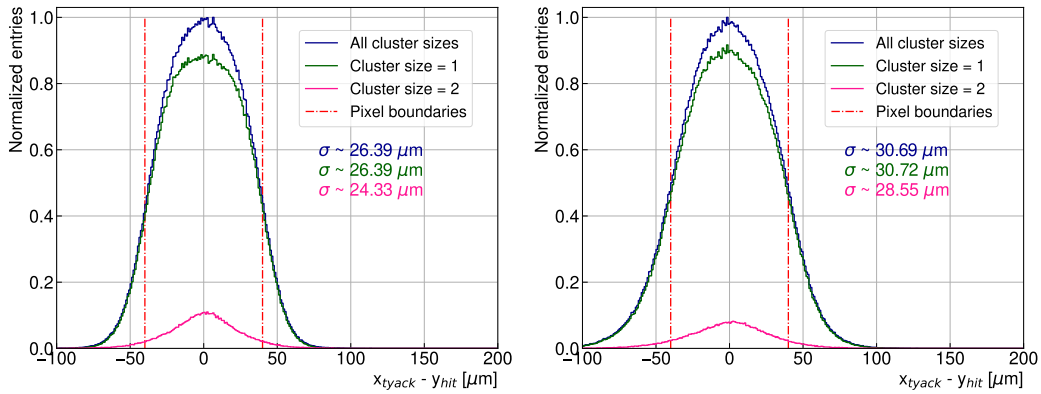

(a) -100 V **(b)** -20 V

Figure 145.: Unbiased spatial residual distributions for different cluster sizes and voltages at a 43 mV threshold and a -20 V bias voltage for a MuPix10 sensor thinned to 100 µm. The cluster center is determined as the arithmetic mean.

List of Publications

- Augustin, Heiko et al. [including **Annie Meneses Gonzalez**]. Efficiency and timing performance of the MuPix7 high-voltage monolithic active pixel sensor. Published in: *Nucl. Instrum. Meth. A* 902 (2018) 158-163.
- Augustin, Heiko et al. [including **Annie Meneses Gonzalez**]. Performance of the large scale HV-CMOS pixel sensor MuPix8. Published in: *Journal of Instrumentation* 14 (2019) C10011.
- Schimassek, Rudolf et al. [including **Annie Meneses Gonzalez**]. Test results of ATLASPIX3 — A reticle size HVCMOS pixel sensor designed for construction of multi chip modules. Published in: *Nucl. Instrum. Meth. A* 986 (2021) 164812.
- Peric, Ivan et al. [including **Annie Meneses Gonzalez**]. High-Voltage CMOS Active Pixel Sensor. Published in: *IEEE J. Solid State Circuits* 56 (2021) 8, 2488-2502.
- Mu3e Collaboration [including **Annie Meneses Gonzalez**]. Technical design of the phase I Mu3e experiment. Published in: *Nucl. Instrum. Meth. A* 1014 (2021) 165679

Bibliography

[1] D. Boer et al., *"J/ψ meson production in SIDIS: matching high and low transverse momentum"*

[2] G. Hall, *"Semiconductor particle tracking detectors"*, Reports on Progress in Physics **57**, 481 (1994)

[3] R. A. Sidwell et al., *"Measurement of Charmed Particle Lifetimes"*, Annual Review of Nuclear and Particle Science **33**, 539 (1983)

[4] E. Heijne et al., *"A silicon surface barrier microstrip detector designed for high energy physics"*, Nuclear Instruments and Methods **178**, 331 (1980)

[5] Synopsys, *"Synopsys TCAD"*, `https://www.synopsys.com/silicon/tcad.html`

[6] M. Tilli & A. Haapalinna, *"Handbook of Silicon Based MEMS Materials and Technologies"*, second edition, William Andrew Publishing (2015)

[7] S. Sze, *"Semiconductor devices, physics and technology"*, Wiley (1985)

[8] G. Lutz, *"Semiconductor Radiation Detectors: Device Physics"*, Springer Berlin Heidelberg (2007)

[9] K. Graff, *"Metal impurities in silicon-device fabrication"*, Springer Science & Business Media (2013)

[10] A. A. Istratov & E. R. Weber, *"Physics of Copper in Silicon"*, Journal of The Electrochemical Society **149**, G21 (2002)

[11] A. Istratov, H. Hieslmair & E. Weber, *"Iron contamination in silicon technolog"*, Applied Physics A **70**, 489–534 (2000)

[12] W. Zulehner, *"Czochralski growth of silicon"*, Journal of Crystal Growth **65**, 189 (1983)

[13] K. Sumino & I. Yonenaga, *"Oxygen Effect on Mechanical Properties"*

[14] A. Borghesi, B. Pivac, A. Sassella & A. Stella, *"Oxygen precipitation in silicon"*, Journal of Applied Physics **77**, 4169 (1995)

[15] I. Yonenaga, *"Dislocation behavior in heavily impurity doped Si"*, Scripta Materialia **45**, 1267 (2001)

[16] *"SEMI MF723 - Practice for Conversion Between Resistivity and Dopant or Carrier Density for Boron-Doped, Phosphorous-Doped, and Arsenic-Doped Silicon"*, SEMI International Standards **45**,

[17] H. Kolanoski & N. Wermes, *"Semiconductor detectors"*, in *"Particle Detectors: Fundamentals and Applications"*, Oxford University Press (2020)

[18] W. Shockley & W. T. Read, *"Statistics of the Recombinations of Holes and Electrons"*, Phys. Rev. **87**, 835 (1952)

[19] M. J. Bosma, *"On the Cutting Edge of Semiconductor Sensors: Towards Intelligent X-ray Detectors"*

[20] W. Dietze, W. Keller & A. Mühlbauer, *"Float-Zone Grown Silicon"*, Springer Berlin Heidelberg (1981), 1-42

[21] W. Zulehner, *"The Growth of Highly Pure Silicon Crystals"*, Metrologia **31**, 255 (1994)

[22] S. Kumar et al., *"A Review of Cylindrical Grinding Process parameters by using various Optimization techniques and their effects on the surface Integrity, Wear Rate and MRR"*

[23] N. Qin et al., *"Simultaneous double side grinding of silicon wafer: a review and analysis of experimental investigations"*", Machining Science and Technology **13**, 285 (2009)

[24] *"A grinding-based manufacturing method for silicon wafers: an experimental investigation"*, International Journal of Machine Tools and Manufacture **45**, 1140 (2005)

[25] U. Satake et al., *"Optimization Method for Double-sided Polishing Process based on Kinematical Analysis"*, Procedia CIRP **41**, 870 (2016)

[26] David-Leon Pohl, *"3D-Silicon and Passive CMOS Sensors for Pixel Detectors in High Radiation Environments"*

[27] H. Robbins & B. Schwartz, *"Chemical Etching of Silicon"*, Journal of The Electrochemical Society **106**, 505 (1959)

[28] L. Rossi et al., *"Pixel Detectors: From Fundamentals to Applications"*, Springer Berlin Heidelberg (2006)

[29] *"Single step ohmic contact for heavily doped n-type silicon"*, Applied Surface Science **506**, 144686 (2020)

[30] W. Shockley & W. T. Read, *"Statistics of the Recombinations of Holes and Electrons"*, Phys. Rev. **87**, 835 (1952)

[31] H. Bethe, *"Zur Theorie des Durchgangs schneller Korpuskularstrahlen durch Materie"*, Annalen der Physik **397**, 325 (1930)

[32] F. Bloch, *"Bremsvermögen von Atomen mit mehreren Elektronen"*, Zeitschrift für Physik 1933 81:5 **81**, 363 (1933)

[33] P. Zyla et al., *"Review of Particle Physics"*, PTEP **2020**, 083C01 (2020)

[34] W. Shockley, *"Currents to conductors induced by a moving point charge"*, *J. Appl. Phys.* **9**, 635 (1938)

[35] S. Ramo, *"Currents Induced by Electron Motion"*, *Proc. IRE* **27**, 584 (1939)

[36] H. Spieler, *"Signal formation and acquisition"*, in *"Semiconductor Detector Systems"*, Oxford University Press (2005)

[37] N. Wermes, *"Pixel detectors for charged particles"*, Nuclear Instruments and Methods in Physics Research Section A: Accelerators, Spectrometers, Detectors and Associated Equipment **604**, 370 (2009)

[38] I. Perić, *"A novel monolithic pixelated particle detector implemented in high-voltage CMOS technology"*, Nuclear Instruments and Methods in Physics Research Section A: Accelerators, Spectrometers, Detectors and Associated Equipment **582**, 876 (2007), VERTEX 2006

[39] A. Herkert, *"Characterization of a Monolithic Pixel Sensor Prototype in HV-CMOS Technology for the High-Luminosity LHC"*

[40] T. Rudzki et al., *"The Mu3e experiment: Toward the construction of an HV-MAPS vertex detector"*, in *"International Workshop on Future Linear Colliders"*

[41] H. Augustin, *"Development of a novel slow control interface and suppression of signal line crosstalk enabling HV-MAPS as sensor technology for Mu3e"*

[42] K. Arndt, H. Augustin et al., *"Technical design of the phase I Mu3e experiment"*, Nuclear Instruments and Methods in Physics Research Section A: Accelerators, Spectrometers, Detectors and Associated Equipment **1014**, 165679 (2021)

[43] HIMB project Collaboration, E. Valetov, *"Beamline design and optimisation for high intensity muon beams at PSI"*, JACoW **IPAC2022**, 523 (2022)

[44] E. Mobs, *"The CERN accelerator complex. Complexe des accélérateurs du CERN"*

[45] B. Schmidt, *"The High-Luminosity upgrade of the LHC: Physics and Technology Challenges for the Accelerator and the Experiments"*, *J. Phys. Conf. Ser.* **706**, 022002 (2016)

[46] LHCb Collaboration, *"LHCb detector performance"*, *Int. J. Mod. Phys. A* **30**, 1530022 (2015)

[47] P. Hopchev, *"SciFi: A large Scintillating Fibre Tracker for LHCb"*

[48] V. Bellee, T. Hume & O. Steinkamp, *"Occupancy studies for the LHCb Run4 Mighty Tracker"*

[49] J. Hammerich & on behalf of the LHCb MightyTracker group, *"Towards MightyPix, an HV-MAPS for the LHCb Mighty Tracker upgrade"*, Journal of Instrumentation **17**, C10005 (2022)

[50] T. Weber, *"High-voltage monolithic active pixel sensors for the PANDA luminosity detector and search for the decay e+ e- -> eta c eta pi+ pi- at center of mass energies between 4.23-4.36 GeV at BESIII"*

[51] I. Selyuzhenkov, *"Status of the FAIR facility in Darmstadt"*, Journal of Physics: Conference Series **1685**, 012020 (2020)

[52] R. Sánchez, A. Braeuning-Demian, J. Glorius, S. Hagmann, P.-M. Hillenbrand, A. Kalinin, T. Köhler, Y. A. Litvinov, N. Petridis, S. Sanjari, U. Spillmann & T. Stöhlker, *"Towards experiments with highly charged ions at HESR"*, X-Ray Spectrometry **49**, 33 (2020)

[53] R. Hagdorn, *"Characterization of the MuPix8 sensor for the prototype of the $\bar{P}ANDA$ luminosity detector"*

[54] A. Karavdina, *"Preparation for the accurate luminosity measurement by antiproton-proton elastic scattering and feasibility study for observation of h_c hadronic decay modes at the PANDA experiment"*

[55] R. Diener et al., *"The DESY II Test Beam Facility"*, *Nucl. Instrum. Meth. A* **922**, 265 (2019)

[56] J. Baudot et al., *"First test results Of MIMOSA-26, a fast CMOS sensor with integrated zero suppression and digitized output"*, in *"2009 IEEE Nuclear Science Symposium Conference Record (NSS/MIC)"*, 1169-1173

[57] H. Augustin et al., *"Upgrading the beam telescopes at the DESY II Test Beam Facility"*, Nuclear Instruments and Methods in Physics Research Section A: Ac-

celerators, Spectrometers, Detectors and Associated Equipment **1040**, 167183 (2022)

[58] J. P. Hammerich, *"Analog Characterization and Time Resolution of a large scale HV-MAPS Prototype"*

[59] J. Kroeger, *"Characterisation of a High-Voltage Monolithic Active Pixel Sensor Prototype for Future Collider Detectors"*

[60] T. Semiconductors, URL: https://www.tsisemi.com/.

[61] M. Menzel, *"Calibration of the MuPix10 Pixel Sensor for the Mu3e Experiment"*

[62] H. Augustin et al., *"MuPix10: First Results from the Final Design"*, JPS Conf. Proc. **34**, 010012 (2021)

[63] T. Semiconductors, URL: https://ams.com/en/ams-start.

[64] ATLAS Collaboration, *"Technical Design Report for the ATLAS Inner Tracker Pixel Detector"*

[65] D. M. S. Sultan et al., *"Electrical characterization of 180 nm ATLASPix2 HV-CMOS monolithic prototypes for the High-Luminosity LHC"*, Journal of Instrumentation **15**, P05022 (2020)

[66] M. Prathapan et al., *"ATLASpix3 : A high voltage CMOS sensor chip designed for ATLAS Inner Tracker"*, PoS **TWEPP2019**, 010 (2020)

[67] M. Vogt, H. Krüger, T. Hemperek, J. Janssen, D. Pohl & M. Daas, *"Characterization and Verification Environment for the RD53A Pixel Readout Chip in 65 nm CMOS"*, "

[68] I. Perić et al., *"A high-voltage pixel sensor for the ATLAS upgrade"*, Nuclear Instruments and Methods in Physics Research Section A: Accelerators, Spectrometers, Detectors and Associated Equipment **924**, 99 (2019), 11th International Hiroshima Symposium on Development and Application of Semiconductor Tracking Detectors

[69] M. R. Pinto, *"PISCEA-II User's Manual"*

[70] B. University of California, *"The Spice Page"*

[71] Synopsys, *"Sentaurus Structure Editor"*

[72] G. J. Sussman & G. L. S. Jr., *"Scheme: An interpreter for extended lambda calculus"*, in *"MEMO 349, MIT AI LAB"*

[73] J. Barnes & R. Lomax, *"Finite-element methods in semiconductor device simulation"*, IEEE Transactions on Electron Devices **24**, 1082 (1977)

[74] Synopsys, *"Sentaurus Mesh User Guide"*

[75] Synopsys, *"Sentaurus Device User Guide"*

[76] H. Augustin, *"Characterization of a novel HV-MAPS Sensor with two Amplification Stages and first examination of thinned MuPix Sensors"*

[77] L. Huth, *"A High Rate Testbeam Data Acquisition System and Characterization of High Voltage Monolithic Active Pixel Sensors"*

[78] H. Augustin et al., *"MuPix: an HV-MAPS for the Mu3e experiment"*, Journal of the Physical Society of Japan **24**, others (2023), Proceedings of the 31th International Workshop on Vertex Detectors (VERTEX2022), in preparation

[79] S. Gao et al., *"Warping of silicon wafers subjected to back-grinding process"*, Precision Engineering **40**, 87 (2015)

[80] J. Wüstenfeld, *"Characterisation of Ionisation-Induced Surface Effects for the Optimisation of Silicon- Detectors for Particle Physics Applications"*

[81] M. Benoit, *"Study of radiation hardened pixel planar detectors for ATLAS vertex detector update"*

[82] H. Augustin et al., *"Performance of the large scale HV-CMOS pixel sensor MuPix8"*, Journal of Instrumentation **14**, C10011 (2019)

[83] EUDET Project, *"EUDET: Detector RD towards the International Linear Collider"*

[84] J. Baudot et al., *"First test results of MIMOSA-26, a fast CMOS sensor with integrated zero suppression and digitized output"*, *IEEE Nucl Sci Symp Conf Rec (2009)* , 1169 (2009)

[85] Y. Liu & Cothers, *"ADENIUM – A demonstrator for a next-generation beam telescope at DESY"*

[86] M. Mager, *"ALPIDE, the Monolithic Active Pixel Sensor for the ALICE ITS upgrade"*, Nuclear Instruments and Methods in Physics Research Section A: Accelerators, Spectrometers, Detectors and Associated Equipment **824**, 434 (2016), Frontier Detectors for Frontier Physics: Proceedings of the 13th Pisa Meeting on Advanced Detectors

[87] P. Baesso et al., *"The AIDA-2020 TLU: a flexible trigger logic unit for test beam facilities"*, Journal of Instrumentation **14**, P09019 (2019)

[88] P. Ahlburg et al., *"EUDAQ-a data acquisition software framework for common beam telescopes"*, *JINST* **15**, P01038 (2020)

[89] CLICdp Collaboration, J. Kröger et al., *"User Manual for the Corryvreckan Test Beam Data Reconstruction Framework, Version 1.0"*

[90] H. Augustin et al., *"The MuPix System-on-Chip for the Mu3e Experiment"*, Nucl. Instrum. Meth. A **845**, 194 (2017)

[91] C. Kleinwort, *"General Broken Lines as advanced track fitting method"*, *Nucl. Instrum. Meth. A* **673**, 107 (2012)

[92] V. Blobel et al., *"Fast alignment of a complex tracking detector using advanced track models"*, *Comput. Phys. Commun.* **182**, 1760 (2011)

[93] F. James & M. Roos, *"Minuit - a system for function minimization and analysis of the parameter errors and correlations"*, *Comput. Phys. Commun.* **10**, 343 (1975)

[94] M. A. Vos et al., *"Charge collection with binary readout from a test beam perspective"*

[95] J. Stricker, *"Testing of a Method for the Sensor Thickness Determination and a Cluster Size Study for the MuPix10"*

[96] R. M. Muenker, *"Test beam and simulation studies on High Resistivity CMOS pixel sensors"*

Acknowledgments

I would like to express my sincere gratitude to my supervisor, André Schöning, for providing me with the invaluable opportunity to pursue my Ph.D. research under his guidance. Your expertise and encouragement have been instrumental in shaping this thesis, and I am truly grateful for your mentorship. I would also like to extend my thanks to Peter Fischer for his patience and willingness to be the second referee of this thesis.

Many thanks to my Mu3e and HVMAPS group colleagues, Thomas Rudzki, Sebastian Dittmeier, and Luigi Vigani, for their collaboration and assistance throughout my research. Thanks to the members of the testbeam crew, Benjamin Weinläder, and David Immig, for their support during the experimental phase of my research. Special thanks to Heiko Augustin for his unwavering support from day one. Your guidance, advice, and encouragement have been indispensable, and I am truly grateful. I am also grateful to Adrian Herkert and Lennart Huth for their assistance and support during all the testbeam activities. Your contributions and willingness to help have significantly impacted the success of my research.

To my dear friends Tamasi Kar and Marta Marta Czurylo, thank you for making each day more enjoyable with your fun-filled conversations and coffee breaks in the afternoon. Your friendship has been a constant source of support and happiness throughout my Ph.D. A heartfelt thank you goes to Luigi for providing delicious food and organizing memorable parties. Your ability to create a joyful atmosphere has brought much-needed relaxation and joy to this journey.

I would like to extend my appreciation to all my Cuban friends who have shown me love and encouragement in their own unique ways, especially Desy, Ely, and Wendy. Your friendship and unwavering support have meant the world to me.

To my mom, you are my biggest fan, my pillar of support, and my everything. Without your guidance, none of this would have been possible. Thank you for always believing in me and guiding me toward success. I am grateful to my dad for his unconditional love and for passing on to me the trait of patience. Your constant

support and encouragement have been a driving force throughout my Ph.D. journey. To my abuela Carmen for feeding me the best food in the world and for his love. Nana, and Ara, thank you for your love and unwavering support. Your presence in my life has been a source of strength and inspiration.

I extend my gratitude to tia Eleiza for introducing me to the path of science and for her guidance and mentorship. To my tio Wilfred for always being a suport. To my abuela Cuki, tia Juana, Martica, and Delia for their love, my abuelo, tios, and primas, thank you for always being there for me and for your unwavering pride in my accomplishments. Your love and support have been a constant source of motivation.

Lastly, to my dear husband Arturo, from the moment our paths intertwined in that university classroom in 2010, it has been an extraordinary adventure. Thank you for being a constant source of love, strength, and unwavering support throughout these years. Together, we have conquered every challenge, and I am forever grateful to have you as my companion, both in academia and in our hearts.

To all those mentioned above and to anyone else who has contributed to my journey in ways big or small, please accept my heartfelt appreciation for your support, encouragement, and belief in me. This thesis would not have been possible without all of you.